7.0 Pressure Sensors

Monitoring of high pressures with high accuracy in oil reservoirs is vitally important for downhole oil exploration and oil recovery applications. In this chapter, we present the details of the pressure sensor system design, sensor fabrication methods and test results.

7.1 Pressure Sensor Design

The primary design issues of FABRY-PEROT pressure sensor include the sensor head geometry, material, sensor sensitivity, and sensor dynamic range. The geometry of a pressure sensor is shown in Figure 7.1. The sensor head is made by inserting two fibers into a fused silica capillary tube and thermally sealing them together so that an air gap is formed between the two cleaved fiber endfaces. When a hydrostatic pressure is applied, the capillary tube will deform, and as a consequence the cavity length will change. Effects in both the longitudinal and the transverse directions should be considered.

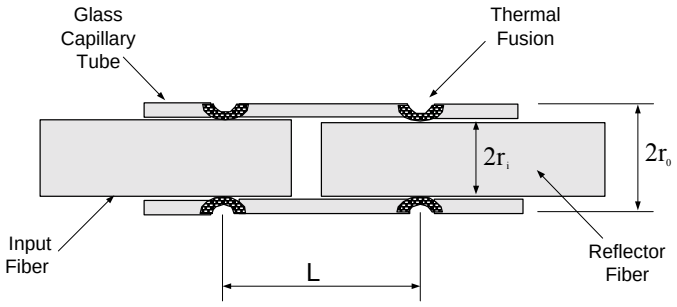

Figure 7.1. Geometry of SCIIB pressure sensor head.

Assume that the capillary tube has an outer radius of r_o and an inner radius of r_i. When the applied pressure changes from p_1 to p_2 the sensor air gap change (ΔL) can be expressed as

$$\Delta L = \frac{L}{E}[\sigma_z - \mu(\sigma_r - \sigma_t)], \qquad \textbf{(7-1)}$$

where L is the effective sensor gauge length defined as the distance between the two thermal bonding points; E is the Young's Modulus and μ is the Poisson's ratio of the capillary tube. For the fused silica materials used, $E=74$ *GPa,* and $\mu=0.17$. Three strains are concerned in the analysis: σ_r is the radial strain, σ_t is the lateral strain, and σ_z is the longitudinal strain generated by the applied pressure. Those three strains can be calculated by the following equations.

$$\sigma_r = \frac{(p_2 - p_1) r_o^{\,2}}{r_o^{\,2} - r_i^{\,2}} \left(1 - \frac{r_i^{\,2}}{r_0^{\,2}}\right) \qquad \textbf{(7-2)}$$

$$\sigma_t = \frac{(p_2 - p_1) r_o^{\,2}}{r_o^{\,2} - r_i^{\,2}} \left(1 + \frac{r_i^{\,2}}{r_0^{\,2}}\right) \qquad \textbf{(7-3)}$$

$$\sigma_z = \frac{(p_2 - p_1) r_o^{\,2}}{r_o^{\,2} - r_i^{\,2}} \qquad \textbf{(7-4)}$$

After combining Eq. (7-2) through (7-4), the sensor cavity length change caused by the applied pressure can be expressed as

$$\Delta L = \frac{L(p_2 - p_1) r_o^{\,2}}{E(r_o^{\,2} - r_i^{\,2})} (1 - 2\mu). \qquad \textbf{(7-5)}$$

Eq. (7-5) clearly shows that the change in applied pressure can be measured by the change in the air gap length of the sensor. If we calibrate the sensor cavity length at known pressure, we can measure the absolute applied pressure by measuring the change of the sensor cavity length. For SCIIB sensors, to avoid the phase ambiguity problem, the sensor must operate over the linear range of a half interference fringe, which is approximately a quarter of a fringe. It is very important to design the sensor head so that the sensor operation is constrained to this linear range. The geometrical parameters can be selected limit the measuring pressure to the linear portion of the interference fringe.

The maximum pressure measurement range is plotted versus the sensor effective gauge length and the outer diameter of the capillary tube in Figure 7.2. Here we assume that the

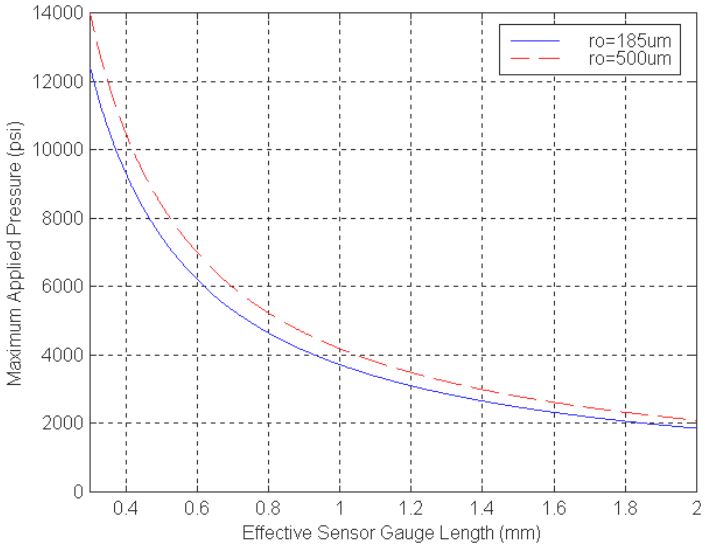

Figure 7.2. Relationship between the sensor geometric parameters and the maximum pressure.

inner diameter of the tube is 130 μm and the wavelength of the source is 1300 nm. The maximum applied pressure is set to cover only the linear portion of the interference fringe, which is a quarter of the source wavelength. As indicated in the plot, the change in outer diameter of the tube doesn't affect the sensor performance significantly. On the other hand, the choice of the effective gauge length can allow us to effectively design the sensor for different dynamic ranges.

7.2 Pressure Sensor Fabrication

The sensor head is fabricated by inserting two fibers into a silica glass capillary tube. The tube has an inner diameter of 130 μm, which is slightly larger than the fiber-cladding diameter of 125 μm. The outer diameter of the glass tube can be varied as required to achieve different dynamic ranges and resolutions according to Equation (7-5). In order to obtain good interference signals, the two fibers inside the capillary tube must be maintained in good alignment. Thereafter, the geometric parameters that can be used to modify the sensor performances are the effective sensor gauge L and the outer diameter of the capillary tube.

With the automated sensor fabrication system discussed in Chapter 6, we can fabricate high-performance sensor heads. First, fiber with the buffer removed are carefully cleaned using alcohol and well cleaved using a fiber cleaver. The capillary tube, also with the buffer removed, is also cleaned and well cleaved to the desired length. Second, with the help of the microscope, the two pieces of fiber are inserted into the capillary tube and clamped on the positioning stages by magnetic holders. By adjusting the micropositioning stage system, the two pieces of fiber are moved to the preset positions where the desired initial sensor F-P cavity length is obtained. By moving the two-dimensional translation stage underneath the micromotion stage system, the fiber and capillary tube assembly is brought to the center of the laser spot. The CO_2 laser emits light to heat the assembly with certain power level and duration controlled by the computer. For good quality, hermetically sealed sensor heads, the proper power level and duration of CO_2 laser exposure must be selected. After one side of the sensor head is bonded, the fiber and capillary assembly is then moved to the other side to perform an identical bonding process for the second bonding point. After completion of the second bonding process, a sensor head is produced.

7.2.1 Singlemode fiber sensor

The geometry of sensor head is the same as that shown in Figure 7.1. Both the input fiber and reflector fiber are 9/125μm standard singlemode fiber. The fiber and the tubing are coposed of the same material. The singlemode white light system is used to monitor the air gap. The measurement range is 15~50μm, and the accuracy is 10nm. Figure 7.3 shows the singlemode white light monitoring window.

7.2.2 Multimode fiber sensor

The geometry of sensor head is the same as that shown in Figure 7.1. Both the input fiber and reflector fiber are 62.5/125μm (or in some cases 50/125μm) regular multimode fiber. The fiber has a slightly larger CTE (coefficient of thermal expansion) than the tubing. When fabricating the sensor head, we use the multimode white light system to monitor the air gap.

The measurement range is 4.5~20 μm, and the accuracy is 1nm. Figure 7.4 shows the multimode white light monitoring window.

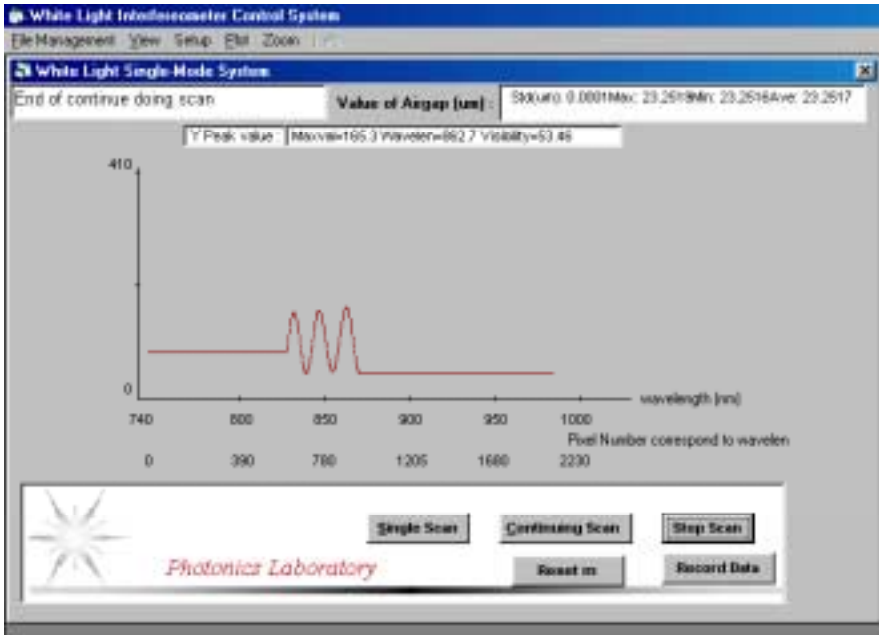

Figure 7.3. Singlemode white light monitoring window.

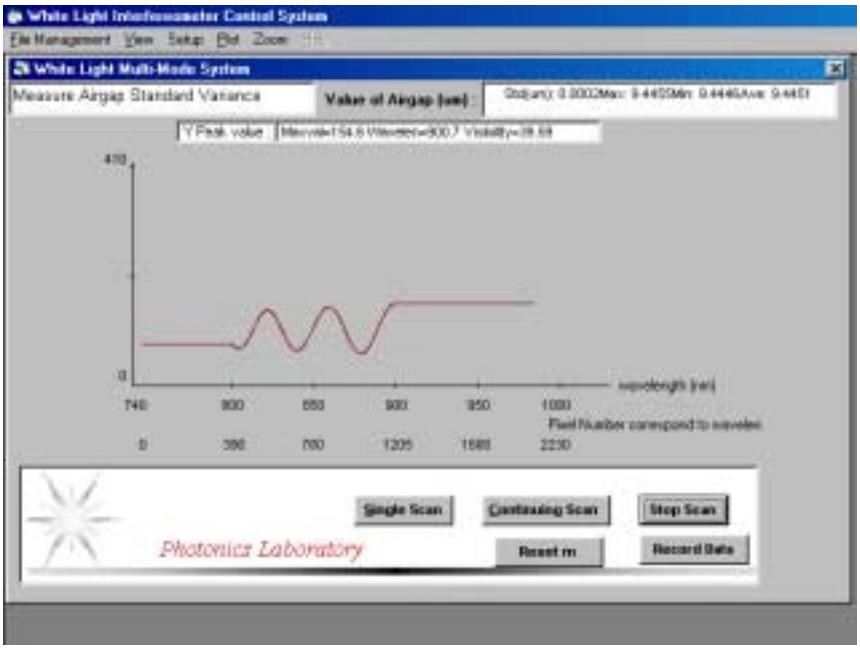

Figure 7.4. Multimode white light monitoring window.

7.3 Carbon Coated Multimode-Singlemode Combo Fiber Sensor

In order to protect the sensor head from water penetration, we choose a carbon coated multimode fiber for sensor head fabrication instead of regular fiber. The geometry of the carbon coated multimode fiber is shown in Figure 7.5.

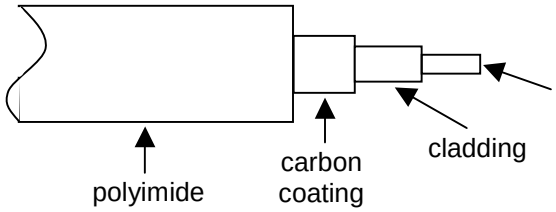

Figure 7.5. Schematic of carbon-coated fiber.

Before sensor fabrication, the polyimide must be removed so that the fiber can be put into the tubing. It was not easy to remove the polyamide from the glass fiber Two methods were developed for this polyimide removal process:

(1) Sulfuric acid: Heat sulfuric acid to 130°C in a test tube. Immerse fiber in the tube until the fiber color changes from brown to silvery. Then rinse the fiber with deionized water. This method is not difficult but time consuming and somewhat dangerous. Polyimide removal requires one hour and before sensor fabrication, the carbon coated fiber must be spliced with the output fiber of the white-light system.

(2) Blade: After much practice and experiment, we developed a technique to remove the polyimide from the carbon coating using a sharp blade to remove the polyimide. It is simple, but difficult because the carbon coatied fiber was very brittle. The angle and the force of the blade must be controlled very carefully in order to avoid fracturing the fiber. When the technique was mastered it only took several minutes to remove the polyimide and the fiber was not as brittle as the one handled by the first method. Figure 7.6 illustrates the process.

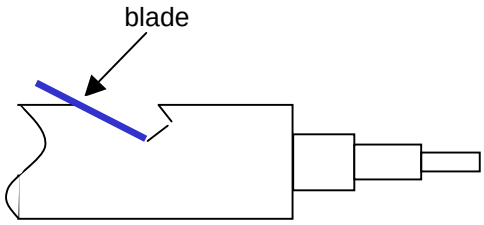

Figure 7.6. Polyimide removal from carbon-coated fiber using a blade.

7.3.1 Leakage prevention

In the downhole application, the optical fiber sensor must endure over 10000 psi pressure, and the bonding of the sensor must be strong enough to prevent leaking. After numerous

experiments, a three-point bonding method was developed. The sensors have three bonding points on both sides of the air gap as shown in Figure 7.7. In fact, the three points are continuous along the fiber and tubing, so the splice length is longer than it is for single point bonding.

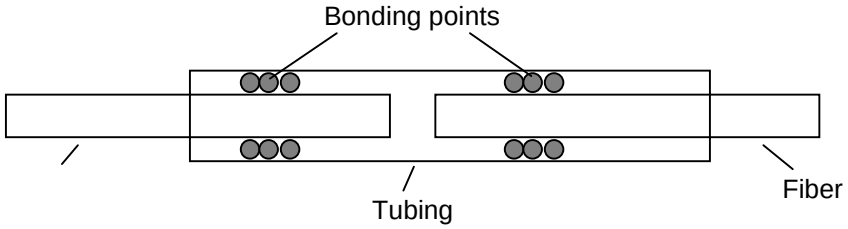

Figure 7.7. Schematic of three-point bonding.

7.3.2 Temperature sensitivity reduction

Since the carbon coated multimode fiber has a slightly larger CTE than the tubing, temperature changes will cause a change in air gap (Fabry-Perot cavity), causing a large error in the pressure measurement when the environmental temperature is not stable. After many trials, we designed a combination structure sensor head, shown in Figure 7.8. Between the two bonding points, the length of singlemode fiber used in the sensor fabrication is much longer than the carbon coated multimode fiber. Because the CTE of the singlemode fiber more closely matches the CTE of the tubing, the sensor head thermal dependence was greatly reduced.

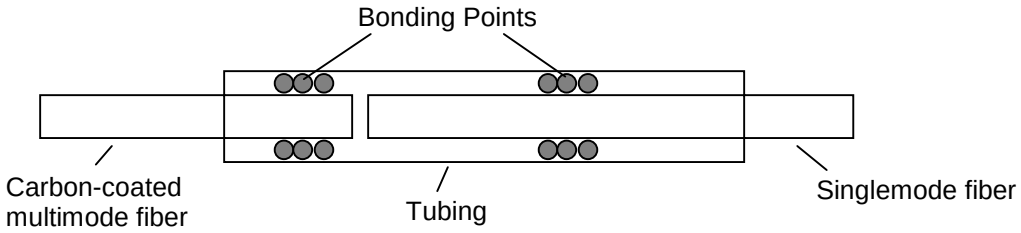

Figure 7.8. Combo structure sensor head to reduce temperature sensitivity.

7.3.3 Precise air gap control

The air gap of the fiber sensor must be controlled for two reasons.

(1) The visibility will be related to the air gap.
(2) Air gap measurement by the white-light system has a minimum and maximum limit.

We found that the air gap can be controlled during the CO_2 laser bonding process by bonding the reflector fiber side about 10 times. For the first 5 times, the laser power is adjusted through the series, 1.8w→ 2.0w→ 2.2→ 2.3w→ 2.33w. Then a power between 1.9~2.2w is used for the final five bonding repetitions. If the samepower is used for each repitition of the laser pulse, the air gap value will change linearly with the bonding times. Figure 7.9 shows the air gap adjustment process. After the first five bonding repetitions, the air gap changed from 21.6680 to 23.0665μm. Selecting the laser power between 2.0~2.2w, the air gap changes linearly during the last five times bonding. Therefore, by using the last five bondings to adjust the air gap to the desired value, a very close tolerance can be maintained on the initial air gap after fabrication. Finally, the air gap that was obtained in this way was very close to the desired value of 23.1945 μm.

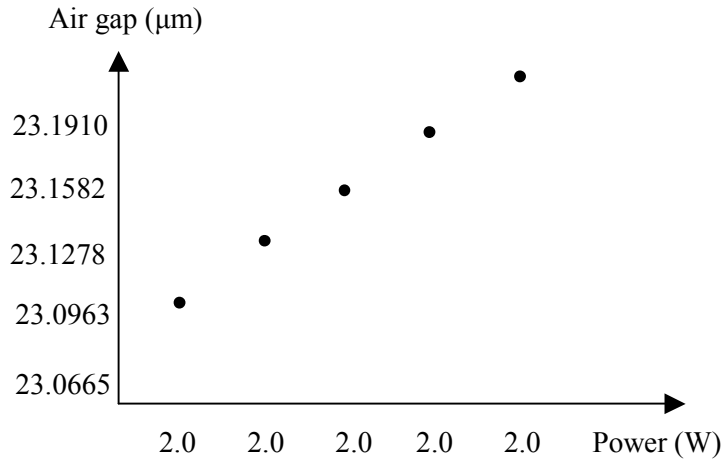

Figure 7.9. Air gap control by laser bonding power.

In Figure 7.9, bonding with a laser power of approximately 2.0W changes the air gap about 30nm for each laser pulse. The number of additional laser pulses required depends upon how close the air gap is to the desired value. If the airgap after the first five pulses of the laser is far from the desired value, more than 5 laser pulse may be required to bring the air gap to the desired value. Conversely, if the air gap after the first five laser pulses is very close to the desired value, fewer additional laser pulses will be required. The first five laser pulses can be thought of as the coarse adjustment and successive laser pulses as the fine adjustment. For even finer resolution air gap setting, the laser power of the last pulses can be changed as well. We can use a lower power to change the air gap more precisely and in practice, the highest precision that has been achieved is about 3nm.

7.3.4 Gauge length

The sensitivity of the pressure sensor is directly determined by the gauge length of the FABRY-PEROT sensor head. On another hand, to make the sensor head deployable, the sensor size should be small enough. After many experiment and tests, a 10mm gauge length was chosen. When pressure increases from 0~5000psi, the air-gap will decrease about 5μm.

7.3.5 Elimination of nonlinearity

The air gap will be decreased as the pressure applied on the sensor increases, *i.e.*, the Fabry-Perot cavity will become smaller. The change in air gap should be linear with the change in pressure because the Young's modulus of the tubing is a constant. But some sensors exhibit nonlinearity when the pressure is relative low. After many tests, we determined that the reason is the frictional force between the fiber and tubing in the region between the bonding points (which will be referred to as the gauge region), which may be caused by some dust or electrostatic charge. Although the shorter the multimode fiber, the smaller the thermal dependence, there is a tradeoff between thermal stability and nonlinearity. By numerous experiments, the optimum structure was found to consist of a 3mm carbon coating multimode fiber plus a 7mm singlemode fiber.

4.3.Pressure Sensor Testing System

Before the pressure sensor probe could be used for actual pressure measurement, it had to be calibrated to relate the output ratio to the applied pressure. Sensor calibration is usually conducted by applying known pressures within its operating range. The one-to-one relation between the sensor original output and the applied pressure forms the calibration curve which can be stored in the host computer and later used to convert the sensor output to the pressure reading.

7.3.6 System construction

The sensor calibration system was constructed based on a computer-controlled high-performance pressure generator/controller manufactured by *Advanced Pressure Products, Inc*. The system configuration is shown in Figure 7.10. The pressure controller/generator can supply a hydrostatic pressure up to 20,000 psi, and the accuracy of the pressure output is 0.1% of the full scale. The construction of this system allowed us to precisely and automatically calibrate the fiber optic pressure sensor over the entire operating range. The system also allowed us to test many performance characteristics of the pressure sensors such as the linearity, hysteresis, repeatability, and dynamic range.

Multiple pressure channels were fabricated on the APP pressure system, which could be controlled separately through several valves installed in the system piping. With this configuration, three pressure sensors could be tested at the same time. The sensors could also be tested under high pressures at elevated temperatures by heating one of the pressure test chambers using a flexible electric heating tape, which could achieve a temperature up to 700°C. This test was very important to evaluate the temperature dependence of the pressure sensor. The temperature sensitivity testing results were useful feedback to the sensor fabrication improvement.

A second pressure testing system was designed for testing the pressure sensors based on the Model 9035 pressure calibrator purchased from *Pressure Systems, Inc*. (*PSI*). This system has a relatively small pressure range but very high accuracy. The system configuration is shown in Figure 7.11. The calibration pressure range is from 0 to 250 psia, and the long-term accuracy is ±0.02% of the full range. This system allowed us to test the resolution and accuracy of the pressure sensor with a very high accuracy.

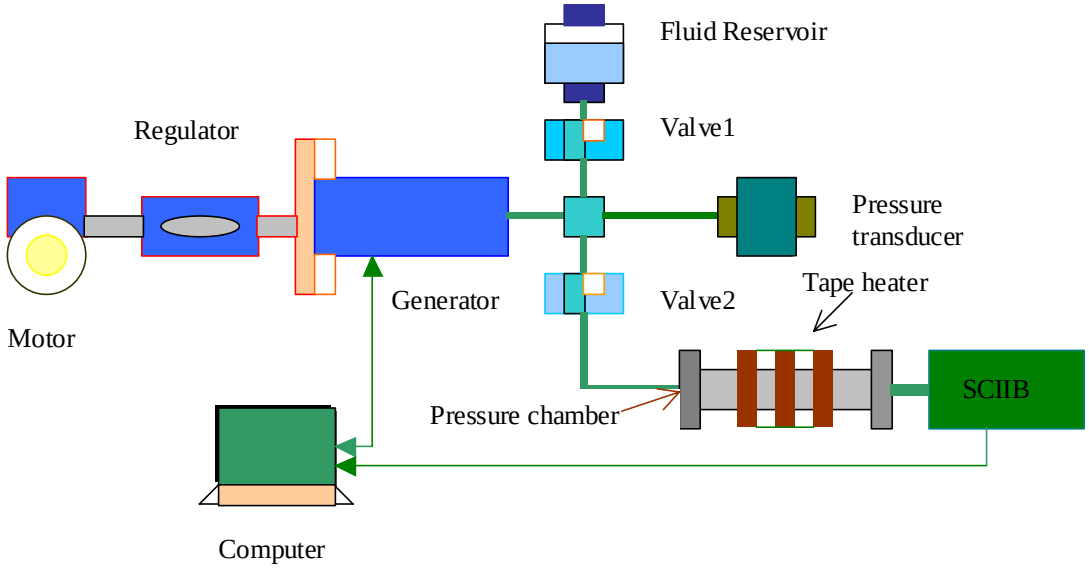

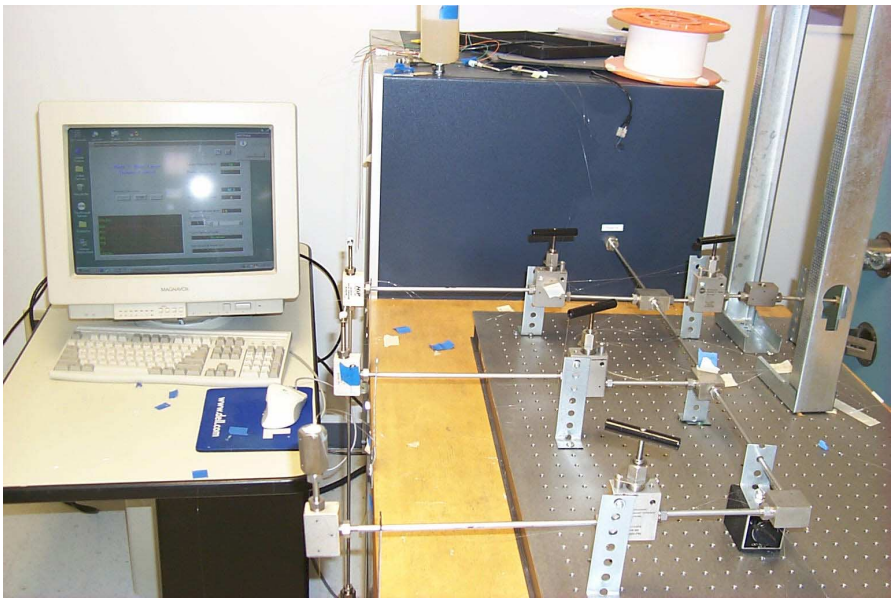

Figure 7.10. APP pressure sensor test system.

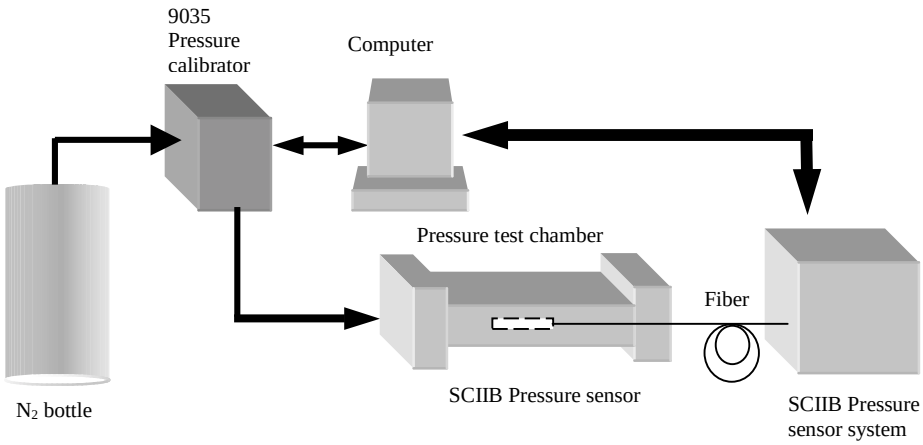

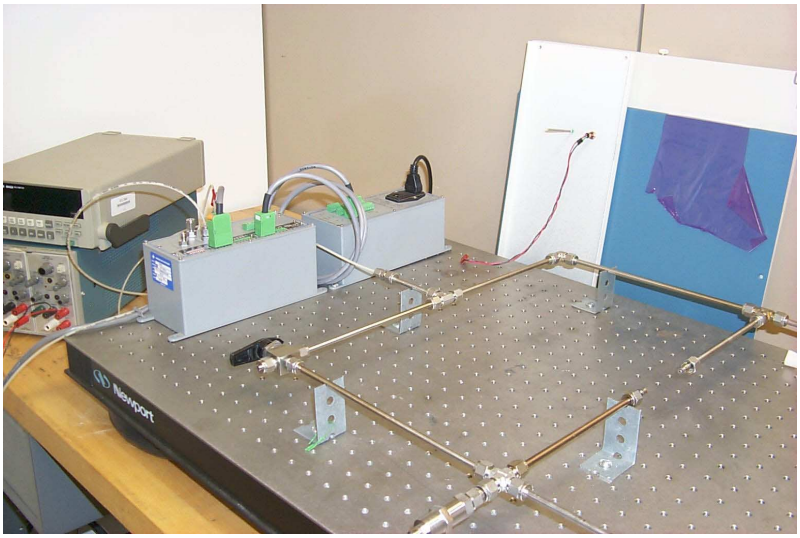

Figure 7.11. PSI 9035 based high accuracy pressure testing system configuration.

7.3.7 Calibration procedures

During the calibration process, the pressure sensor was installed inside the pressure calibration chamber. Through the computer programs, the hydrostatic pressure was applied to the sensor at increments of 1/40 of the estimated linear range of the pressure sensor. The pressure gauge inside the APP system measured the hydrostatic pressure inside the chamber and the system saved the data as applied pressure. At the same time, the output of the sensor system was sampled through the A/D converter and stored in another data file. To ensure the accuracy of the calibration, the system held the pressure at each step for about 50 seconds before moving to the next step. By taking the average within the pressure holding period, the error was minimized.

Figure 7.12 shows typical applied pressure data, and Figure 7.13 is the SCIIB output data recorded during the sensor calibration. The sensor used in the test was a singlemode fiber sensor with the gauge length of 0.5mm, initial cavity length of 25.46μm, and interference fringe visibility of 70%. Figure 7.14 plots the SCIIB output versus the applied pressure after averaging. A one-to-one relation of the applied pressure and the SCIIB output was then used to find the calibration equation through polynomial fitting. Experimental results revealed that the optimal order of the polynomial fitting was 10. Usually, the calibration curve was obtained by taking the average of several consecutive calibration data to further ensure the accuracy of calibration.

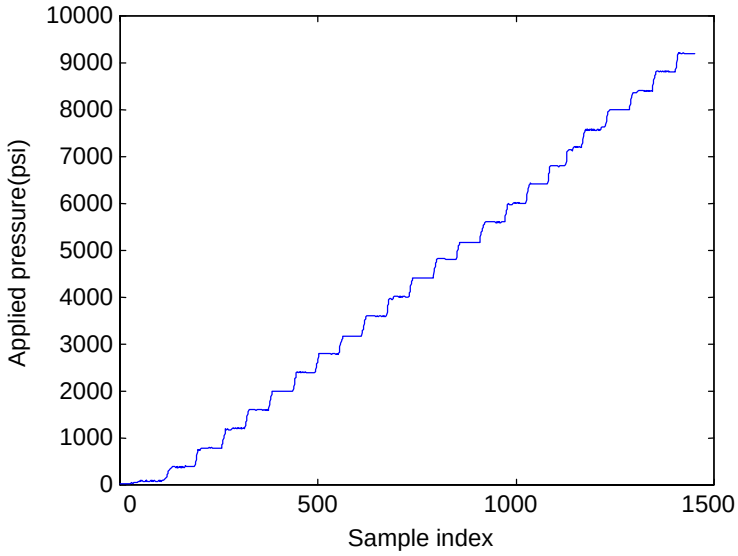

Figure 7.12. Applied pressure recorded during sensor calibration.

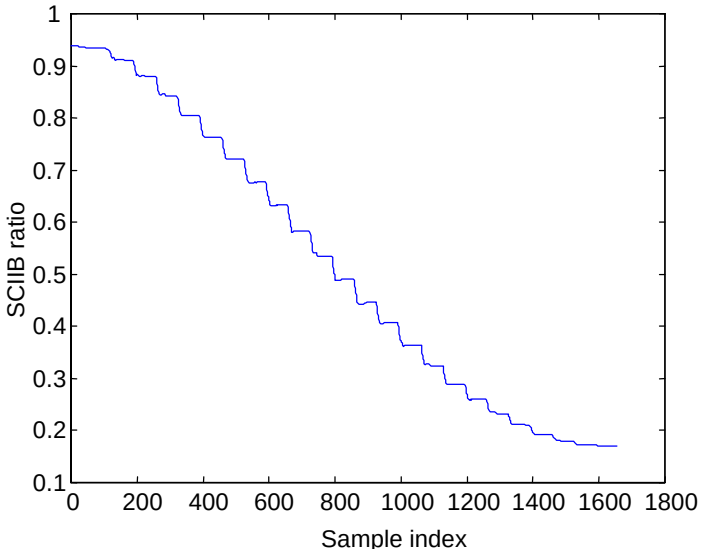

Figure 7.13. SCIIB output ratio recorded during sensor calibration.

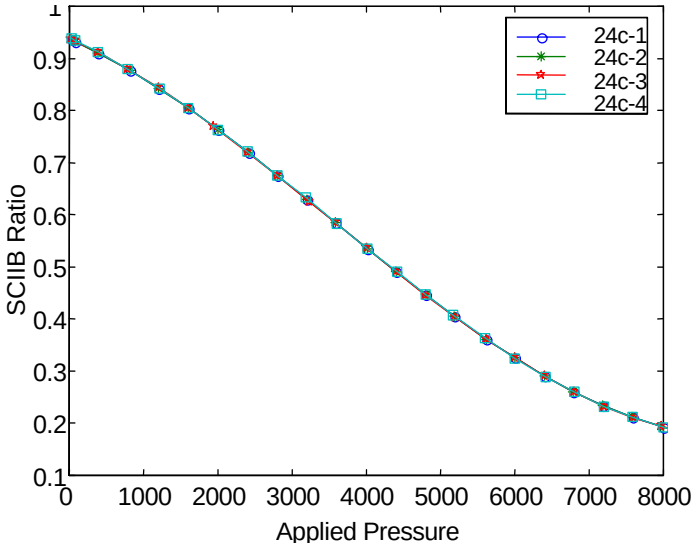

Figure 7.14. SCIIB pressure sensor calibration curve.

7.4 Experimental Results1

7.4.1SCIIB pressure sensors

After calibration of the sensors, the performance characteristics of the developed SCIIB pressure sensor system were evaluated, including linearity, hysteresis, resolution, repeatability, system stability, temperature cross sensitivity, and over pressure capability. These are each discussed in detail below.

7.4.1.1 Linearity

Due to the sinusoidal nature of the interference signal, the direct output from the SCIIB pressure sensor is a nonlinear function of the applied pressure. However, the calibration process can linearize the SCIIB output data by polynomial curve fitting. To assess the residual nonlinearity of the sensor system, we examined the measurement results after calibration, as shown in Figure 7.15, with respect to the applied pressure given by the *APP* system. The sensor used in the test was a singlemode fiber sensor with a gauge length of 0.5mm, initial cavity length of 25.46μm, and interference fringe visibility of 70%. The magnified deviation between the calibration line and the straight line is plotted in Figure 7.16. The maximum deviation is about 9psi. If we normalized the nonlinearity with respect the its full dynamic range of 8500psi, the normalized nonlinearity error is less than 0.1% of the full scale of pressure measurements, which is the best accuracy offered by the pressure calibration system.

7.4.1.2 Hysteresis

Hysteresis of the pressure sensor can be measured by cycling the applied pressure between the minimum and the maximum of the operating range in both increasing and decreasing directions. The hysteresis can be calculated as the largest difference between the output readings of the pressure cycles. The SCIIB pressure sensor probe is made of silica glass

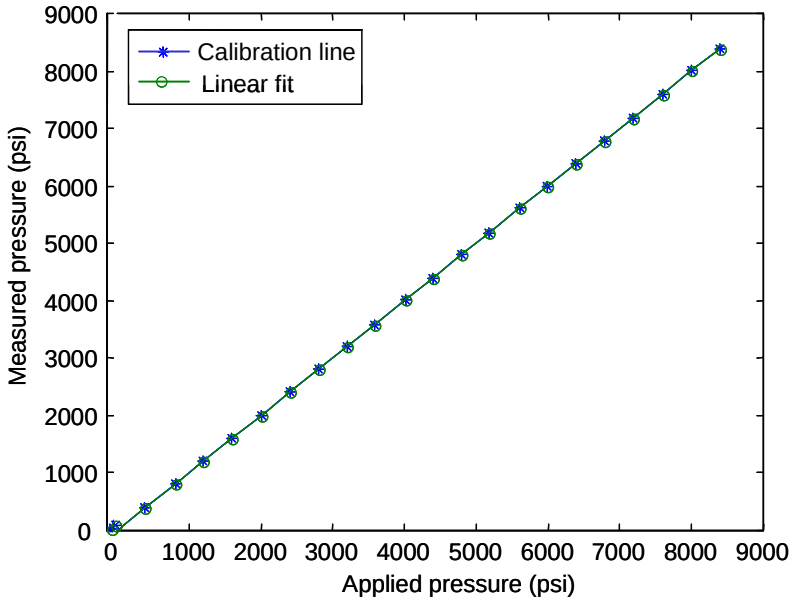

Figure 7.15. SCIIB pressure sensor system calibration lines.

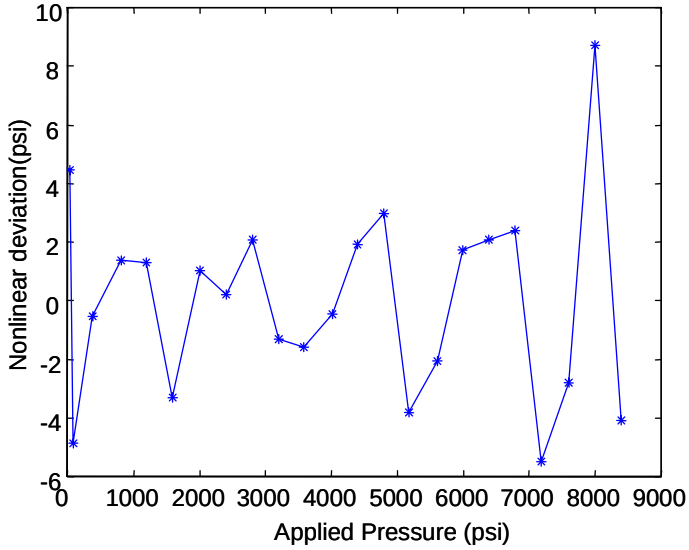

Figure 7.16. Nonlinearity of the SCIIB pressure sensor system

material and the operating range of the sensor in terms of pressure-induced strain is very small. Therefore, the hysteresis of the sensor probe is expected to be very small. Nevertheless, experiments were conducted to evaluate the actual hysteresis of the SCIIB sensor probe. The evaluation was conducted using the *APP* pressure system after the sensor system was calibrated. The applied pressure was first increased to the maximum operating range of 8500psi at the step of 400psi. The pressure was then decreased to atmospheric pressure after it was maintained at 8500psi for several minutes. The measurement results are

shown in Figure 7.17. The experimental results confirm our expectation. There was no noticeable hysteresis found within the entire operating range.

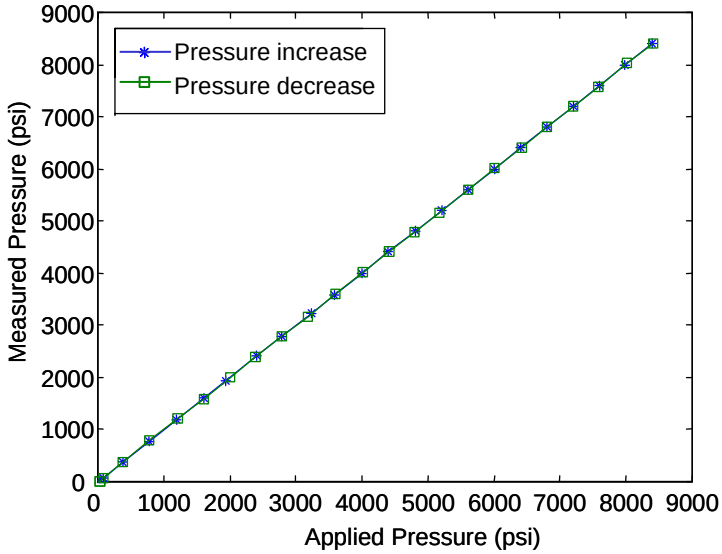

Figure 7.17. Hysteresis of the SCIIB pressure sensor.

7.4.1.3 Resolution

The resolution of the sensor system is usually interpreted as the standard deviation of a series of pressure measurements. It is common to use twice the standard deviation as the direct measure of resolution. The evaluation of the sensor resolution was performed using a calibrated sensor with the linear range of 8500psi. The sensor was exposed to the atmosphere where the pressure reading from the sensor should be around 15 psi. The data from the SCIIB system was sampled at a rate of 50 samples per second for one minute, which should be high enough compared to the system's frequency response of 15Hz. The pressure measurement outputs within the one-minute sampling period are plotted in Figure 7.18. The standard deviation of the pressure data within this time period was calculated to be σ=0.121psi. Therefore the resolution of the sensor system was estimated to be $2\ \sigma$ =0.242psi. The normalized resolution with respect to the dynamic range of the system was 0.003% of the full scale.

It must be pointed out that the resolution of the sensor is not constant within the entire operating range due to the non-linear nature of the interference signal. However, by confining the operating range of the SCIIB sensor within its semi-linear range, the resolution of the system should be retained within 60% of the maximum resolution as defined by Eq. (4-14).

7.4.1.4 Repeatability

Repeatability of the sensor can be measured by applying pressure to a certain preset point repeatedly from only one direction (increasing or decreasing). The largest difference of the sensor output readings can be used to specify the repeatability of the sensor. The same calibrated singlemode sensor was used to evaluate the repeatability of the system. Using the

APP system, two consecutive measurements up to the full operating range of the sensor were performed with the results shown in Figure 7.19. For comparison purposes, the original calibration data is also shown. The deviation of the two measurement results with respect to the calibration data are plotted in Figure 7.20. The maximum deviation between the measured pressure and the calibrated pressure was within ±13psi. The normalized repeatability of the sensor system with respect to its dynamic range was therefore ±0.15% of the full scale.

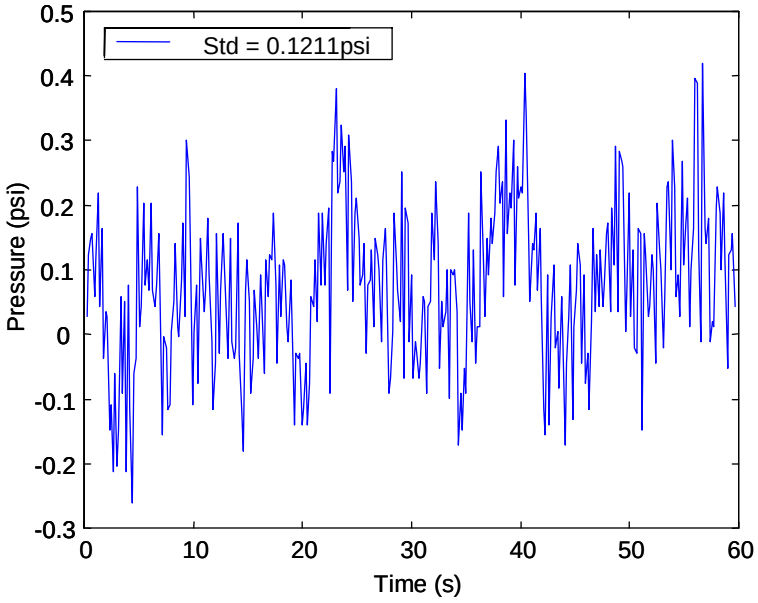

Figure 7.18. Standard deviation measurement of the SCIIB pressure sensor.

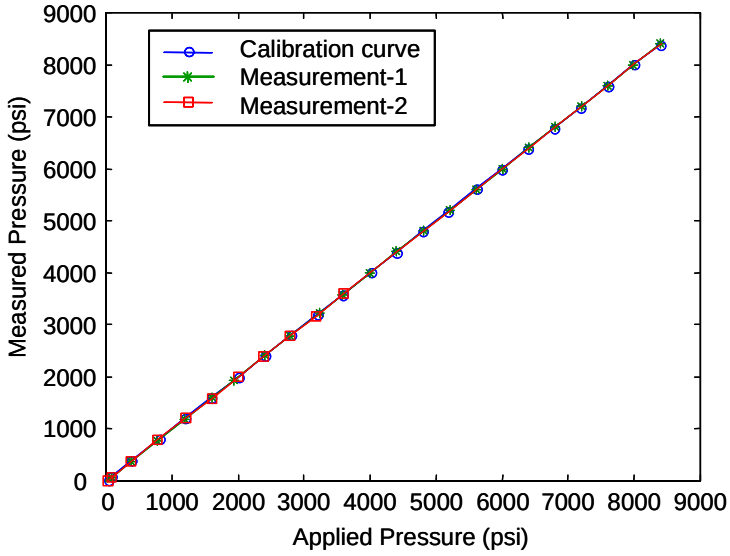

Figure 7.19. Repeatability of the pressure measurement.

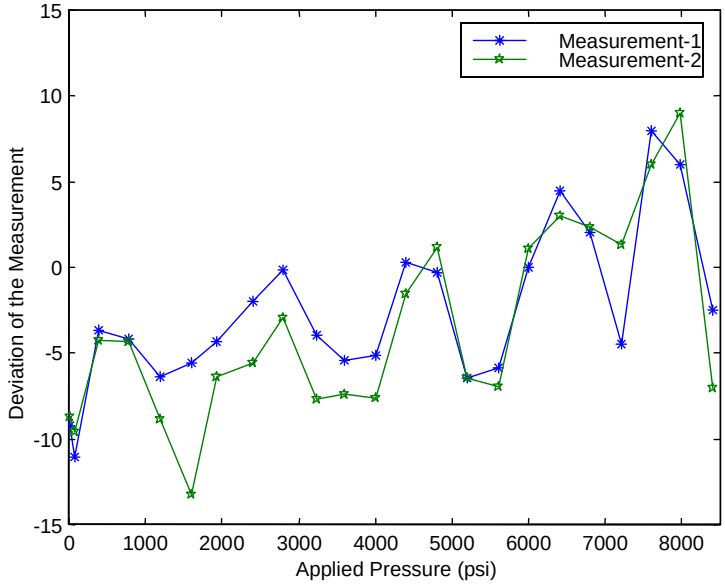

Figure 7.20. Deviation of the measured pressure with respect to the calibration data

7.4.1.5 System stability test

The same singlemode sensor with an operating range of 8500psi was also used to test the system stability. The sensor was kept in the pressure test chamber of the *APP* system for 24 hours starting from 4:00pm in the afternoon. The pressure of the chamber was maintained to the atmosphere pressure. The data acquisition system was programmed to sample the sensor's output every 20 seconds. The test result is shown in Figure 7.21. By processing the

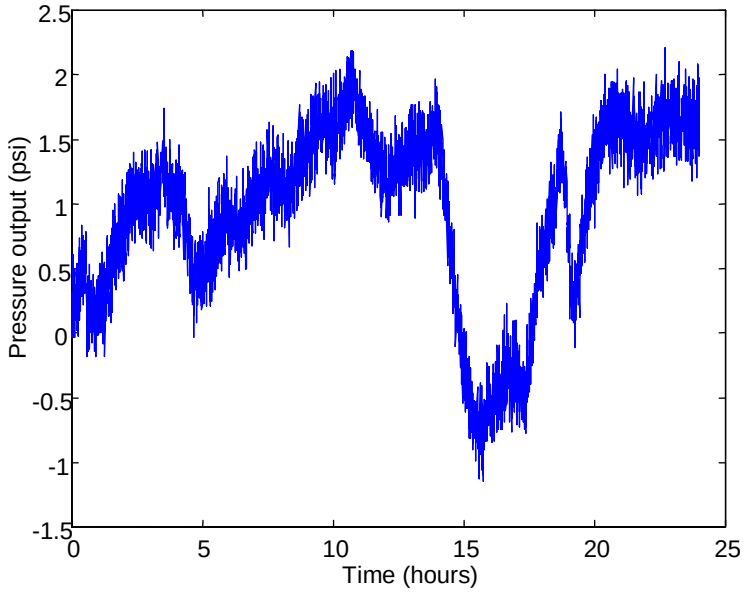

Figure 7.21. System stability over 24 hours.

data, the maximum peak-to-peak pressure variation within the 24-hour time period was 3.3 psi. The normalized maximum variation was thus 0.04% of the full dynamic range. The test results also showed that the variation of the data was not one-directional.

It must be said that the complete evaluation of the system stability needs much longer test period (for example, one year). Therefore, the stability test result of 24-hour period was hence not quite conclusive.

7.4.1.6 Temperature cross-sensitivity

The cross sensitivity to temperature could result in errors of the pressure measurement when the environmental temperature changes. The construction of the APP pressure calibration system allowed us to characterize the temperature cross sensitivity of the SCIIB pressure sensor by measuring pressures at different elevated temperatures. As shown in Figure 7.22, the same singlemode fiber sensor with a dynamic range of 8500psi was tested at temperatures of 24°C, 88°C, and 206°C respectively. Figure 7.23 shows clearly the measurement errors at the two elevated temperatures. The maximum deviation was 215psi at 88°C and 307psi at 206°C respectively. The maximum temperature cross sensitivity was thus calculated to be 0.04% per degree Celsius. It was also noticed that the large errors were found at the low and high pressure range where the nonlinear effects became the largest. The temperature cross sensitivity could thus be reduced by sacrificing the dynamic range of the sensor.

7.4.1.7 Overpressure capability test

In real downhole applications, pressures higher than the nominal values might be encountered due to the use of steam flood to pump the oil to the surface. It is therefore very important for the sensor to be able to sustain burst pressures higher than its dynamic range. The overpressure capability of the SCIIB pressure sensors was thus tested. The sensor used in the overpressure tests was a multimode fiber-based sensor with a gauge length of 1.0mm,

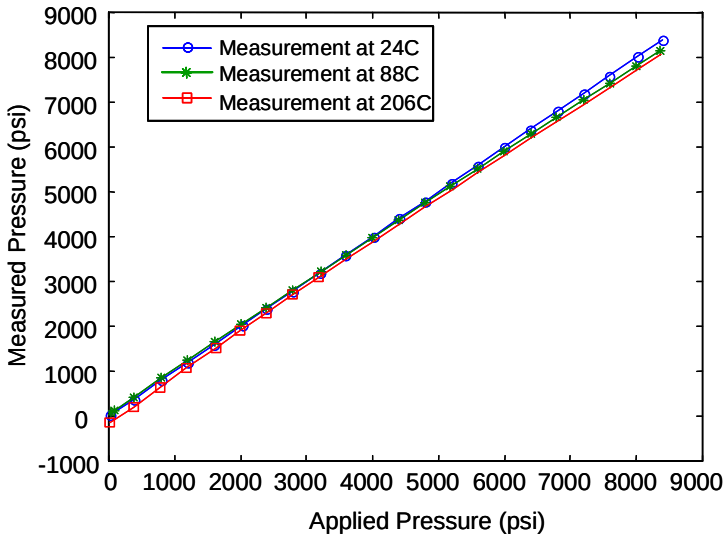

Figure 7.22. Temperature cross sensitivity of the SCIIB pressure sensor.

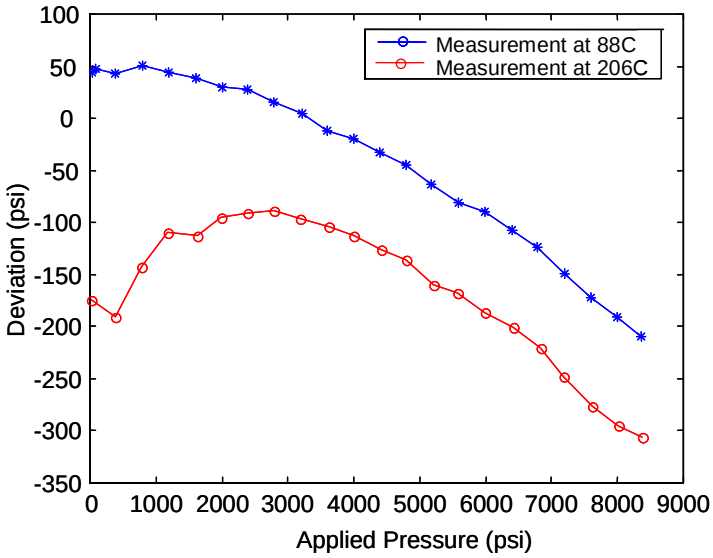

Figure 7.23. Pressure measurement errors resulting from the temperature dependence.

an initial cavity length of 5.67μm, and a fringe visibility of 49%. The sensor was calibrated to have a dynamic range of 1800psi.

The overpressure tests were conducted at room temperature. The sensor was first overpressured to 4000psi and kept in the pressurized chamber for one hour. After the pressure was released, the sensor was evaluated for the measurement of pressures within its dynamic range. The same experiment was also conducted at an overpressure of 6000psi for one hour. The experimental results are shown in Figure 7.24. The deviations from the original calibration line after the overpressures are shown in Figure 7.25. The overpressures do not show any observable effect on the sensor performance. The deviations shown in Figure 7.25 are within the range governed by the repeatability of the sensor.

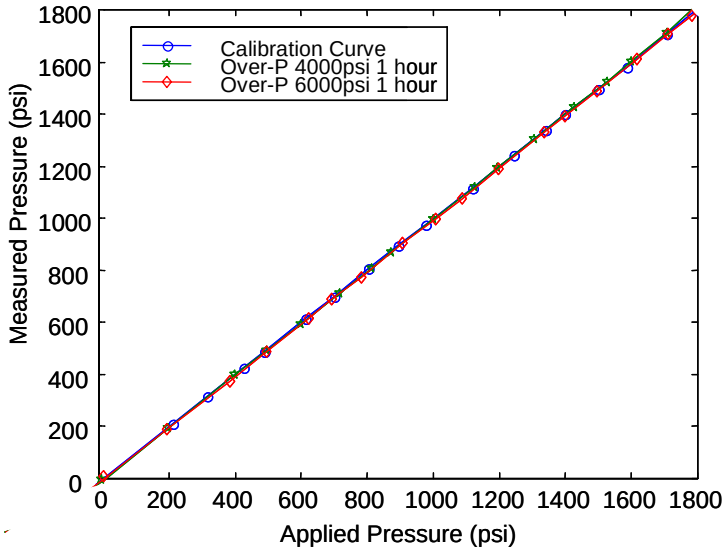

Figure 7.24. Overpressure test results of the multimode SCIIB sensor.

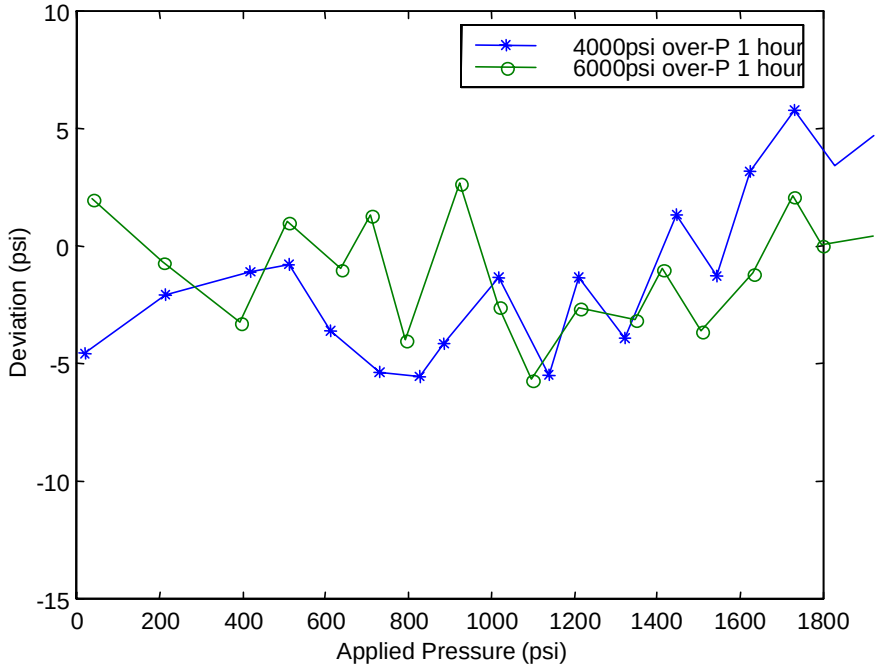

Figure 7.25. Sensor deviation of the overpressure tests.

7.4.1.8 Dynamic pressure measurement

To demonstrate the sensor's dynamic response, the calibrated SCIIB pressure sensors were applied for dynamic pressure measurements. The pressure signal was provided by the *APP* system after it was programmed to pressurize the chamber from atmospheric pressure to the preset pressure in even steps. Both a multimode sensor with an operating range of 1800psi and a singlemode sensor with an operating range of 8500psi were tested. The testing range for the multimode sensor was 900psi and that for single-mode sensor was 8500psi.

The pressure increases measured by the SCIIB pressure sensors are shown in Figure 7.26 and Figure 7.27 for the multimode and singlemode fiber sensors, respectively. The sampling rates of both the SCIIB sensor systems and the pressure gauge were set to one sample per second. The output of the built-in pressure gauge of the APP system is also plotted for comparison purposes. As shown in the two figures, the measurement results of both the multimode and single-mode fiber SCIIB sensors agreed very well with that of the built-in pressure gauge.

7.4.2 Multimode white light pressure sensors

Typical test results for the white light pressure sensor are shown in Figure 7.28. The pressure sensor was tested up to 6000psi five separate times. Two of them were performed at about 176 °C; others were performed at room temperature. The temperature dependence of the pressure sensor shown in Figure 7.28 is about 0.2psi/°C.

The results of the resolution testing of the pressure system are shown in Figure 7.29. In general, two times the standard deviation was taken as a measure of the resolution. The whole system was run continuously for 30 seconds. The sampling rate is about 5

points/second. The standard deviation calculated from the testing results is about 0.015nm, so the resolution of this system is about 0.03nm, which corresponds to 0.03psi.

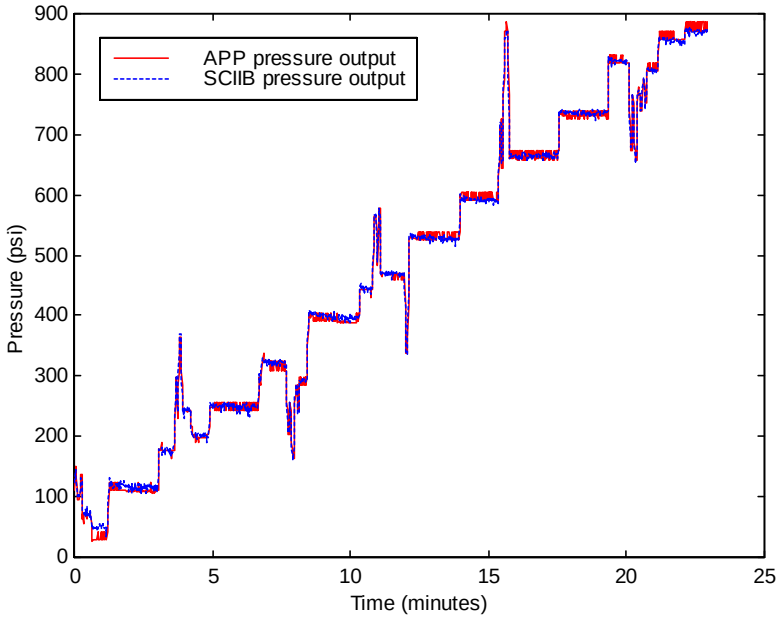

Figure 7.26. Dynamic pressure measurement results for the multimode sensor.

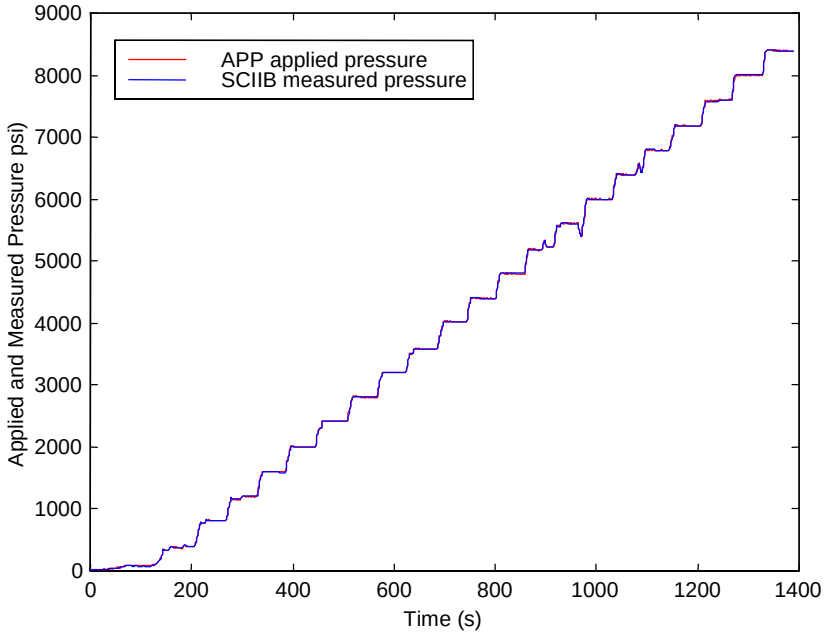

Figure 7.27. Dynamic pressure measurement results for the singlemode sensor.

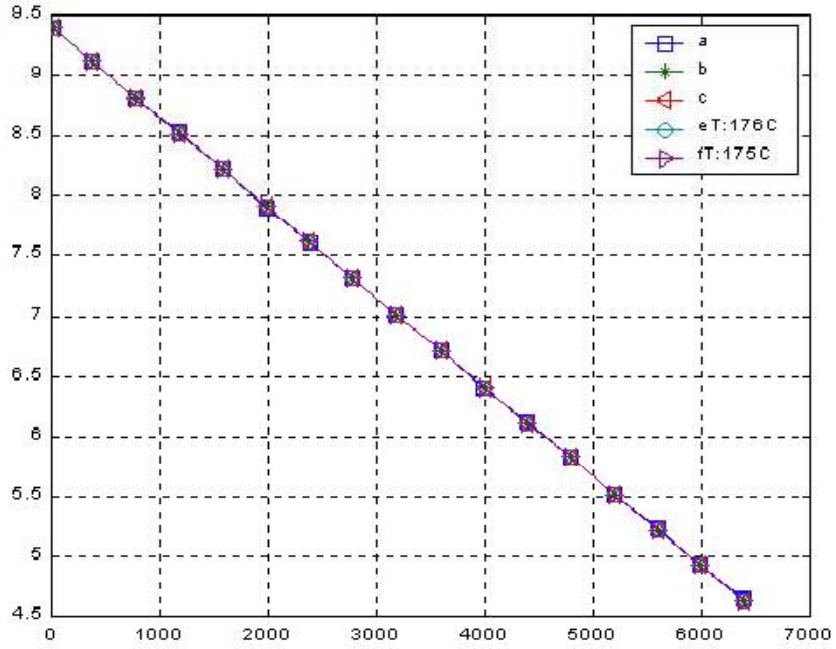

Figure 7.28. Testing results of a pressure sensor under different temperatures.

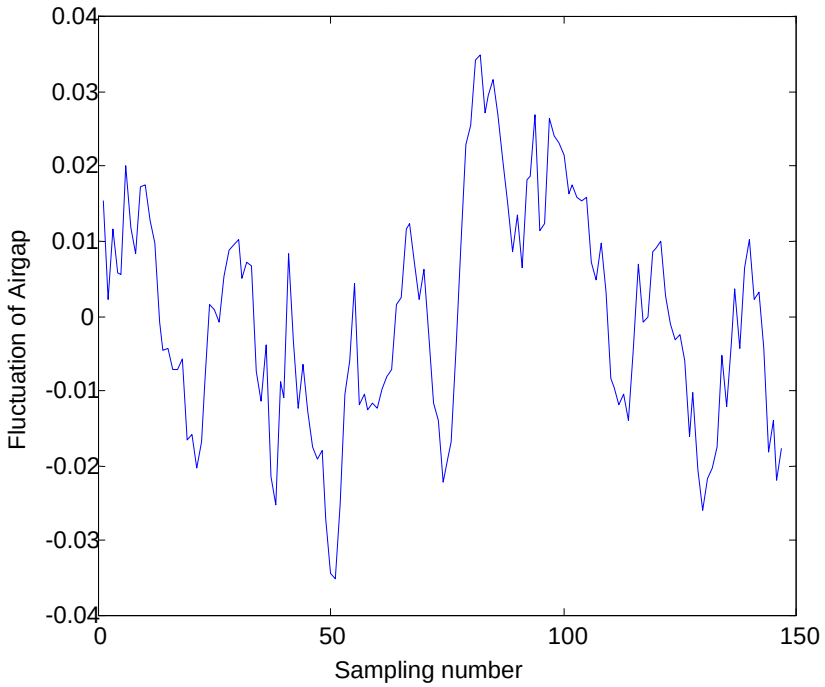

Figure 7.29. Resolution of pressure system.

The stability of the pressure system over 48 hours is shown in Figure 7.30. The maximum air gap error is less than ±0.5 nm, which corresponds to about ±0.5psi. Compared with the dynamic range of 6000psi, the stability is better than 0.01%.

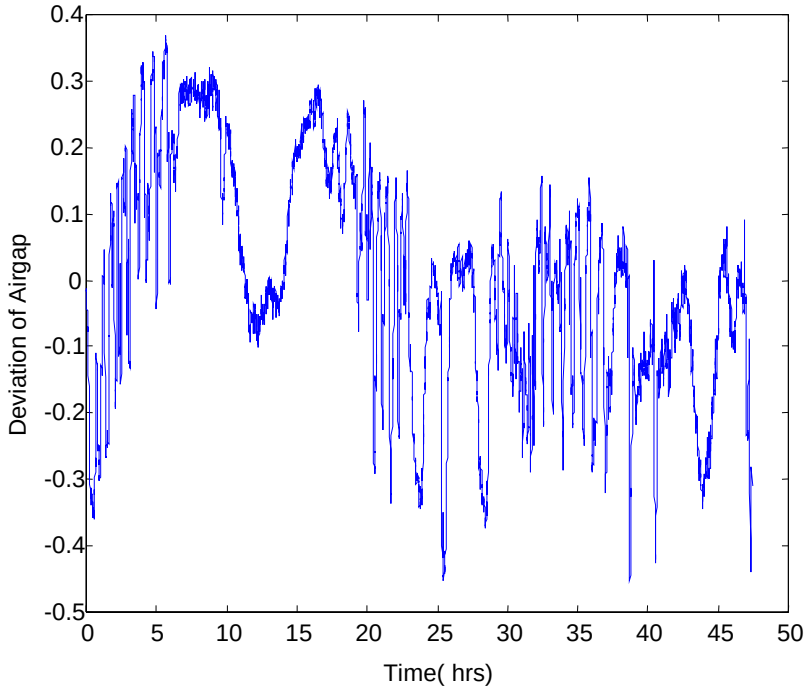

Figure 7.30. 48-hour stability testing of the pressure sensor.

8.0 Temperature Sensors

Temperature measurement and monitoring for downhole oil recovery was an important objective in this research project. The goal was to precisely measure the temperature between –40ºC and +200ºC with an accuracy of ±1.0ºC and resolution of a 0.01ºC under pressure up to 20,000 psia. In this chapter, we present the detailed design of the temperature sensor system, including the sensor geometric design, sensor fabrication, sensor testing, calibration and characterization.

8.1 Temperature Sensor Design

The geometry of the SCIIB fiber optic temperature sensor is illustrated in Figure 8.1. The structure of the temperature sensor resembles that of the pressure sensor except for differences in the geometric parameters and the material used for the alignment tube. When the ambient temperature changes, the physical length of the capillary tube and the fibers will change, which results in a change in the air gap between the two fiber endfaces. Using the white light system, this air gap change can be demodulated from the interference spectrum and thus enable precise measurement of the temperature. Since the same structure was used for both pressure and temperature sensor, the fabrication processes are similar.

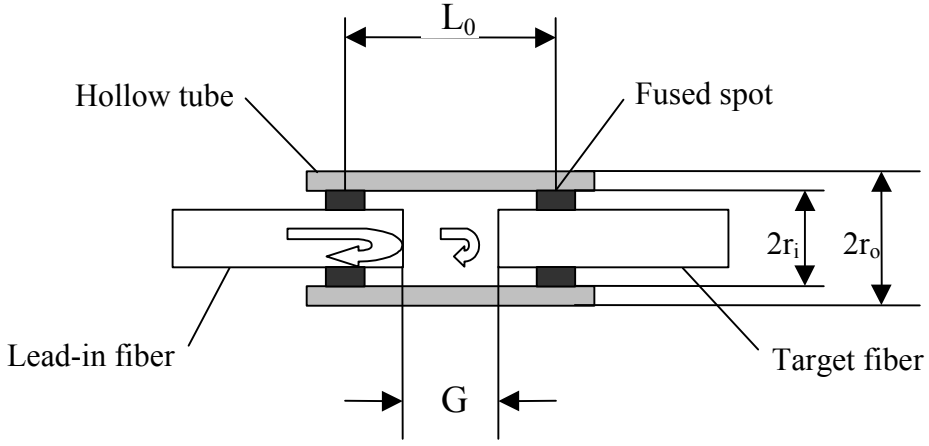

Figure 8.1. Geometry of FABRY-PEROT temperature sensor.

To increase the temperature sensitivity, the geometric parameters and the material used for the alignment tube are different from that for the pressure sensor. The operating principle of FABRY-PEROT temperature sensor can be described by

$$\Delta G = (\alpha_0 L_0 - \alpha_1 L_1 - \alpha_2 L_2)\Delta T\,, \qquad \textbf{(8-1)}$$

where ΔG is the air-gap change induced by the temperature change ΔT, L_0 is the gauge length of sensor head; L_1 is the length of input fiber defined from the input bonding point to the end-face of input fiber; L_2 is the length of reflecting fiber defined from the other bonding point to the end-face of reflecting fiber; α_0, α_1, α_2 are thermal expansion coefficients (CTE) of glass tube, input fiber and reflecting fiber, respectively.

Design of the temperature sensor was focused on selecting suitable materials for the glass tube and the reflecting fiber to increase the temperature sensitivity. Borosilicate glass was selected for the capillary tube, with a CTE of $\alpha_0=3.2*10\text{-}6/℃$. In general, the optical fiber is made by doping small amount of germanium into pure silica material. Typical optical fibers have a CTE of about $7.5*10^{-7}$/°C, which is very close to that of pure silica.

The maximum temperature measurement range is plotted versus the sensor effective gauge length in Figure 8.2. Here, we assume that the source wavelength is 1300 nm, the fiber is singlemode, and the maximum temperature change generates a gap change corresponding to 1/8 of the source wavelength, which covers the whole linear range of the interference fringe. The maximum measurement temperature decreases with increasing effective gauge length. The sensor can be designed to have a maximum temperature measuring range from 100°C to 800°C when it is fabricated to have a gauge length between 1 and 8 mm.

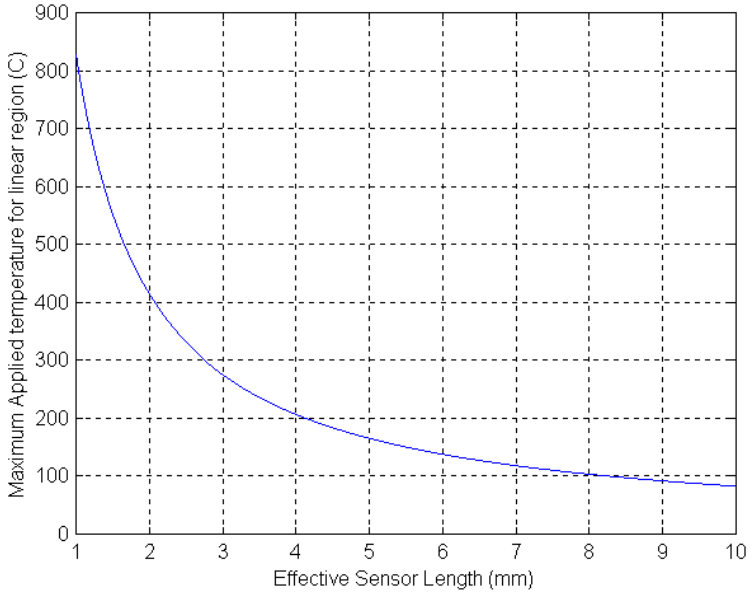

Figure 8.2. Relationship between sensor gauge length and temperature measurement range.

8.2 Temperature Sensor Fabrication

FABRY-PEROT temperature sensors can be fabricated on the automated sensor fabrication station described in Chapter 6. The fabrication process involves inserting two cleaved fibers inside a capillary tube and using the CO_2 laser to thermally fuse the fibers and the tube together. In our experiments, we used the fused borosilicate tube available from Vitrocom,

Inc. The inner diameter of the tube is 150 μm, and the outer diameter is 250 μm. The sensor effective gauge length can be controlled during the fabrication by using a translation stage to move the bonding point with respect to the CO_2 laser beam. After the sensor is fabricated, another CO_2 laser exposure is applied to provide proper annealing of the bonding region to remove residual stresses.

8.3 Pressure Cross-Sensitivity

In the downhole environment, both high pressure and high temperature exist. To eliminate the pressure dependence of the temperature sensor, a special tube was used to isolate pressure from the temperature sensor. The pressure isolator structure is shown in Figure 8.3. Isolation is achieved by bonding borosilicate glass tubing outside the temperature sensor. The borosilicate tubing is sealed at one end, and is bonded to the borosilicate alignment tubing of the FABRY-PEROT sensor on the other end, separating the outside pressure from the temperature sensor head. The borosilicate glass tubing can also provide mechanical protection for the lead-in fiber / sensor tubing joint.

There are three reasons to choose borosilicate as the material for both inner and outer tube: First, borosilicate has much larger CTE compared to fused silicate. From Eq.8-1, a large CTE difference between the tube and optical fiber will increase the sensitivity, resolution and dynamic range of temperature sensor dramatically. Second, bonding between identical materials is much stronger than that between different materials. Third, the laser power required for bonding the borosilicate tubing is much lower than the power required for bonding the fused silicate tubing. Thus the isolating tube bonding process will be harmless to the fiber.

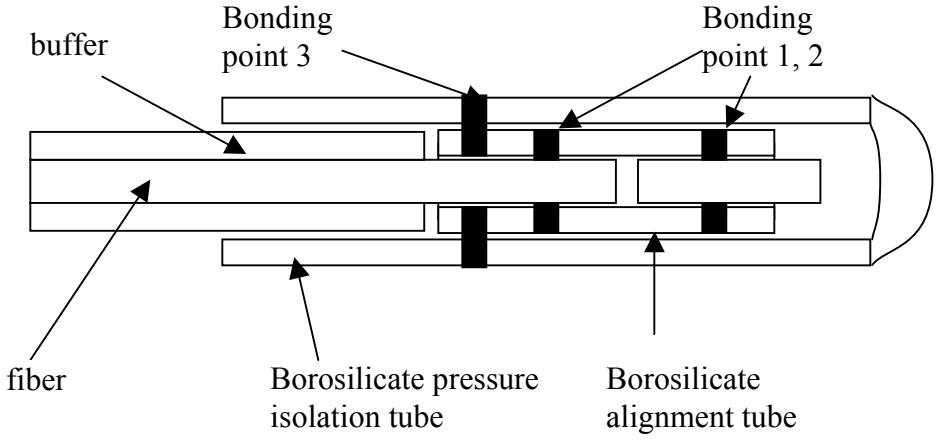

Figure 8.3. Pressure isolating tube of the temperature sensor.

8.4 Temperature Sensor Testing Results

8.4.1 SCIIB thermal stability

The robustness and stability of SCIIB temperature sensors were evaluated under conditions representative of the downhole environment. The experimental setup includes an electrical furnace with a maximum temperature of 1100°C and an Omega CN76000 thermometer to read the temperature at an accuracy of 0.1°C. The SCIIB fiber optic sensor and the thermometer were put side by side in the oven, and the temperature was increased from room temperature to 900°C in steps of 10°C. Both the SCIIB sensor output and the thermometer output were recorded for comparison. The temperature sensor under test had an effective gauge length of 1 mm, and the initial air gap of 5.93 μm. The temperature sensor was tested in the furnace several times. The test results are plotted in Figure 8.4. The sensor successfully survived the test and the output was quite repeatable. The testing results also indicate that the sensor has a very good thermal stability.

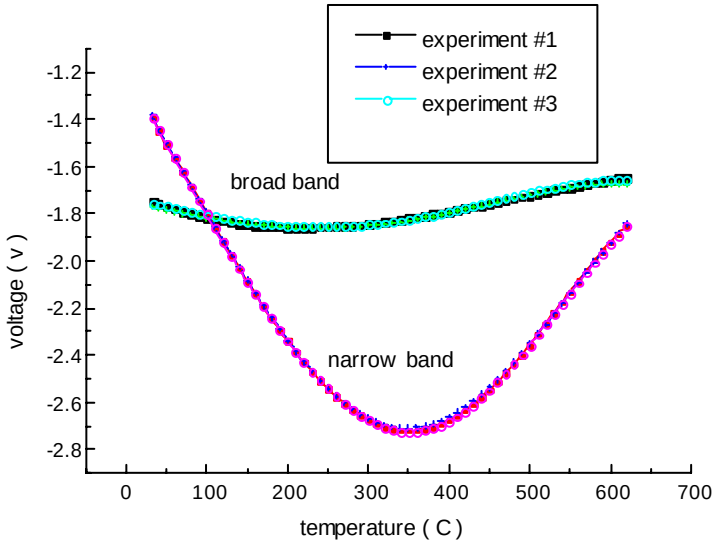

Figure 8.4. SCIIB temperature sensor survivability and stability test results.

8.4.2 SCIIB differential coefficient of thermal expansion (ΔCTE)

The ΔCTE is an important parameter in designing the dynamic range of the SCIIB temperature sensors. Theoretically, the ΔCTE of the sensor can be calculated by referring to the nominal CTEs of the tube material and that of the fibers. However, the actual CTEs of the fiber and the tube can deviate from their theoretical values due to the small chemical or physical differences among the materials used by different manufacturers. Therefore, the precise value of the ΔCTE can only be determined experimentally.

In order to measure the ΔCTE of the SCIIB sensor assembly, we fabricated another sensor with an effective gauge length of 2.5 mm, and an initial air gap length of 5.75 μm. The sensor was tested using the same experimental setup as described in the survivability test. The

sensor output versus the increase of the temperature is plotted in Figure 8.5. Because the sensor had a gauge length longer than the first sensor, when temperature increased, the air gap change covered more than half of an interference fringe. We know that the change from the peak to the valley of an interference fringe corresponds to an air gap change of a quarter wavelength; therefore, the ΔCTE can be calculated by determining the corresponding increase of the temperature between these two points. We used the multimode SCIIB system during the experiments, which has a source central wavelength of 850 nm. The temperature increase from the peak point to the valley point was ΔT=420°C. Therefore, according to Eq. 8-1, the ΔCTE of the sensor is 2.0238×10^{-7}/°C.

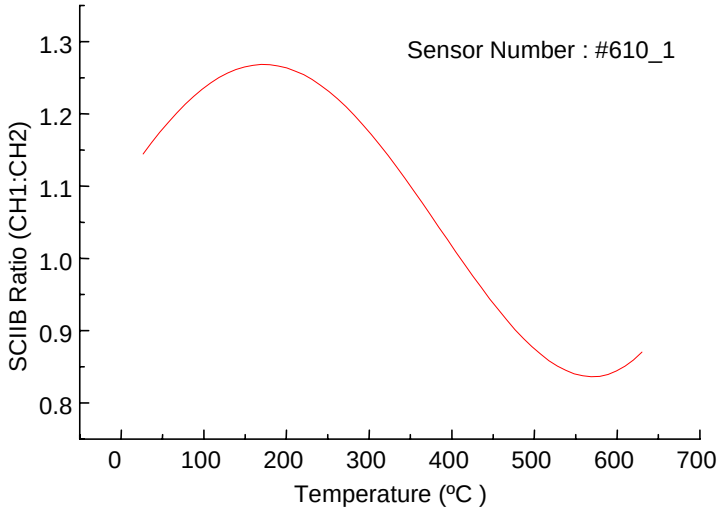

Figure 8.5. Test result used to calculate the ΔCTE of the SCIIB sensor.

8.4.3 SCIIB standard deviation

The standard deviation of the temperature measurement was tested by placing the SCIIB temperature sensor in a controlled environment with a constant temperature. After the temperature of the environment was stabilized, we continuously measured the ambient temperature 100 times. The sensor used in this experiment was a multimode sensor with an effective gauge length of 2 mm and an initial air gap of 5.6 μm. The deviation of the measured data is plotted in Figure 8.6. Based on this data, we conclude that the standard deviation of temperature measurement is σ = 0.0044°C.

8.4.4 White light interferometer temperature sensor

To evaluate the performance of the white light temperature sensor, a type-48000 furnace (Thermolyne Corporation) was used for the temperature test. The temperature range of this furnace is from room temperature to 1200 °C. To increase the resolution of the temperature test, a thermocouple placed beside the FABRY-PEROT temperature sensor was used as the temperature standard. Signals from the thermocouple and the FABRY-PEROT sensor were sampled into the PC synchronously, and a self-developed program was used to evaluate the performance of the temperature sensor.

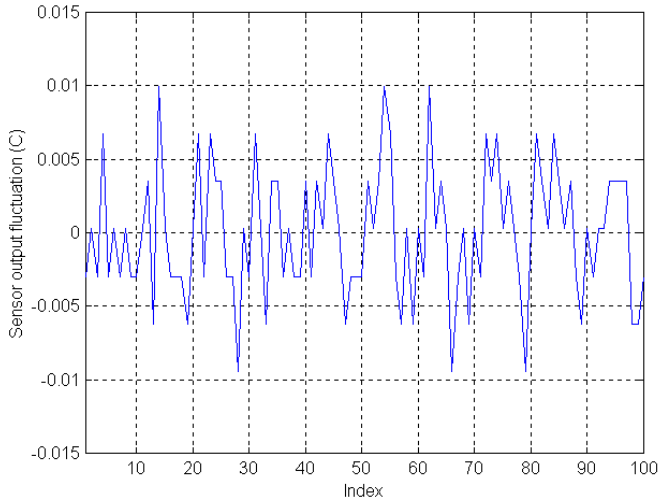

Figure 8.6. SCIIB temperature sensor standard deviation test results.

Figure 8.7 shows a typical testing result of the temperature sensor. While the temperature of the oven increased from room temperature to about 190 °C, the air gap of the sensor head increased from 7 μm to about 16 μm. One difficulty encountered in the temperature testing was the hysteresis effect. In general, a relatively long time period is necessary for the oven to reach a stable temperature. While the heating element is heating, the temperature distribution inside the oven may be large. This induces a hysteresis effect of about 1.5°C between the output of thermocouple and the FABRY-PEROT temperature sensor (Figure 8.8).

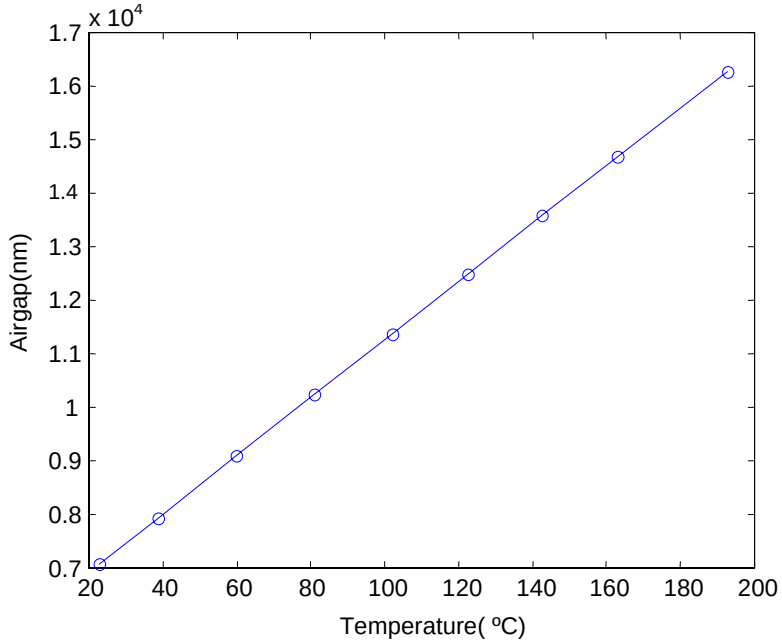

Figure 8.7. Calibration curve of white light temperature sensor.

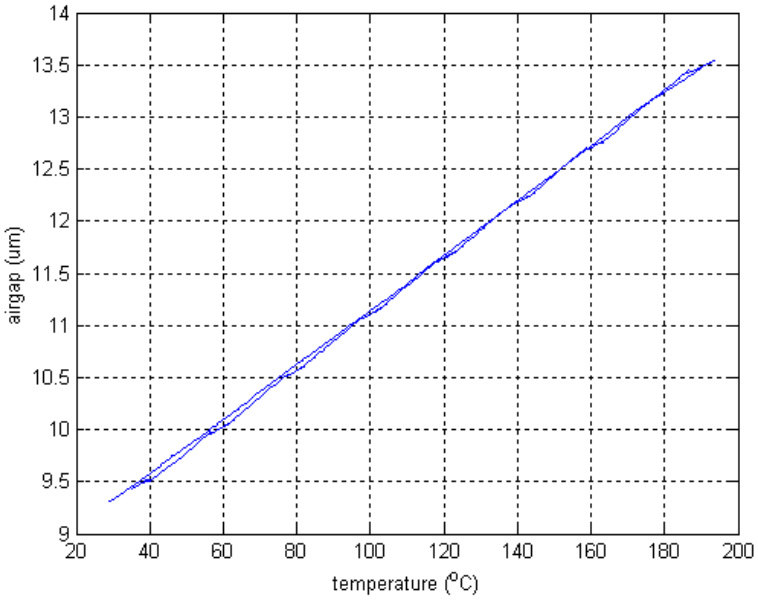

Figure 8.8. Hysteresis effect in temperature measurement.

9.0 Flow Sensors

Monitoring of oil flow velocity in the oil reservoirs with a high accuracy is vitally important for downhole oil exploration and oil recovery applications. Since the FABRY-PEROT sensor scheme has been proven to be effective for highly sensitive and accurate measurement of pressure and temperature, it is thus possible to design flow meters based on the combination of the FABRY-PEROT sensor technology with various mechanical configurations, such as pitot tubes, orifices, thermal dispersion, acoustic dispersion and vortex shedding-induced vibration schemes.

After investigating various flow meter configurations and possible combinations with FABRY-PEROT sensors, the strain-based FABRY-PEROT sensor was chosen for design, fabrication, experimental testing and evaluation to meet the requirements for oil field instrumentation. In this chapter, we report the details of the fiber optic flow sensor system design, fabrication method and test results.

9.1 Flow Sensor Design

Flow rate measurement was achieved by using a Fabry-Perot fiber optic sensor head with the multimode white light demodulating system. Special consideration was given to the requirements for the downhole applications, including temperature stability, high-pressure isolation, high sensitivity, large dynamic range, etc. The basic principle of the self-compensating fiber optic flow sensor is illustrated in Figure 9.1. The system is composed of a sensor probe, optical spectrum analyzer (OSA) for optoelectronic signal processing and a dual core multimode fiber cable linking the sensor probe and the signal-processing unit. The broadband light from two light-emitting diodes (LEDs) is launched into two 3dB 2x2 multimode fiber couplers, which splits each beam into two equal signals. One beam propagates along the lead-in fiber to the sensor head, while the other is terminated at the end-face of one of the coupler's output fibers. The reflected signal from the sensor head also propagates along the same fiber to the same coupler, and then both of the light beams are detected by the fiber optic spectrometer. A multimode white light interferometric spectrum analyzer is used to obtain the flow rate by demodulating the light signal fringes from the detected spectrums.

The configuration of the fiber optic flow sensor head shown in Figure 9.1 is a combination of the broadband white light interferometer and cantilever beam designs. Based on the strain principle of cantilever beams [4], the flow rate can be determined by detecting the air-gap changes from two fiber sensors caused by the bending of the cantilever beam. The sensor head is fabricated by bonding two identical fiber optic tube-based sensors on a cantilever-beam. Each sensor is fabricated by inserting two fibers into a fused silica hollow glass tube. The process is somewhat different from normal tube-based fiber optic sensor fabrication [5],

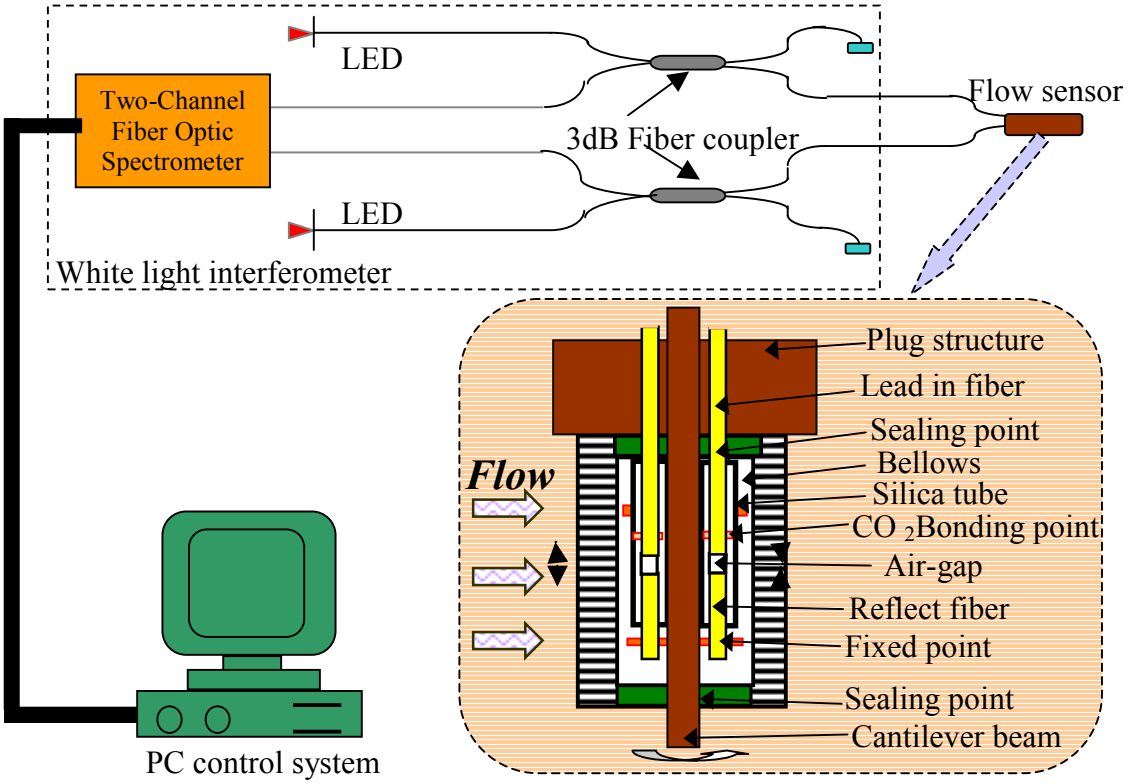

Figure 9.1. Fiber optic flow sensor system.

because while one end of the capillary tube is thermally bonded to the lead-in fiber, the reflecting fiber is left free to move in the other end of tube. Therefore, an air gap is formed between the two cleaved fiber end faces. The sensor fabrication process is then repeated for the other side of the beam. Both ends of the tube and both reflecting fibers are firmly bonded to the metal cantilever beam at a predetermined gauge length. This allows the air gap to change freely without restriction by the capillary tube and only related with the changes in bending of the cantilever beam caused by the flow rate of the fluid. This dual sensor combination is then inserted into the central hole of a metal tube or plug, which allows easy installation of the sensor plug into the flow pipes for measurement. Finally a small metal bellows is used to cover the beam and sensors. This bellows allows the flow to bend the cantilever beam located inside without allowing the fluid to contact the cantilever beam or sensors. In this manner, the sensor can be isolated from the fluids (which may be corrosive) in the outside environment. When the fluid flows past the sensor, the cantilever beam will be bent by the force caused by the momentum of the fluid passing the beam.

When a fluid impinges on the beam, all its momentum can be considered converted into force, which can be expressed as

$$F \times t = m \times v \qquad (9\text{-}1)$$

where F is the force on the cantilever, t is the unit of time, v is the velocity of the fluid, and m is the quantity of the passing fluid within the unit time. These quantities are related as follows.

$$\begin{cases} m = \rho \times V \\ V = S \times v \times t \\ S = c \times L \end{cases} \quad \textbf{(9-2)}$$

where ρ is the density of the fluid, V is the volume of flow in unit time; S is the area of the cantilever beam, c is width of cantilever, d is thickness of cantilever, L_b is the length of the cantilever beam. From Eq. (9-1) and (9-2) the applied force per unit time t is:

$$F = \rho \times c \times L_b \times v^2 \quad \textbf{(9-3)}$$

Suppose F is a uniform force, the maximum strain ε will be at the fixed end of the cantilever

$$\varepsilon = \frac{6FL_b}{Ecd^2} \quad \textbf{(9-4)}$$

where E is theYoung's modulus. When the flow passes by, because each of the sensor's free fibers are bonded to cantilever, bending of the beam will be manifested as an air gap change. The air gap variation caused by the gauge length change ΔL between the two bonding points can be represented as

$$\Delta L = \varepsilon \times L \quad \textbf{(9-5)}$$

where L is the gauge length between two bonding points. Then from Eq. (9-2) to (9-5), we obtain

$$\Delta L = \frac{6\rho v^2 L_b{}^2 L}{Ed^2} = \beta(v) \quad \textbf{(9-6)}$$

where β denotes the relationship between the air-gap change ΔL and the velocity of the flow v.

When the cantilever-beam bends due to the flow of the fluid, the air-gap of the sensor on the side facing the fluid flow will increase, while the air-gap of the sensor located on the opposite side of the cantilever beam will decrease. For a given material, the volume compressibility and thermal expansion should be approximately linear for small pressure and temperature changes. Therefore, when fluid passes by the sensor, the air gap of both sensors will change but in opposite directions. However, both sensors will have the same magnitude and direction of air gap change due to the temperature and pressure changes:

$$\begin{cases} \Delta L_1 = a_1 \Delta T + K a_1 \Delta P + \beta_1(v) \\ \Delta L_2 = a_2 \Delta T + K a_2 \Delta P + \beta_2(v) \end{cases} \quad \textbf{(9-7)}$$

where ΔL_1, ΔL_2 represent the gauge length changes of the two sensors, α_1, α_2 are the temperature effects of the two sensors, K is the relationship between the effects of thermal extension and pressure extension, and β_1, β_2 refer to the flow coefficients of the two sensors as shown in Eq.(9-6). We can cancel the effects from temperature and pressure based on the

above equations to obtain the relationship F between the flow rate and system output based on the two air-gap changes.

$$F(v) = a_2 \Delta L_1 - a_1 \Delta L_2 = a_2 \beta_1(v) - a_1 \beta_2(v) \qquad \textbf{(9-8)}$$

From Eq. (9-8), we can see that by analyzing the outputs of the two sensors, this sensor system can detect the applied flow velocity while being insensitive to pressure and temperature changes by automatically compensating for temperature and pressure effects. If we select the cantilever-beam to be brass with $E = 4.2 \times 10^{10}$ kg/m^2, $L_b = 25mm$, $c=5mm$, $d=0.5mm$, and the two fiber sensors with gage length of $L=20mm$, original air gap of a= $12.00mm$, then the relationship between the air gap changes and the applied flow velocity can be calculated as shown in Figure 9.2. According to this simulation, we can see that when the cantilever beam temperature is changed, both the front and back sensor air gaps are affected, causing the relationship between sensor output and the applied flow rate very repeatable, which illustrates that the sensor can compensate for temperature automatically.

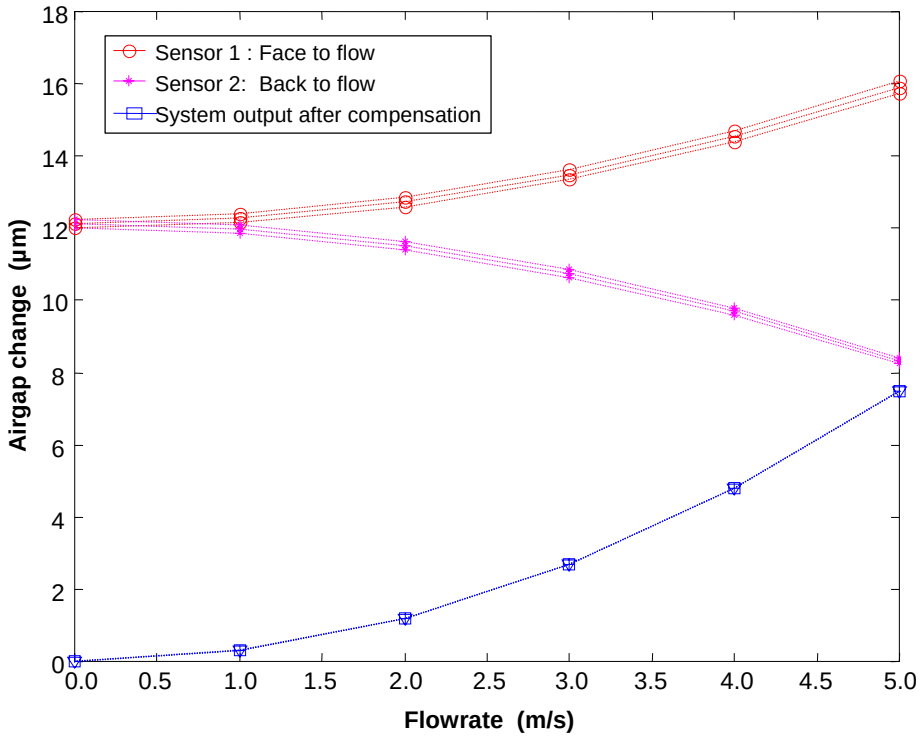

Figure 9.2. Simulation of flow sensor self-compensation.

In industrial practice, flow measurements are usually used to obtain the flow rate rather than the flow velocity, so the related cross sectional area of the flow pipes must be added to Eq. (9-8) to obtain the relationship between the air gap changes and flow rate. It is also possible that the relationship between air gap changes and flow velocity will differ from the theoretical value due to materials processing and fabrication techniques, but these factors can all be combined within Eq. (9-8) and will be adjusted for during system calibration.

9.2 Flow Sensor Construction

The prototype flow sensor system was constructed as shown in Figure 9.1. A dual channel white light interferometer system was used for optoelectronic signal processing. Two Honeywell 4854 LEDs with center wavelengths around 850nm pigtailed with standard 50/125 multimode fibers were used as broadband light sources. A PC-2000 dual-channel fiber optic spectrometer from Ocean Optics, Inc. was used to detect the optical signals from the sensor head, and its output fed to the flow rate measurement control system based on a multimode white light interferometric spectrum analyzer.

The analysis described in the previous section provides a clear guide to the design of the fiber optic sensor for flow detection. The fabrication technique was gradually improved through experience after making many sensor heads. Due to Invar's low coefficient of thermal expansion (CTE) (1.05×10^{-6}/ºC), which is much lower than most conventional metals and closer to fused silica [6], an Invar sheet from Electronic Space Products International, Inc was selected for the cantilever-beam and cut, polished and annealed. The inner diameter of the hollow fused quartz tubing was chosen to be 132mm, which limits the movement of the multimode fiber (125mm) to 5mm. PN-231 regular Nickel bellows from *Servometer, Inc*. were used for the packaging of the flow sensor. The size of the Invar cantilever beam was selected as 3mm × 30mm. Based on the working range and resolution of the multimode white light system [7], the thickness of the invar sheet, the gauge lengths and the original air-gaps of both fiber sensors were adjusted to maximize the visibility of both sensors through the complete measurement range. Also the gauge length was selected to be as small as possible to decrease the inherent thermal expansion. In fiber fabrication, the initial air gap between both fiber end-faces was adjusted to obtain the highest interference fringe visibility. The fabrication process is shown in Figure 9.3a and b; the photograph of the finished flow sensor is shown in Figure 9.3c; the sensor plugged into its fitting for testing or measurement is shown in Figure 9.3d. Both the lab-scale testing and field-testing have been performed to evaluate the prototype flow sensor system, as described in the following sections.

9.3 Lab-Scale Experiments and Results

Evaluation and testing of the flow sensors is necessary to improve the flow sensor design and fabrication. The lab-scale test system was set up as illustrated in Figure 9.4. This experimental set-up includes a FT-24NENW turbine flow meter, purchased from *Flow Technologies Inc.* For 1-1/2" pipe sizes, the custom ordered calibration flow rate range is from 1.6 to 90 GPM, the repeatability is ±0.05% of the full range, and the linearity is ± 0.5% of reading. A ¼ HP *Wayne* submersible utility pump was used to drive the water through the PVC pipes; with 1-1/2"pipe, the maximum flow rate should be 18.5GPM. A *DPF700* meter from *Omega, Inc* was ordered with a RS-232 option board to connect to a laboratory computer for preliminary flow rate testing. Both the fiber optic sensor and the thermometer were put into the testing pipes, and the pumped flow rate adjusted by changing the input of the electrical pump. Both the flow sensor output and the flow meter output were recorded for comparison. The testing system at CPT is shown in Figure 9.5.

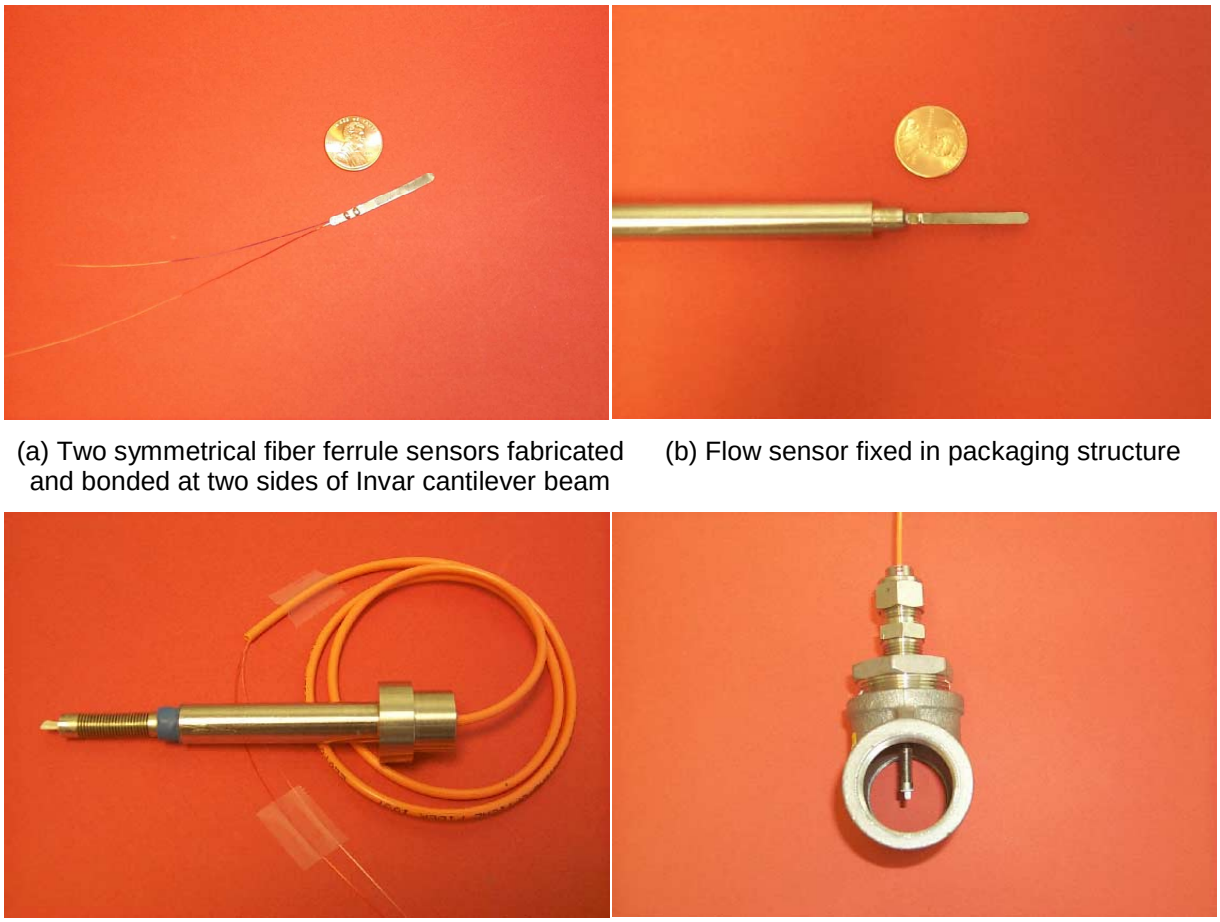

(a) Two symmetrical fiber ferrule sensors fabricated and bonded at two sides of Invar cantilever beam

(b) Flow sensor fixed in packaging structure

(c) Prototype fiber optic flow sensor

(d) Flow sensor fixed into T-fitting

Figure 9.3. Fabrication of flow sensor.

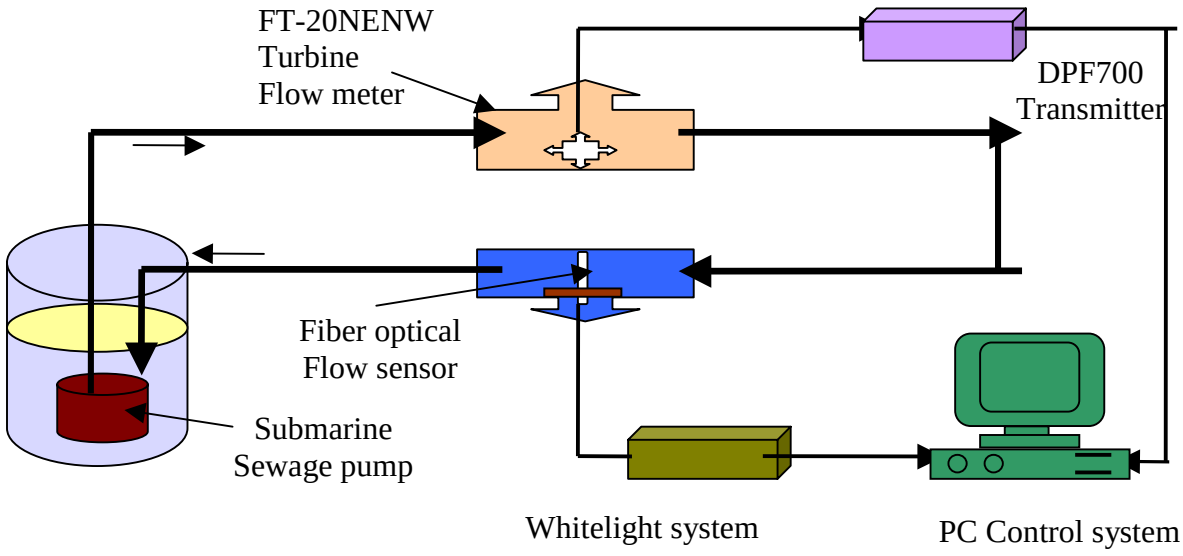

Figure 9.4. Lab-scale flow testing system setup.

(a) Lab-scale flow testing system loops

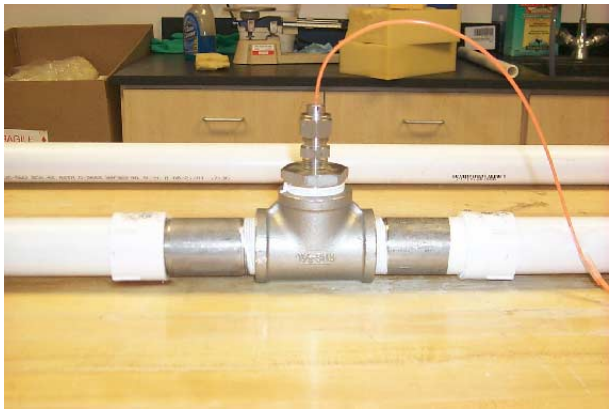

(b) Flow sensor deployed in testing

Figure 9.5. Flow sensor testing setup in Center for Photonics Technology, Virginia Tech.

Using this testing system, numerous experiments have been outperformed to evaluate the performance of the designed flow sensor system. The normal test temperature range was from 18~45°C with normal atmospheric pressure. The results shown below were obtained using the fiber optic flow sensor whose parameters are shown in Table 1.

Table 9.1. Parameters of fiber optic flow sensor used for lab scale testing.

Fiber type:	Multimode 50/125
Cantilever beam material:	Invar sheet
Cantilever beam size:	0.010"*1.5*0.13"
Original air gaps of two sensors:	9.211μm; 8.810μm
Original visibility of two sensors:	67%; 69%
Gauge length of two sensors:	1.8mm; 2 mm
Relative temperature coefficients:	0.9; 1
Sensor protection:	Flexible Ni-bellows

9.3.1 Sensor calibration

Sensor calibration is very important for sensor evaluation and application. It is usually conducted by applying known flow rates within its operating range to obtain the calibration curve, or one-to-one relationship between the original sensor output and the applied flow rate, which can be stored in the host computer and later used to convert sensor output to the flow rate reading. To ensure the calibration accuracy, the flow rate was held at each step for about three minutes before moving to the next step during the calibration process. By averaging the output of both the flow meter and flow sensor at each step, errors can be minimized. The original data is shown in Figure 9.6. Because the temperature effect coefficients (TEC) were determined by testing prior to sensor calibration (Table 9.1), Eq. (9-

1)~(9-3) were used to cancel the temperature effects. The compensated output is shown in Figure 9.6 and used to obtain the flow sensor calibration curve shown in Figure 9.7. In general, the calibration curve was obtained by taking the average of several consecutive sets of calibration data to further ensure the calibration accuracy and to generate the coefficients of calibration.

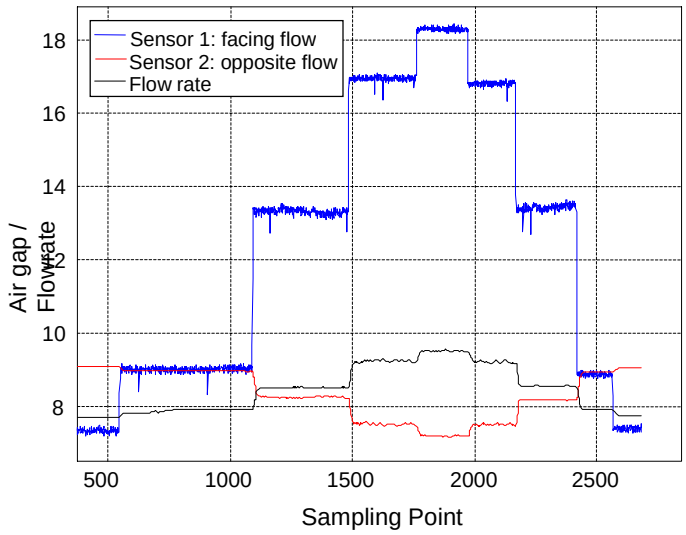

Figure 9.6. Relationship between flow rate and flow sensor air gaps.

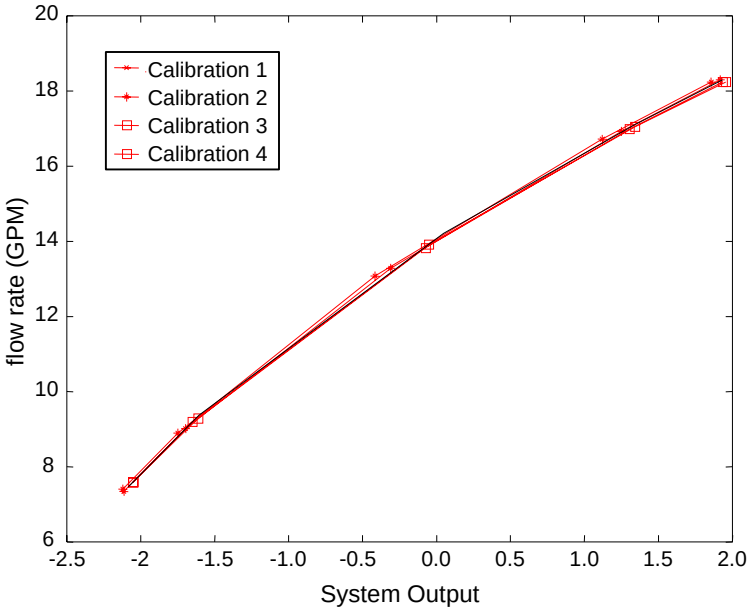

Figure 9.7. Flow sensor calibration curve.

9.3.2 Temperature compensation

Temperature dependence is critical for flow sensors used in oil field environment. It is a great challenge to design a flow sensor to have minimum (ideally zero) temperature dependence. With the self-compensation design as described in Section 2, it is possible, in theory, to have very small or even zero temperature sensitivity. Figure 9.8 shows the temperature independence characteristic of the flow sensor. Even though the environmental temperature changes from 23ºC (squares) to 45ºC (stars), the output of the fiber flow sensor matched the applied flow rate with high repeatability, indicating that this sensor design can compensate the temperature changes automatically, consistent with the theoretical analysis.

9.3.3 Measurement results

Using the calibration curve or coefficients, the fiber optic sensor was used for flow rate measurement and the results compared with the flow rate output from FT-24NENW flow meter in Figure 9.9.

9.3.4 Repeatability

Sensor repeatability can be determined by applying a preset flow rate repeatedly from one direction (increasing or decreasing). The largest difference in the sensor output readings can be used to specify the repeatability of the sensor. Under different water temperatures, four measurements up to the full operating range of the sensor were performed with the results shown in Figure 9.10a. For comparison purposes, the original calibration data is also shown. The deviation of the two measurements with respect to the calibration data is plotted in Figure 9.10b. The maximum deviation between the measured pressure and the calibrated pressure was within ±0.3GPM. The normalized repeatability of the sensor system with respect to its dynamic range was therefore ±1.62% of the full scale. This test also demonstrates that this sensor design can effectively compensate for temperature influences.

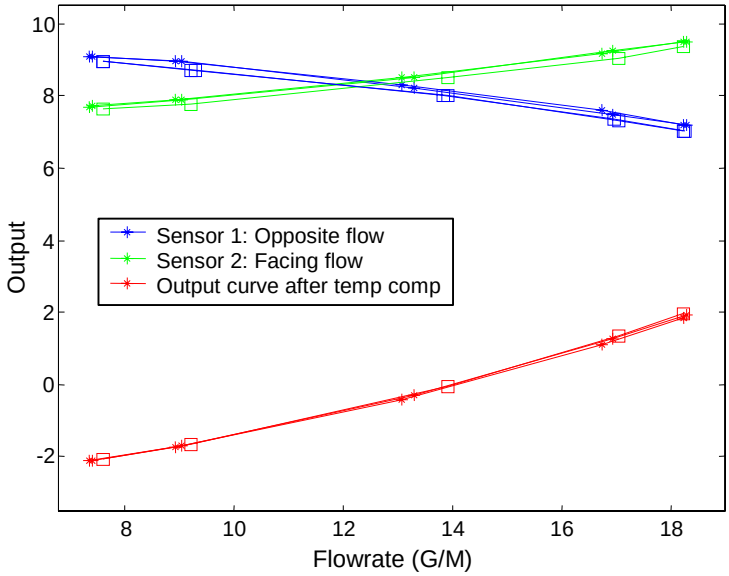

Figure 9.8. Fiber optic flow sensor self-compensation result.

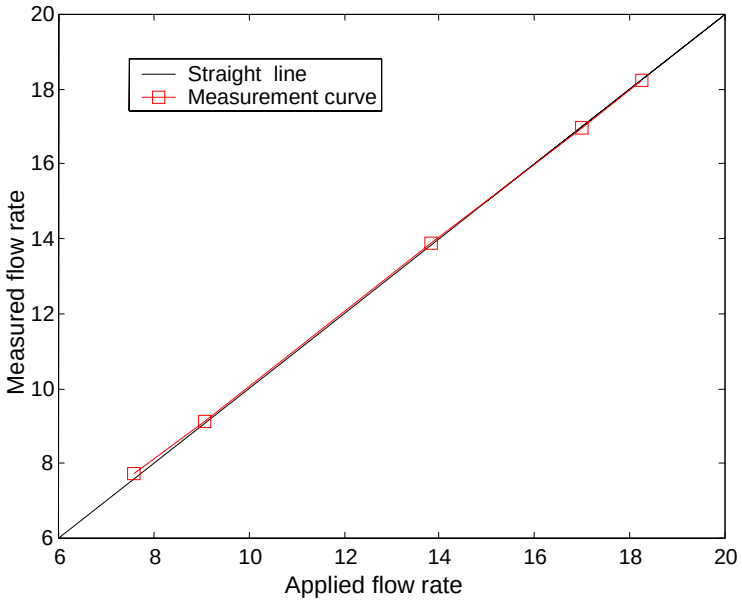

Figure 9.9. Flow sensor system calibration lines.

9.3.5 Dynamic flow measurements

To demonstrate the sensor's dynamic response, the calibrated flow sensor was tested under dynamic flow conditions. The reference flow signal was provided by the FT-24NENW Turbine flow meter. Comparison of the output of both the fiber optic flow sensor and flow meter shown in Figure 9.11 reveals that the fiber optic sensor matches the turbine flow meter very well.

9.3.6 Resolution of flow rate measurement

The resolution of a sensor system is usually interpreted as the standard deviation of a series of flow measurements. It is common to use twice the standard deviation as the direct measure of resolution. Evaluation of the flow sensor resolution was performed using a calibrated sensor. The sensor was placed in the testing pipe and the data from the test system was sampled at a rate of 60 samples per second for one minute, which should be sufficient compared to the system's frequency response of 10Hz. The flow rate measurement outputs within the one-minute sampling period are plotted in Figure 9.12. The standard deviation of the flow data within this time period was calculated to be σ=0.0097GPM. Therefore the resolution of the sensor system was estimated to be 2σ=0.0194GPM. The normalized resolution with respect to the dynamic range of the system was 0.11% of full scale.

9.3.7 Hysteresis of flow rate measurement

The hysteresis of the flow sensor can be measured by cycling the applied flow between the minimum and the maximum of the operating range in both increasing and decreasing directions. The hysteresis can be calculated as the largest difference between the output readings of the pressure cycles. Experiments were conducted to evaluate the actual hysteresis

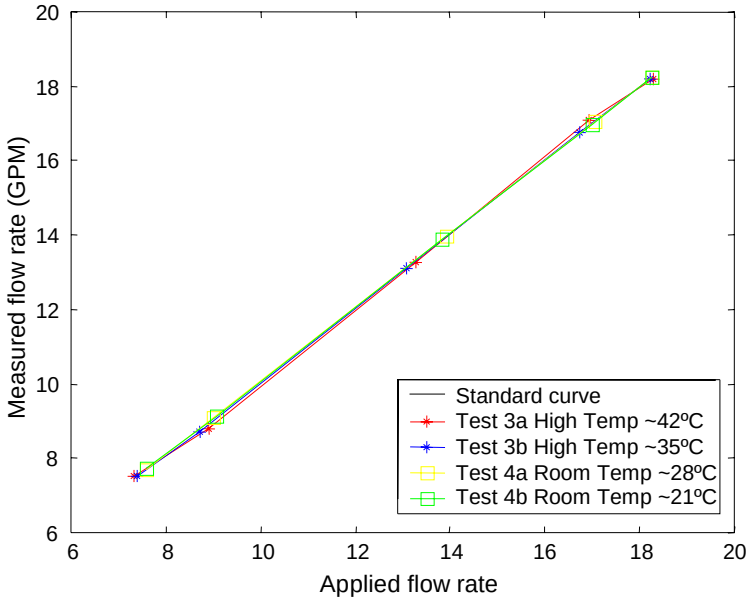

(a) Flow measurement repeatability results.

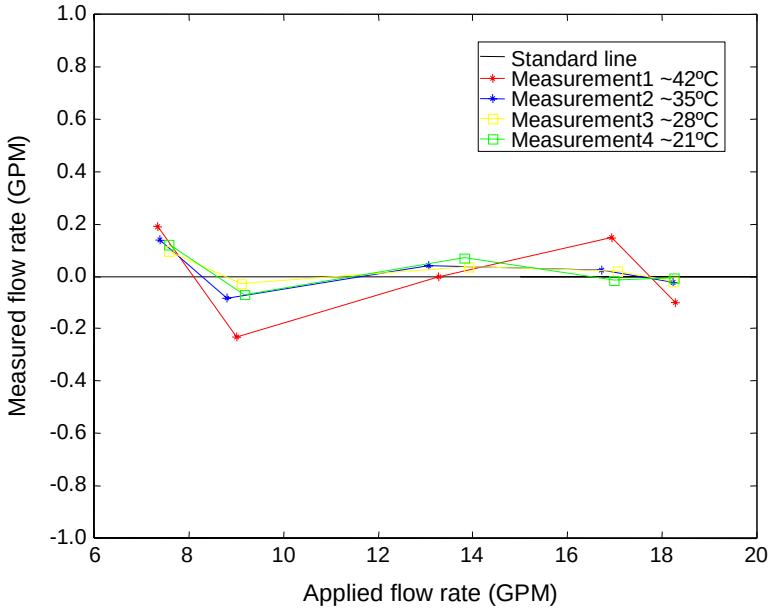

(b) Deviation of the measured flow with respect to the calibration data.

Figure 9.10. Flow measurement repeatability test results.

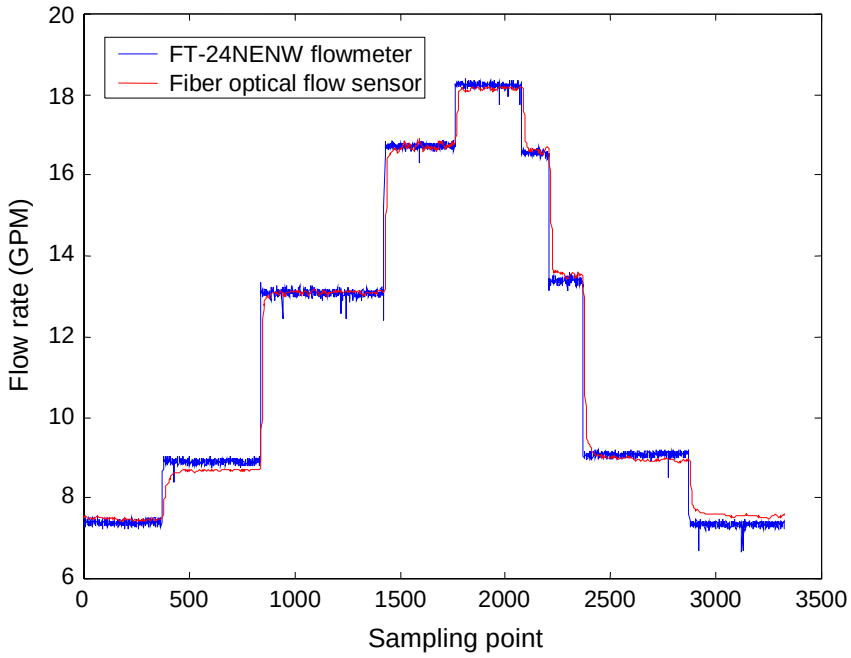

Figure 9.11. Dynamic response of flow sensor.

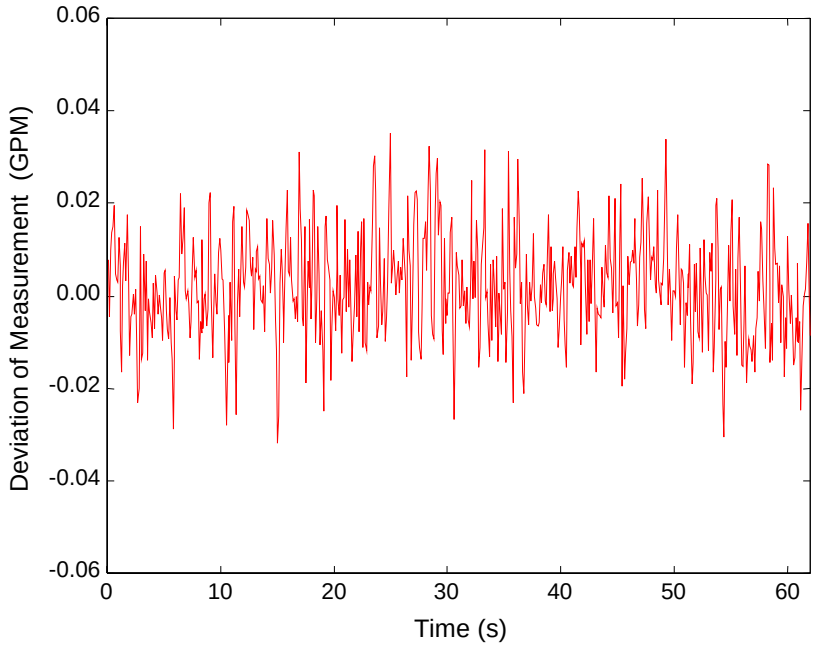

Figure 9.12. Resolution of flow sensor system.

of the flow sensor probe. The evaluation was conducted using the same flow testing system after the sensor system was calibrated. The applied flow was first increased to the maximum operating range of 18.5GPM, and then decreased after it was maintained at 18.5GPM for 30 minutes. The experimental results shown in Figure 9.13 demonstrate that the hysteresis of the full operating range is less than 1.35%.

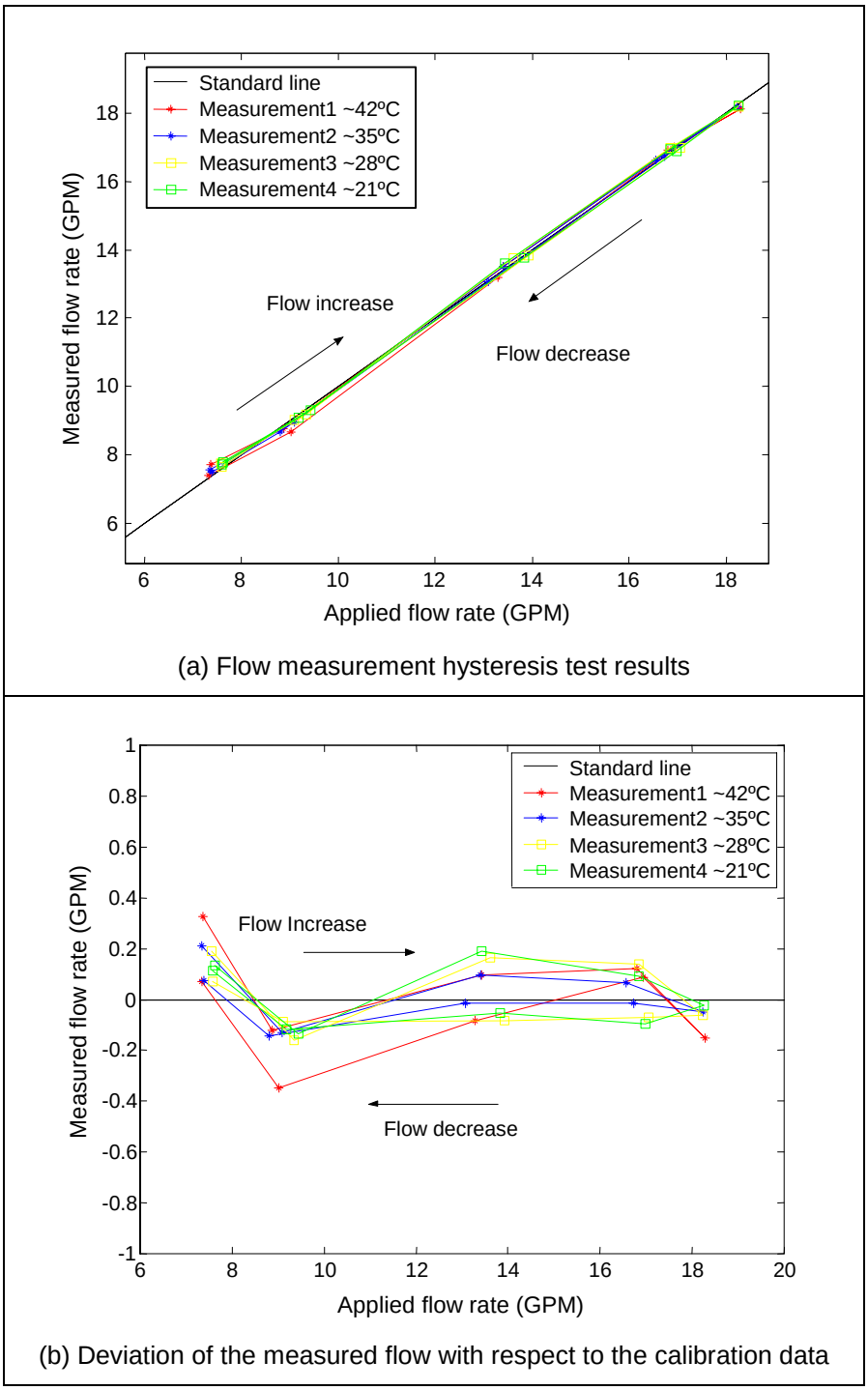

Figure 9.13. Hysteresis of flow sensor in lab-scale testing.

9.3.8 System stability test

The same flow sensor was also used to test the system stability. The sensor was kept in the flow-testing loop for 12 hours while the flow was maintained at 7.2GPM. The data acquisition system was programmed to sample the sensor's output every 10 seconds. The test results are shown in Figure 9.14. Processing the data revealed that the maximum peak-to-peak pressure variation within the 12-hour time period was 0.35 GPM. The data also showed that the output from FT-24NENW flow meter exhibited many discontinuities and fluctuations, which limited the evaluation of flow sensor performance. Thus we believe that the maximum variation was less than 1.89% of the full dynamic range.

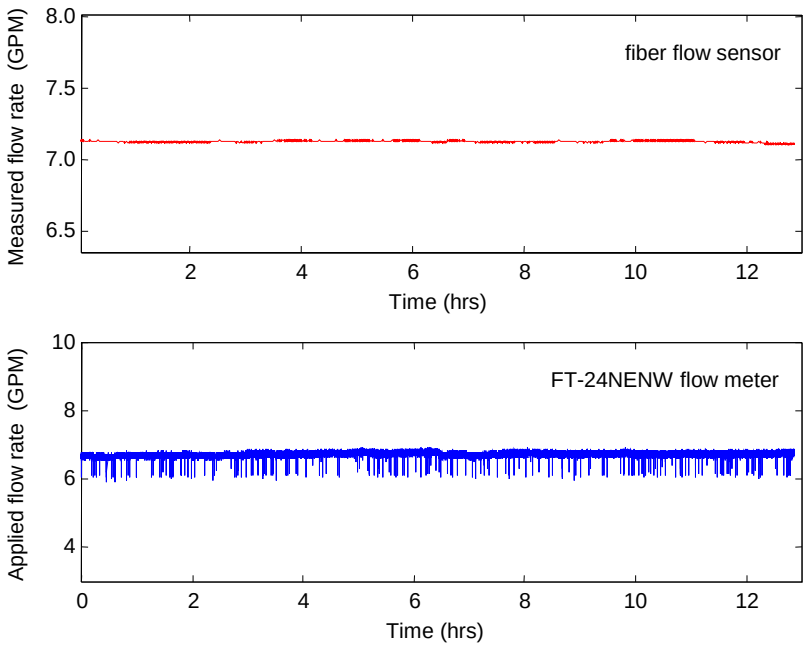

Figure 9.14. Flow sensor system stability test over 12 hours at 7.2 GPM.

10.0 Acoustic Sensors

Acoustic (or seismic) signals are another very useful piece of information in downhole oil recovery. An acoustic wave propagating in the oil reservoir can generate a pressure signal (generally small in amplitude) that can be detected using a fiber optic sensor with a high sensitivity to pressure fluctuations and a high frequency response. In this chapter, the design and implementation of the acoustic sensors is presented.

10.1 Principle of Operation

The basic principle and configuration of the diaphragm-based fiber optic acoustic sensor can be illustrated using Figure 10.1. The system consists of a sensor probe, a light source, an optoelectronic signal processing unit, and an optical fiber linking the sensor probe and the signal-processing unit. As shown in the enlarged view of the sensor head, the input fiber and the thin silica glass diaphragm are bonded together in a cylindrical silica glass tube to form a Fabry-Perot sensing element.

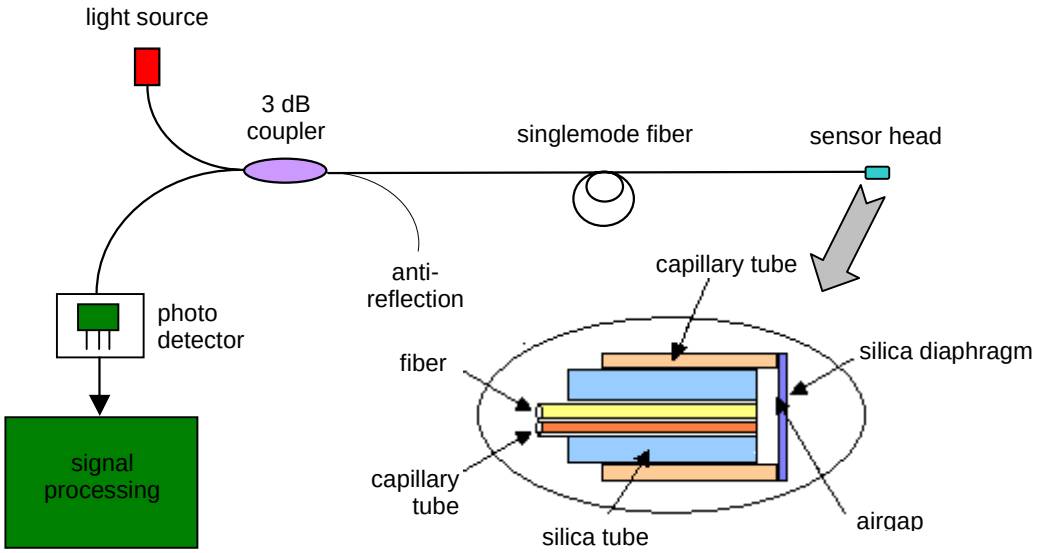

Figure 10.1. Illustration of the principle of the diaphragm-based fiber optic acoustic sensor.

The small pressure generated by an acoustic signal causes a deformation of the diaphragm and modulates the sealed air gap length. Similar to other interferometers, the acoustic fiber optic measurement exhibits very high sensitivity. As discussed previously, the measurement would suffer from the disadvantages of sensitivity reduction and fringe direction ambiguity when the sensor reaches peaks or valleys of the fringes. Therefore the dynamic range of the sensor is controlled through the sensor design and bonding technique used to fabricate the acoustic sensor so that the sensor operates only over the linear range of a half fringe,

corresponding to roughly a quarter fringe. As shown in Figure 10.2, the initial operating point is chosen to be at the center point of the interference fringe, and the thickness of the diaphragm is designed in such a manner that the imposed acoustic signal only deforms the thin diaphragm within the linear part of the sensor response curve. Therefore the sensitivity reduction and fringe direction ambiguity problems can be completely avoided.

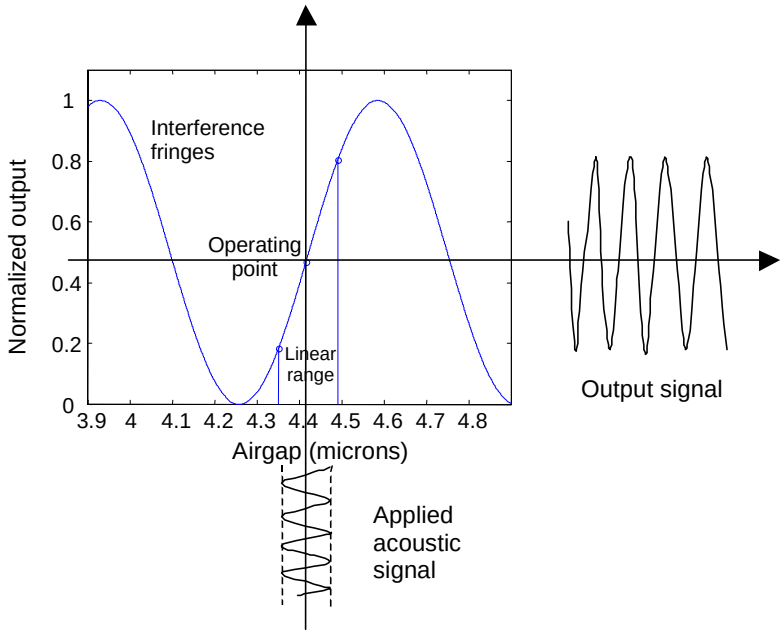

Figure 10.2. Illustration of a linear operating range of the sensor response curve.

It deserves special mention here that parallel to the fiber, a capillary tube placed through the inner hole of the ferrule is used as a pressure filter to transfer the pressure effect between the cavity and the outside. This acts as a mechanical high pass filter such that slowly varying pressure signals do not affect the diaphragm displacement. The reason is that the capillary tube is open to the outside environment. As the pressure outside the sensor increases, the pressure inside the sensor slowly equilibrates through the capillary tube. Because the inner diameter of the capillary tube is small, high frequency signals such as the acoustic signal have pressure cycle variations that are too fast for the capillary tube's small diameter allow equilibration. Therefore, the capillary tube "screens out" the slowly varying pressure cycles. This is particularly useful in the downhole environment where the pressures can become quite high and yet the acoustic signal pressure is so low.

10.2 Sensor Frequency Response and Sensitivity Design

We can use the structure shown in Figure 10.3 to model the acoustic sensor. The diaphragm vibrates in the presence of an acoustic wave as it imposes a dynamic pressure on the diaphragm. It is very important to design the sensor head to ensure high enough frequency response and sensitivity to achieve optimum detection of the acoustic signals.

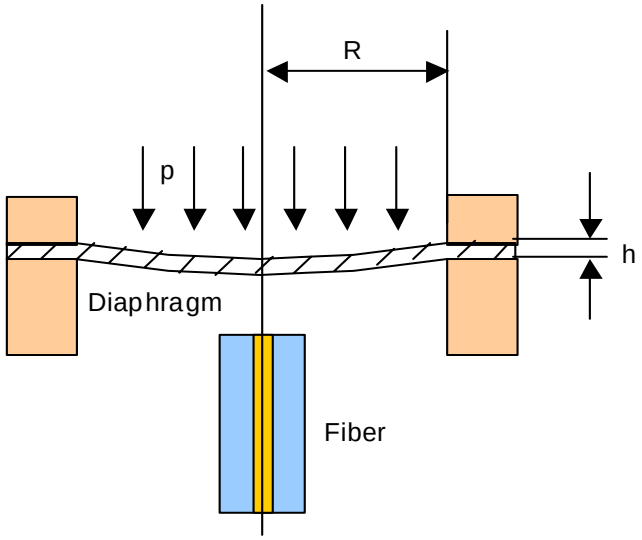

Figure 10.3. Structure model for diaphragm-based acoustic sensor.

The frequency response of the sensor is limited by the natural frequency (f_n) of the diaphragm. The natural frequency can be calculated by the following equation [8]:

$$f_n = \frac{\alpha}{2\pi R^2} \times \sqrt{\frac{Dg}{hw}}, \qquad \textbf{(10-1)}$$

where α is a constant related to the vibrating modes of the diaphragm, and takes a value of 10.21 for the fundamental mode; R is the effective radius defined by the inner diameter of the silica sensor glass tubing; h is the thickness of the diaphragm; g is the gravitational constant; w is the specific weight of the diaphragm material (for fused silica at 25 C°, 2.202×10^3 kg/m^3); and D is the flexural rigidity of the diaphragm defined by

$$f_n = \frac{\alpha}{2\pi R^2} \times \sqrt{\frac{Dg}{hw}}, \qquad \textbf{(10-2)}$$

where μ is the Poisson's ratio (μ = 0.17 for silica glass material at 25°C); E is the Young's modulus of the silica glass material (E = 73.73 GPa or 7.49×10^9 kg/m^2 at 25°C); The frequency response of the sensor can thus be calculated by combining Eq. (10-1) and (10-2) into

$$f_n = 2.749\times10^9 \frac{h}{R^2} \text{ (Hz)}, \qquad \textbf{(10-3)}$$

where h and R are in microns. As indicated by Eq. (10-3), the frequency response is proportional to the thickness of the diaphragm and inversely proportional to the square of the effective diaphragm radius. If we choose a diaphragm with an effective radius of R=1mm, we can plot the predicted frequency response of the sensor as a function of diaphragm thickness as shown in Figure 10.4. So for a 100 μm-thickness diaphragm, the theoretical natural frequency response in air should be 274.9kHz. So any acoustic signals under this frequency can be detected by this diaphragm-based sensor.

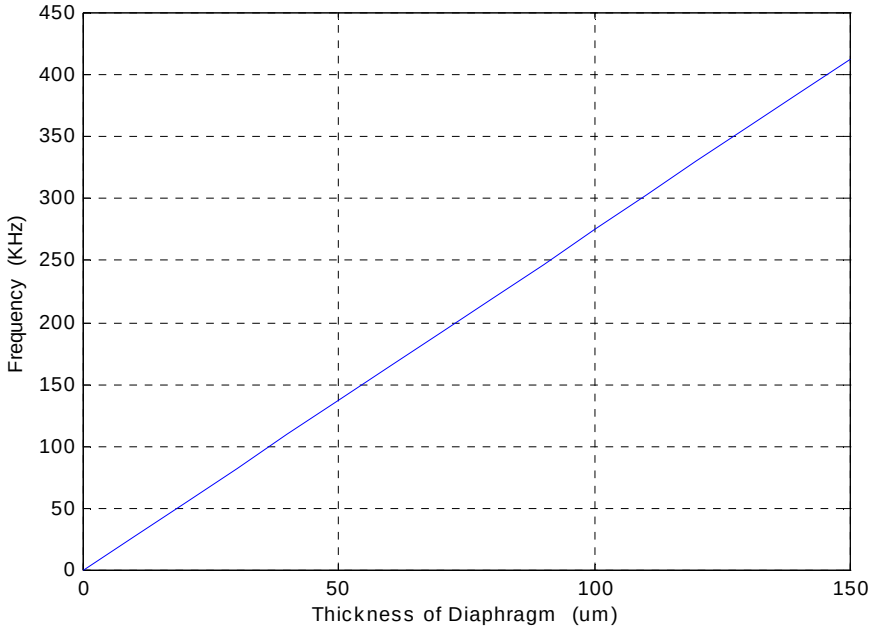

Figure 10.4. Predicted frequency response of the sensor at *R=1*mm.

The diaphragm will be deflected when there is a differential pressure p between the inside and outside of the sealed cavity. The out-of-plane deflection of the diaphragm y as a function of the pressure difference at any radial position r is given by [8]

$$y = \frac{3(1-\mu^2)p}{16Eh^3} \times (R^2 - r^2)^2 . \qquad \textbf{(10-4)}$$

In our sensor configuration, the fiber is positioned in the central part of the diaphragm so that only the center deflection y_0 is of interest, which is given by

$$y_0 = 1.71 \times 10^{-8} \frac{R^4}{h^3} p , \qquad \textbf{(10-5)}$$

where again, y_0, R and h are all in microns, and p is in pounds per square inch (*psia*). From the above equations, it is evident that the sensitivity of the sensor can be designed to fit different application requirements either by choosing diaphragm materials with different μ and E or by changing the geometric parameters of the sensor head with the desired effective diaphragm size R and thickness h. In general, a diaphragm with a larger radius and a smaller thickness will yield a higher sensitivity to the detection of the acoustic signals. However, as indicated above, the operating range of the acoustic sensor head needs to be limited within the linear range, which is a fraction of an interference fringe in order to avoid the sensitivity reduction and fringe direction ambiguity problems. This imposes a limitation on the thickness of the silica diaphragm. Figure 10.5 shows the sensor response with R=1mm, as predicted by Eq. (10-5). For a 100μm thick diaphragm, the theoretical pressure sensitivity in air should be 0.017um/psi.

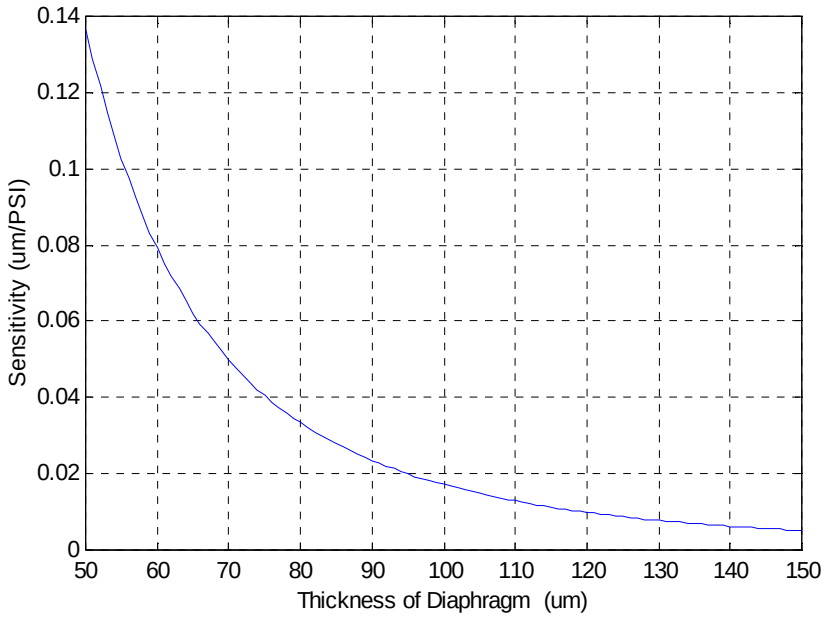

Figure 10.5. Theoretical sensor response (μm/ psi) versus diaphragm thickness at *R*= 1mm.

10.3 Acoustic Sensor Fabrication

As discussed in Chapter 7, the pressure sensor head is fabricated by bonding a silica fiber, ferrule, tube and diaphragm together to form an interferometer with a sealed cavity. To achieve high temperature stability, a uniformly strong bond is necessary among these four components. There are several challenging requirements in the acoustic sensor fabrication. First, the fabricated sensor should have an initial air gap allowing the sensor operating point to be located in the center of the linear part of an interference fringe. This requires precise air gap control and adjustment during the sensor fabrication. Second, the sensor operation requires a stable operating point to eliminate the sensitivity degradation and phase ambiguity problem. Therefore, the components used to make the acoustic sensor need to be made of the same or closely matched material so that the thermal stability of the sensor is ensured. Third, the sensor is intended to be used in the downhole environments; therefore for hydraulic deployment, the overall size of the sensor needs to be very small. To satisfy those special requirements, we investigated several sensor fabrication techniques including the epoxy-based sensor fabrication, the solder bonding method, and the controlled thermal bonding method. Although the first two methods appear to be relatively easy, the sensor performance doesn't satisfy the requirements. We therefore focused our research effort on the third method: controlled thermal bonding techniques

10.3.1 Epoxy-based sensor fabrication

The white light fiber interferometric system was used to monitor the change in air gap in the sensor head. Because the tunable laser is used as the light source, the original air gap of the sensor can be selected at any effective value to ensure that the sensor head will have sufficient visibility to detect the acoustic waves. The fabrication steps include 1) polish the

end of singlemode optical fiber, silica ferrule and silica tube separately; 2) place the diaphragm above the flat endface of the tube and bond them with Epoxy-907; 3) place the fiber and the capillary tube at the same time through the silica tube; ensure that the end faces of extend out of the ferrule, then bond them together; 4) when both are dry after the solidification time, place them into the silica tube, adjust the distance between the fiber's endface and diaphragm carefully to obtain high visibility, and bond the diaphragm when a suitable interference air gap is found using Epoxy-907. The air gap and visibility of the sensor head will change during the solidification, but usually by adjusting the laser wavelength of the tunable laser, a suitable air gap can still be found.

10.3.2 Direct thermal bonding method

The mechanism on which the direct thermal bonding method is based is similar to that of the SCIIB sensor bonding.. When using thermal bonding for sensor fabrication, it is very important to have precise temperature control. Temperatures that are too high could warp or melt the material and damage the structure of the components. On the other hand, temperatures that are too low could result in poor bond strengths.

Using methods similar to the SCIIB sensor fabrication, we use a CO_2 laser as the heating source to fabricate the acoustic sensor because of the small sensor size and the ability to focus the laser output to a small spot. Silica glass materials have very high absorption coefficient at the typical CO_2 laser wavelength (10.6 μm). The optical energy will be transferred to heat, and will raise the temperature, and will eventually reach the softening point of the glass material. The system setup is shown in Figure 10.6. The CO_2 laser, with a maximum output power of 25 W, was purchased from Synrad Inc. Precise control of the CO_2 laser power density (pulseduration and the pulse power) is achieved by a computer controlled D/A circuit and the laser control system. A computer controlled precision stage platform is also used to position the sensor head assembly with respect to the focused CO_2 laser beam.

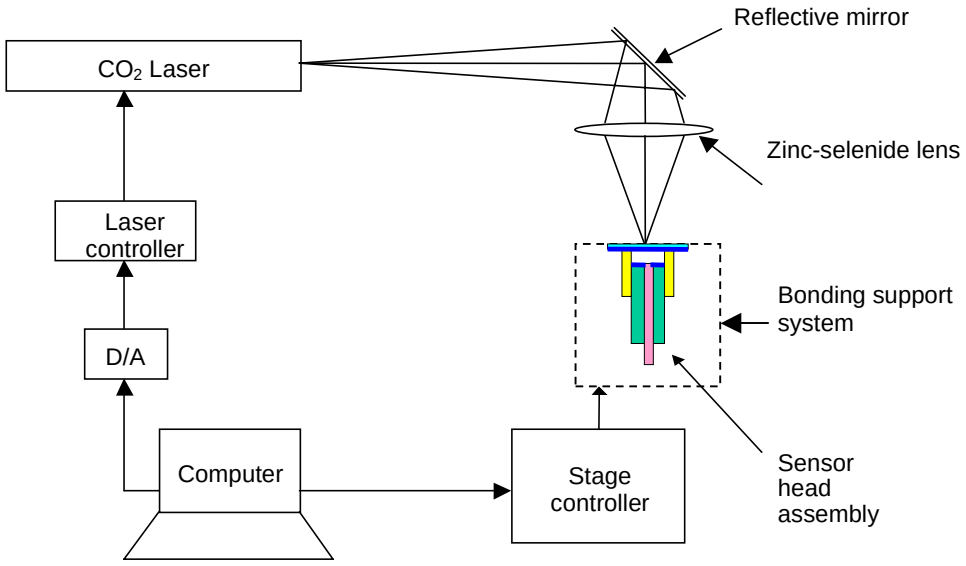

Figure 10.6. Direct thermal bonding diaphragm-based acoustic sensor fabrication system.

10.3.3 Intermediate layer thermal bonding

Previous experience with epoxy-based sensor and solder-based sensor fabrication suggested that a lower softening point material could be used between the two fused silica materials to achieve solid bonding. Borosilicate glass and soda lime glass have much lower softening points than the fused silica glass (1585°C), but higher than the operating temperature of all of the epoxies and most of the solders.

Based on this concept, an acoustic sensor fabrication system was designed using the intermediate layer method. The system configuration is shown in Figure 10.7. A furnace was used as the heating source. The sensor assembly, with the intermediate layer materials applied to the bonding region, was precisely positioned inside the furnace to allow uniform heating. A thermocouple was placed close to the sensor assembly so that the temperature could be precisely controlled and monitored during the sensor fabrication. The ferrule, fiber and the tube were bonded together by applying borosilicate powder. The bonding between the tube and the diaphragm was then achieved by using a special thin borosilicate fiber ring. The diaphragm was held before bonding by a vacuum tool. The holder for the ferrule and tube was made of fused silica glass, which has the same thermal expansion as the sensor components. After the sensor was bonded, it was necessary to anneal it for few hours to release the residual stress.

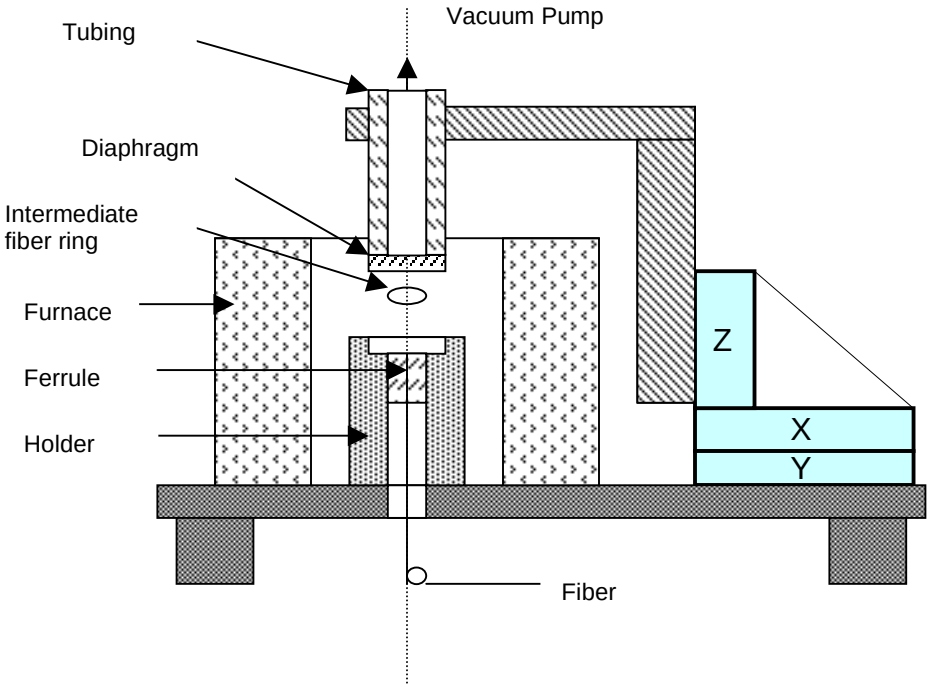

Figure 10.7. Acoustic sensor fabrication system using intermediate layer bonding method.

10.4 Acoustic Testing System

To evaluate the performance of the fabricated acoustic sensors, an acoustic test system was constructed (Figure 10.9). A WDU transducer was used to generate the ultrasonic signal by input from the pulse signal from a C-101-HV-2014 pulser. Also a WDU piezoelectric sensor was used as the standard to calibrate the fiber optic sensor. A 1221A preamplifier was used to amplify the detected acoustic signal from the WDU sensor. The WDU piezoelectric sensor and the fiber optic sensor were placed in a water tank to detect the acoustic signal from the WDU transducer. Amplified signals from both sensors are sent to the two channels of a Lecroy 505 digital storage oscilloscope so that by comparing these two outputs the fiber optic acoustic sensor could be calibrated. Figure 10.8 shows the experimental setup used for acoustic sensor testing.

10.5 Experimental Results

Using the testing system described above, the basic characteristics of the fiber optic acoustic sensors were evaluated. Data from a fiber optic acoustic sensor with a 1mm-diameter, 100μm-thick diaphragm is shown here. Driven by the pulse signal from C-101-HV-2014 pulser, the acoustic waves were generated and transferred to the sensors through water with fundamental frequency of f=130kHz. Figure 10.11 illustrates a series of detected signals from the fiber optic sensor and the WDU sensor. From the enlarged signal and FFT results in the bottom half of Figure 10.11, it is clear that the fiber optic acoustic sensor tracked the acoustic signals very well.

To determine the pressure sensitivity of the acoustic sensor, static water pressure was applied to the sensor head and the singlemode white light system was used to detect the air gap changes of the acoustic sensor. The relationship between the static pressure and the air gap is shown in Figure 10.10; the sensitivity is around 0.008nm/psi, which is near the theoretical value. So if we select the thin diaphragm, according to the Eq. 10-5, we can achieve very high sensitivity using this kind of acoustic sensor. These tests demonstrated that the fiber optic acoustic sensor could respond to the acoustic signal with high sensitivity in laboratory. The field test results are discussed in Chapter 13.

Figure 10.8. Photograph of acoustic testing system.

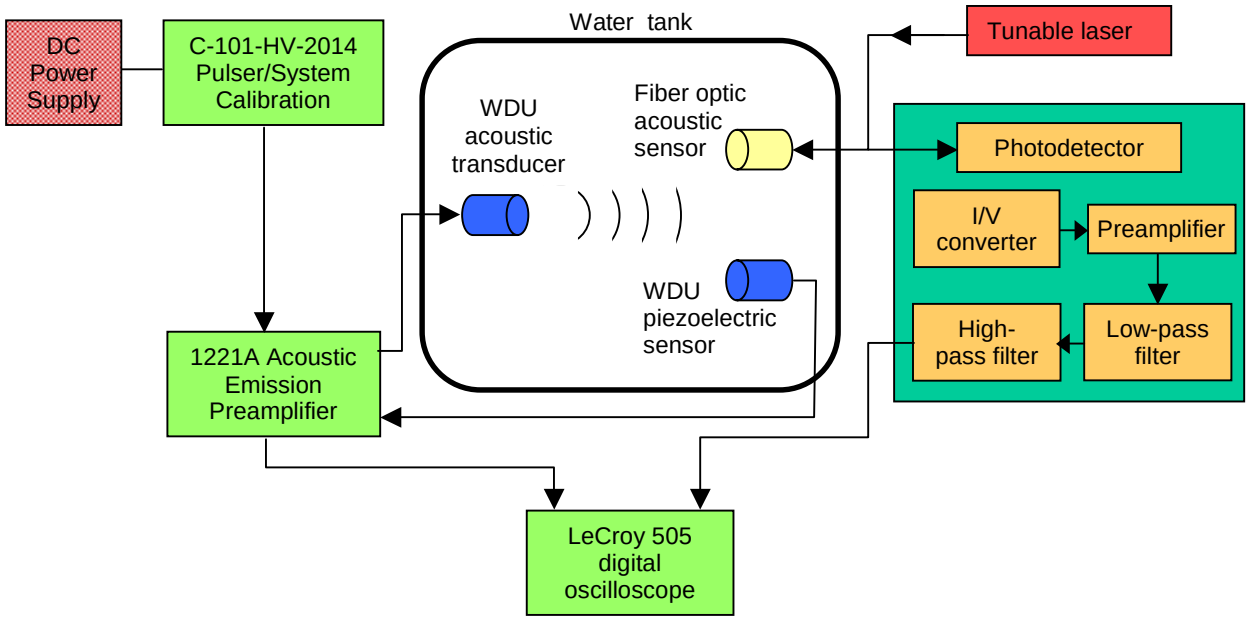

Figure 10.9. Acoustic sensor testing system configuration.

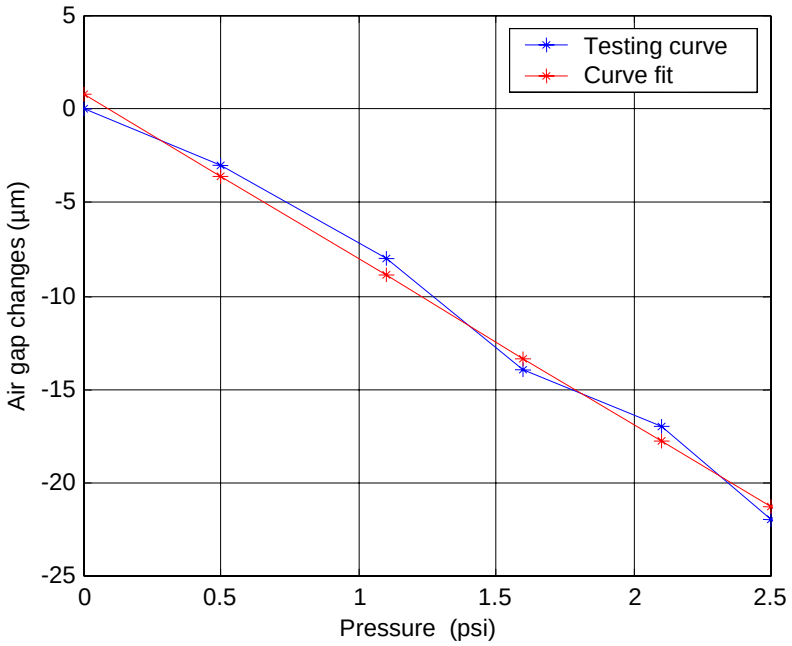

Figure 10.10. Pressure sensitivity of fiber optical acoustic sensor.

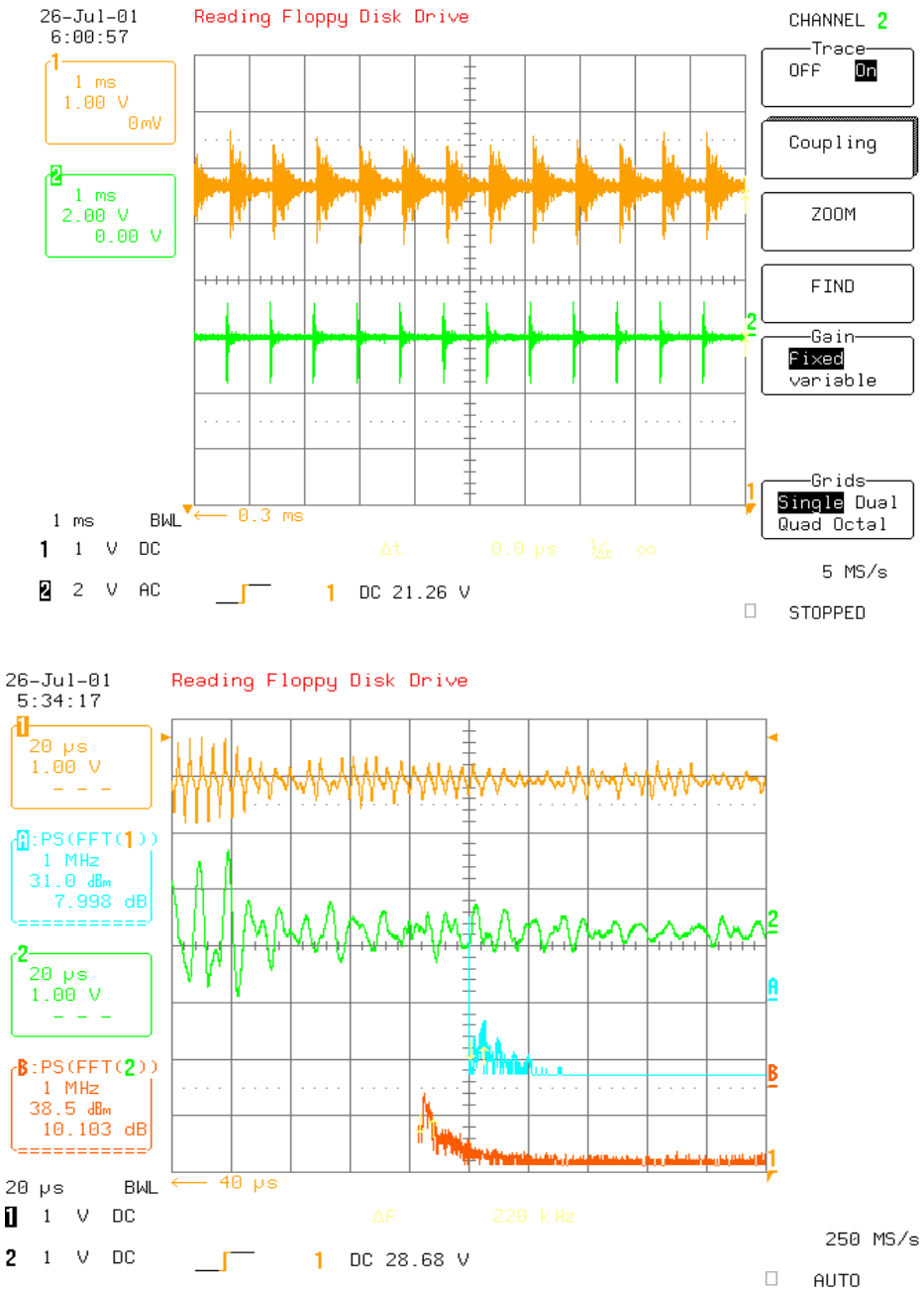

Figure 10.11. Comparison of acoustic signal from acoustic actuator (yellow) and acoustic sensor (green). The bottom graph is an enlargement of the acoustic signal from the LeCroy 505 oscilloscope.

11.0 Sensor Packaging Methods

The focus of this segment of the overall research project was aimed at development of suitable methods to protect the pressure and temperature sensor head from penetration by water and to improve the mechanical durability of the sensor head such that it would be able to survive the rigorous deployment process.

11.1 Packaging Requirements

While the method of protection selected had to be able to provide adequate protection from moisture penetration, at the same time, the protection could not be allowed to adversely affect the performance of the sensors. The requirements of the sensor packaging were:

1. Must provide adequate mechanical protection of the fiber sensor head and the connection between the sensor head and the transmission fiber
2. Must isolate the optical fiber sensor head from chemical corrosion and water penetration
3. For the pressure sensor, it must allow high pressure transduction fidelity
4. For the temperature sensor, it must isolate pressure while allowing high temperature transduction fidelity
5. The total finished size of the largest diameter of the protection package must be smaller than 1mm
6. The method selected must be simple and easy enough that it can be applied at the oil field site
7. For simplicity, it was desired that the method used to protect the splicing point of the optical fibers also be able to protect the sensor head rather than having two separate methods for each

A number of different methods were investigated to protect the sensor head, including laser ablation carbon coating with and without polyimide coatings, sputtering of gold thin films, additional outer glass tubings, and other methods of metallic coating. This chapter describes that effort, and the selected packaging method.

11.2 Determination of Minimum Bend Radius

In order to use optical fiber sensors for downhole oil exploration and recovery, it will be necessary for the fiber and sensor to bend around narrow passages within the deployment column. In some cases, the radius of curvature that the fiber optic cable and sensor assembly must traverse may be very small, possibly less than five or six inches. Therefore the minimum bend radius to which the fiber can be subjected without breaking or otherwise degrading is an important consideration in design of the overall system. In this segment of

the research, an experimental procedure and apparatus were developed to test the minimum bend radius that fibers treated under various conditions could survive.

In addition, it is anticipated that a protective coating may need to be applied to the fiber to prevent the penetration of water into the fiber. With this in mind, a theoretical analysis was undertaken to calculate the minimum bend radius as a function of coating thickness for several different potential coating materials in order to allow determination of the proper thickness more quickly than by trial and error.

11.2.1 Procedure for Minimum Bend Radius Testing

The apparatus shown in Figure 11.1 was constructed so that two parallel metal plates attached to a micrometer could be precisely positioned to hold a fiber at a fixed radius of curvature. On each of the two large, movable metal plates, two small ceramic plates were bonded to form a groove that was used to hold the fibers. These ceramic plates were bonded such that the distance between them was just slightly larger than the fiber diameter. In this way, the position of the fibers was fixed while the plates were brought closer together. The micrometer was calibrated to read zero when the two ceramic plates touched. The readings obtained from the micrometer represented the distance between the surfaces of the ceramic plates. The thickness of the ceramic plates was approximately the same thickness as the diameter of the optical fiber being tested. Therefore, the micrometer reading represented the separation distance between the inner fiber surfaces. The plates were moved at as close to a constant rate as possible during the first set of experiments. In the second set of experiments the plates were held at a constant separation distance and the time to failure was recorded.

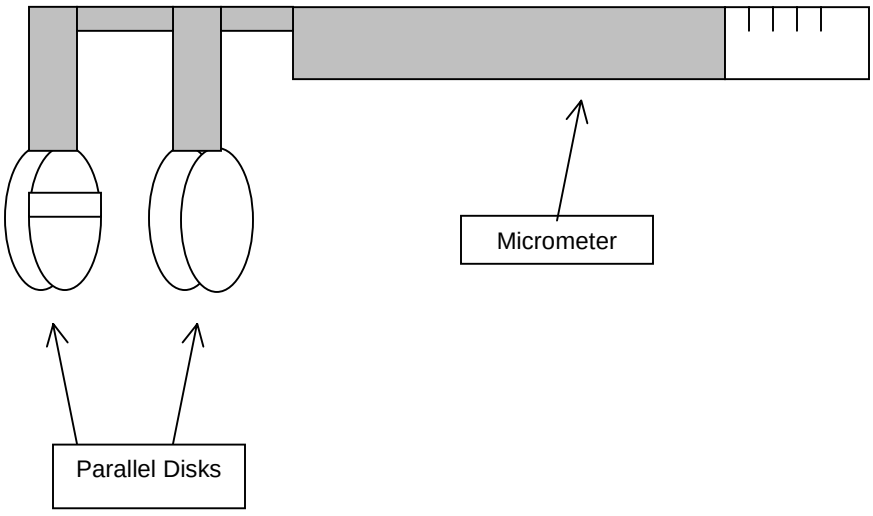

Figure 11.1. Apparatus used for minimum bend radius and time to failure testing.

Samples of singlemode fiber were cut into lengths approximately 25 cm long. The protective polyacrylate buffer (coating) was stripped from some of the fibers and left intact on others. The fibers were placed in a stainless steel tube. The tube was filled with water and the two ends of the tube were carefully sealed. The tubes were placed in an oven and heated to 200°C for specified lengths of time. The tubes were then cooled removed and opened. The water inside the tube was collected to ensure the tubes were properly sealed and the water was still present throughout the reaction time. In general, 15 fiber breaks were measured for each experimental condition. The data points shown in each of the figures that follow represent the average of the 15 measurements.

11.2.2 Minimum Bend Radius Results

Singlemode optical fiber with a cladding diameter of 125 microns was used as received for this experiment. In the first set of tests, the buffer was stripped with a razor blade. Testing of the minimum bend radius of these fibers showed that there was a large standard deviation. This was most likely due to the damage inflicted on the fiber by the razor blade. The procedure was changed to soaking the fiber in acetone to facilitate buffer removal. The acetone caused the buffer to swell and peel easily away from the fiber. The results for the minimum bend radius for the singlemode fiber showed that the fiber had a average minimum bend radius of 0.045" in with the buffer intact (as received) and 0.049" with the buffer removed by acetone.

The minimum bend diameter versus exposure time at 200°C is shown in Figure 11.2. The average minimum bend diameter for the fibers with the buffer on is approximately 0.08 in. and for the fibers with no buffer it is 0.22 in. The minimum bend diameter was the distance between the inner fiber surfaces when the fiber fractured. In both groups of fibers, the minimum bend diameter has no relation to the exposure time at 200°C. It appears that all the

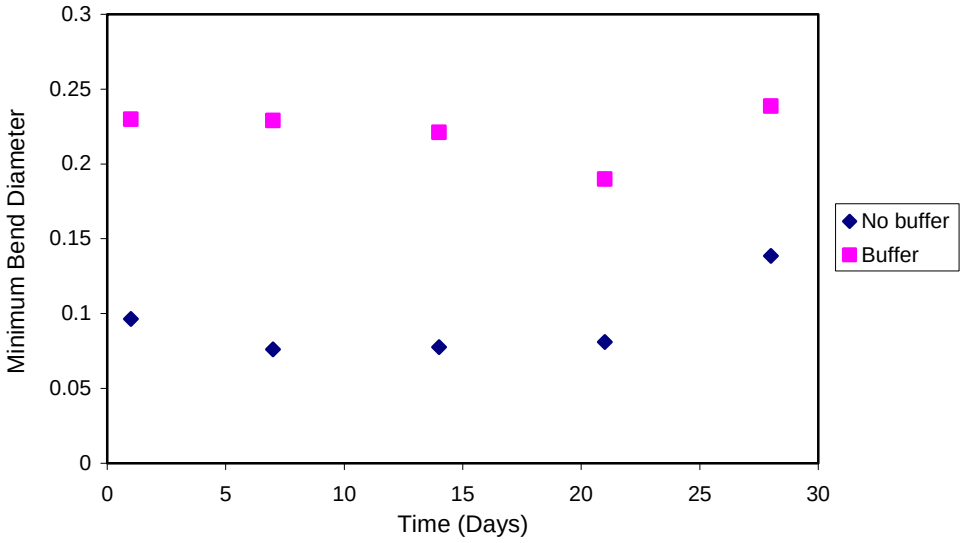

Figure 11.2. Minimum bend diameter versus exposure time at 200ºC.

degradation in the fiber occurs within the first day of exposure. After the first day of exposure, subsequent days of exposure do not affect the minimum bend diameter. It is not certain why the minimum bend diameter for the fibers with buffer shows a distinct difference from those exposed without the buffer. One likely explanation is that the buffer removal process damages the surface of the fibers. The failure of brittle ceramics is a statistical function of the probability of encountering a crack large enough produce failure at a given applied stress. The relation that governs brittle fracture in glass and ceramic materials is

$$\sigma_f = \frac{K_{IC}}{\sqrt{YC}}, \qquad \textbf{(11-1)}$$

where σ_f = the fracture stress, K_{IC} = fracture toughness of the material under mode I loading, Y = the crack geometry factor, and C = the crack size. As seen from this relationship, the stress required for fracture to occur in the glass fiber is a function of the size of the flaws that are present. Since glass materials (and ceramics in general) are much stronger in compression than tension, the fracture almost always originates on the tensile side of the fiber (when bent). Changing the flaw population distribution along the surface of the fiber changes the stress required to fracture the fiber and therefore will affect the minimum bend radius measured. Almost certainly, the fiber with the buffer removed undergoes much more damage than the fiber with the buffer in tact just from handling the fiber to cut and insert into the tubing and possibly from the tubing wall itself.

In order to investigate the effect of the rate of stress application on the failure bend diameter, an additional set of experiments were undertaken. The optical fibers were held at a fixed bend diameter and the time to failure measured. Figure 11.3 shows the time to failure for as-received polyacrylate-coated Corning SMF fiber versus bend diameter. The exponential relationship between the time to failure and the applied stress level indicates that the fiber is susceptible to stress corrosion cracking. This phenomenon, which is also referred to as fatigue in glasses, is a common occurrence. Normally, as described above, the fracture of the glass fiber occurs when the stress value reaches a critical limit dictated by the flaw population distribution. The crack propagation occurs at a velocity of approximately the speed of sound and appears for all practical purposes to occur instantaneously. If the stress is below the critical fracture stress, in certain circumstances the crack can grow at a sub-critical velocity. This is usually associated with the presence of water in the testing environment. The exact relationship between the sub-critical crack velocity and the applied stress is not known, and in some cases is assumed to be a power function. In other cases it is assumed to be exponential in nature. In this report we will assume that the relationship follows an exponential relationship. The details of how the water present in the environment assists the propagation of the crack are not completely understood. It is generally assumed that the water reacts at the crack tip in the presence of stress to break the Si-O bond. As the Si-O bonds are successively broken the crack elongates. The rate of the reaction of the water with the Si-O depends upon the value of the stress. At higher stress values, the crack propagates more quickly an therefore the time to failure is shorter. Conversely, at lower stress values the crack propagates more slowly and time required to reach the critical crack size for the given stress level is longer.

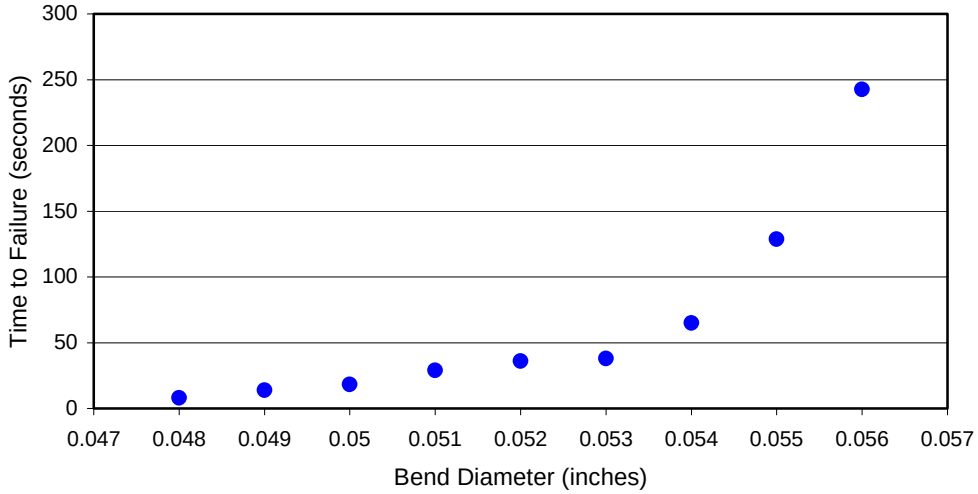

Figure 11.3. Time to failure versus bend diameter for Corning SMF.

Figure 11.4 shows the data from Figure 11.3 plotted with the y axis in log scale. The data appears linear when plotted in this semi-log plot. Since the diameter of the fiber is known and the radius to which the fiber is bent is known, the stress acting on the tensile surface of the fiber can be calculated. This has been done for each of the bend diameters in Figure 11.4 and the data re-plotted as a function of reciprocal stress in Figure 11.5. As shown in this figure, the log of the time to failure is directly proportional to the reciprocal stress applied to the fiber as is predicted by the theory. In the phenomenon of stress corrosion cracking of glass materials, water is known to play a key role in the process. It is believed that the water

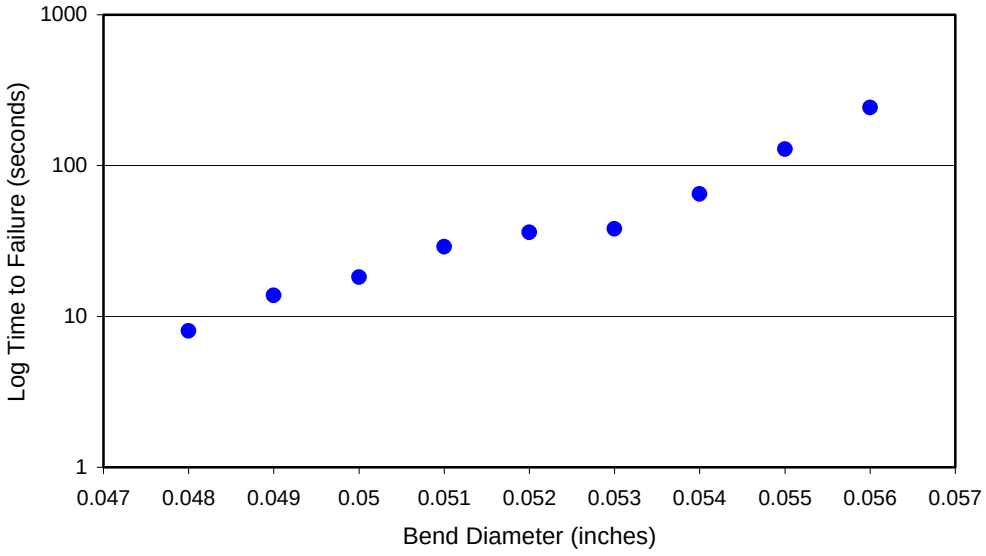

Figure 11.4. Time to failure versus bend diameter.

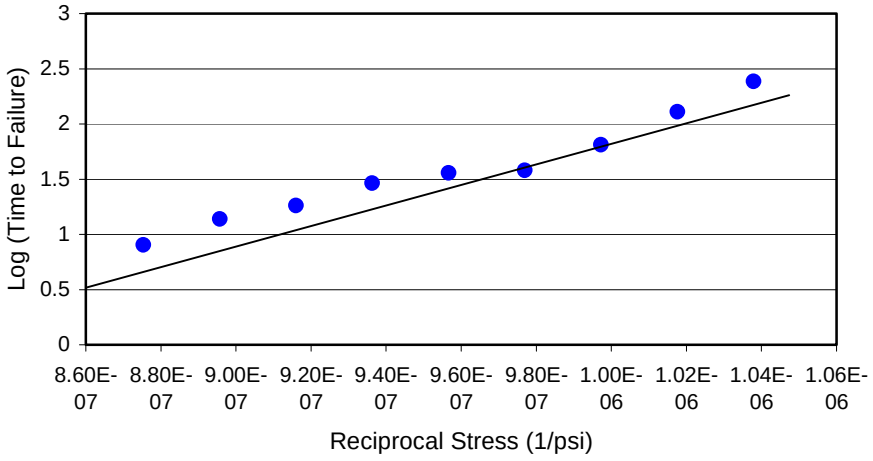

Figure 11.5. Time to failure versus reciprocal stress for Corning SMF.

lowers the energy required for crack propagation by breaking the Si-O (silicon-oxygen) bond as described above. This process is not completely understood. It might well be that water diffuses into the glass material at the crack tip due to the high values of stress in the crack tip vicinity. It is possible that it is this diffusion of water into the crack tip vicinity that lowers the overall fracture toughness of the material. In this model, fracture would occur when the fracture toughness reaches a low enough value.

In order to further investigate this phenomenon, as-received fibers were tested along with fibers soaked in water at room temperature for 30 minutes. These data are shown in Figure 11.6.

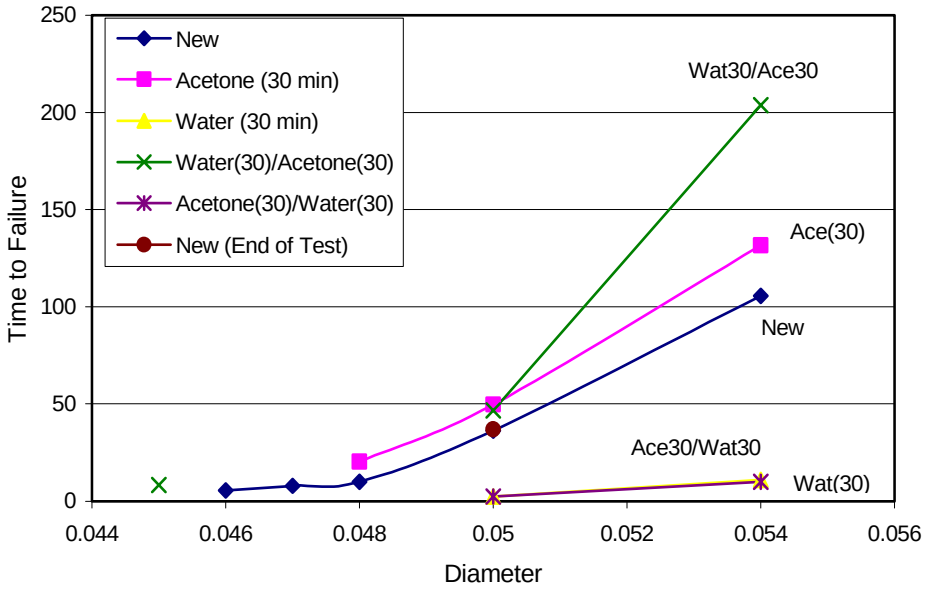

Figure 11.6. Average time to failure for optical fiber versus bend diameter.

After only 30 minutes of soaking, the fiber shows a significant reduction in the time to failure for the single mode fiber (SMF) with the buffer intact. Samples of the new singlemode fiber were also soaked in acetone for 30 minutes and an increase in the time to failure was observed. In order to investigate whether these processes were reversible, the SMF fibers were soaked in water for 30 minutes then in acetone for 30 minutes. The acetone soak completely negates the effect of the water soaking. Conversely, fibers soaked in acetone for 30 minutes then in water for 30 minutes show the water soaking completely negates the affect of the acetone soaking. All of these data are shown in Figure 11.6. These data clearly show that water has a detrimental effect on the time to failure of SMF fiber. The new unsoaked fiber that was tested had most likely absorbed water from the atmosphere. Removal of this water during the acetone soak is responsible for the increase in the time to failure of the fibers as compared to the "as-received" condition. The value for the fibers soaked in water for 30 minutes and then in acetone for thirty minutes held at a bend diameter of 0.054 inches is unusually high. It is suspected that the reason for this is solely due to measurement scatter. In that group of 15 fibers that were tested, one fiber exhibited a much longer time to failure than the other fibers in that group. If the reading for that fiber is eliminated, the data for that set would lie almost exactly on top of the data for the fibers soaked in acetone for 30 minutes (no water treatment).

In another set of experiments, samples of the SMF fiber were soaked in water for 24 hrs, then removed and allowed to stand in air for various periods of time before testing. The results are shown in Figure 11.7. After soaking in water for 24 hrs, the time to failure was very short (less than 1 second). As time progressed, however, the time to failure steadily increased until it reached the same level as that of the new fibers. This is most likely due to the loss of water from the fiber to the air. This result clearly shows that the process of degradation of the fiber due to exposure by water is completely reversible by allowing the fiber to lose the water by standing for a period of time in air. No permanent effects are observed due to the water treatment.

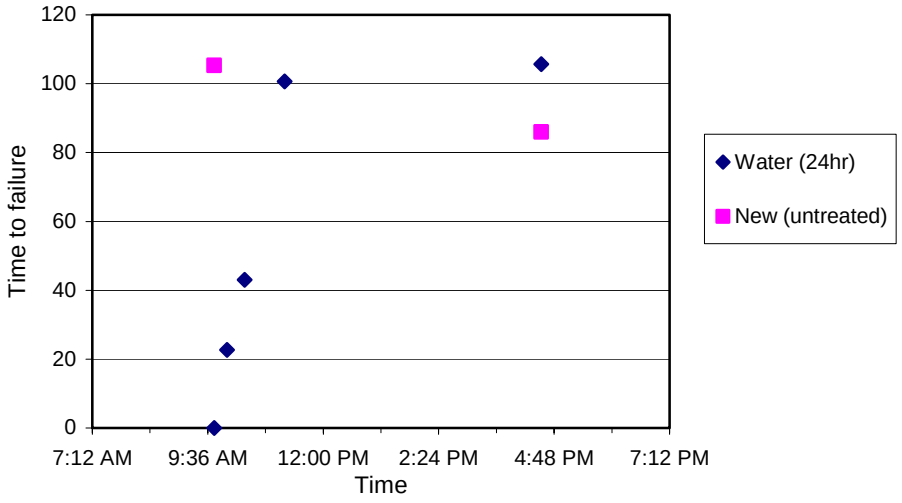

Figure 11.7. Time to failure versus time after exposure.

A theoretical treatment was undertaken to calculate the minimum bend radius as a function of coating thickness for several different materials. The data from these calculations is shown in Figure 11.8. The calculation is based on a 125 micron outer diameter optical fiber coated with various thickness and types of materials. The minimum bend radius was determined as that point at which 0.002% plastic strain would occur in the metal coating. From the curves, it can be seen that an upper limit of about 10 microns or so is about the maximum thickness the coating should be (depending of course upon the choice of material used).

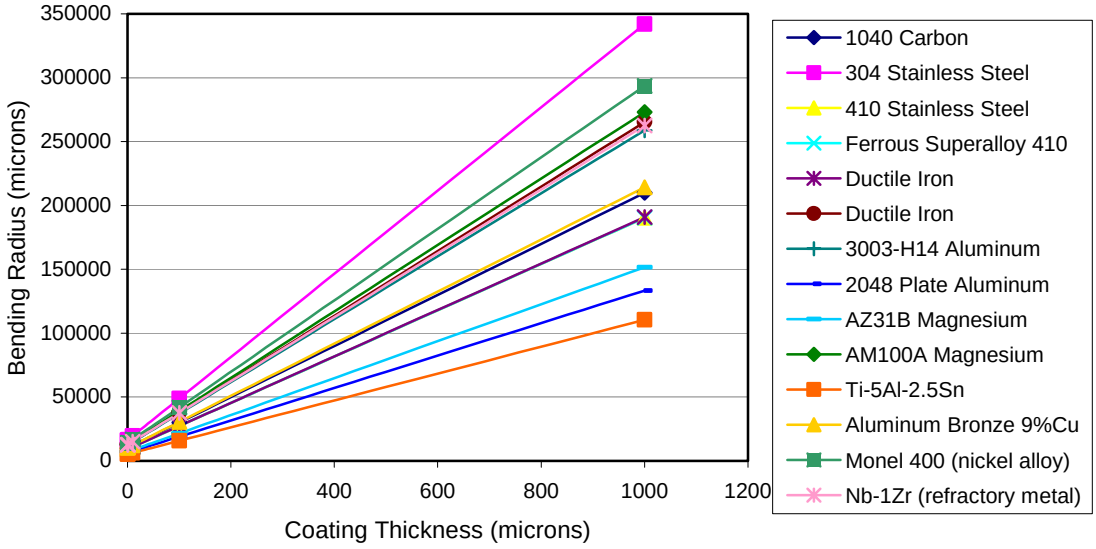

Figure 11.8. Calculated minimum bend radius versus coating thickness for various coating materials.

11.3 Water Effects at Elevated Temperature and Pressure

The goal of this segment of the research program was to evaluate the performance of the optical fiber that will be used to connect the sensor head to the outside world (above ground). Data from Chevron has indicated that penetration of water into optical fibers in the down-hole environment has proved to be detrimental to the life of the fiber. In order to protect the fiber from water, a series of experiments was performed to develop a suitable coating to protect the optical fiber. In order to test the effects of water at elevated temperature and pressure, a special apparatus was constructed as described in the experimental procedure section below. The fibers tested in these experiments were subjected to much higher temperatures than would normally be seen in the downhole environment (approximately 100% higher, 300°C test temperature as compared to 150°C expected maximum operating temperature). The effect of the increased testing temperature on the rate of diffusion of water into the silica fiber is expected to be exponential as described in the results and discussion section. Since the rate of penetration of water into the unprotected fibers was significant, several methods of protecting the fiber were tested in the experimental setup as well.

11.3.1 Experimental Procedure for Fiber Testing in Water at Elevated Temperature and Pressure

Two methods for protection of the optical fiber were selected for testing initially. These employed stainless steel needle tubing and carbon coating. In the case of stainless steel needle tubing, tubing approximately 508 micron OD and 292 micron ID was used. The polyacrylate-coated fiber was inserted into the stainless steel tubing which was filled with water. This fiber and tubing were inserted into another stainless steel tube approximately one quarter inch in diameter such that the needle tubing extended beyond the end of the tubing fittings. The fittings had been predrilled with a small hole just slightly larger than the diameter of the needle tubing. The needle tubing was sealed to the fitting using Miller-Stephenson 907 epoxy. This assembly was in turn inserted into a tube furnace heated at 300°C, such that the ends of the stainless steel tube, which were epoxied, stuck out of the ends of the furnace. The ends of the optical fibers were connected to a white light source and to an optical spectral analyzer respectively. Several other channels were prepared in the same way. In the second channel, a Spectran carbon/polyimide coated fiber was sealed in water in the stainless steel tubing. In the third channel, an as-received polyacrylate-coated multimode fiber without any additional protection was sealed. The fourth channel was used as a reference channel. A fiber was connected from the white light source to the optical spectrum analyzer directly without passing through the furnace. This was used as a reference to compensate for any changes in optical power from the white light source that might occur. All of the fibers were connected to the same white light source through a series of couplers such that once the connections were made they were not disturbed throughout the entire testing process. The pressure developed in the tubing can be determined from the steam tables. At 300°C the pressure inside the stainless steel tubing is 1440 psi.

11.3.2 Experimental Results – Optical Fiber Performance in Water at Elevated Temperature and Pressure

Figure 11.9 shows the absorption in decibels (dB) versus time in hours for the fibers immersed in water and heated to 300°C. As can be seen in this figure, the as-received fiber (without any protection) labeled "water" shows a relatively high absorption rate of water. In comparison, the carbon/polyimide coated fiber, labeled Spect 2, shows very low water absorption tendency. It must be pointed out that 300°C represents a much higher temperature than the fiber would normally experience in the downhole environment. Normally the fiber will experience temperatures less than 200°C. The penetration rate of water into the fiber is assumed to be diffusion controlled. Water at the surface of the fiber diffuses into the fiber due to the concentration difference between the surface and the interior. If the process is diffusion controlled, the flux of water into the fiber will be proportional to the diffusivity of water in the silica glass multiplied by the chemical potential gradient. If we let J= the flux of water, D= the diffusivity and $\nabla\mu$= the chemical potential gradient then

$$J = D\nabla\mu \,. \qquad \textbf{(11-2)}$$

The chemical potential is defined as the partial molar free energy

$$\mu = \frac{\partial G}{\partial n_i}, \tag{11-3}$$

where G= free energy of the system, and n_i = number of moles of component i. For diffusion only in one dimension, for example the x direction, assuming that the chemical potential gradient can be approximated by the concentration gradient of the diffusing species, the equation simplifies to

$$\mu = D\frac{\partial C_i}{\partial x}, \tag{11-4}$$

which is the familiar form of Fick's first law for diffusion.

Since diffusion is a thermally activated process, the diffusivity can be represented as

$$D = D_0 e^{-Q/RT}, \tag{11-5}$$

where Q= activation energy for the rate controlling process, R= the ideal gas constant, D_o= the pre-exponential term and T= the temperature. As seen from this relation, the diffusivity, and likewise the flux, will be exponentially dependent upon the temperature. Therefore, the penetration rate of water into the fiber at 300°C will be exponentially higher than the rate at 200°C. So the testing temperature of 300°C represents a significant accelerating factor in the testing.

The fiber within the needle tubing labeled as "W/T" (water with tubing) has shown no detectable change in the absorption due to water. This is a remarkably good result and shows the stainless steel needle tubing can provide excellent protection against water penetration.

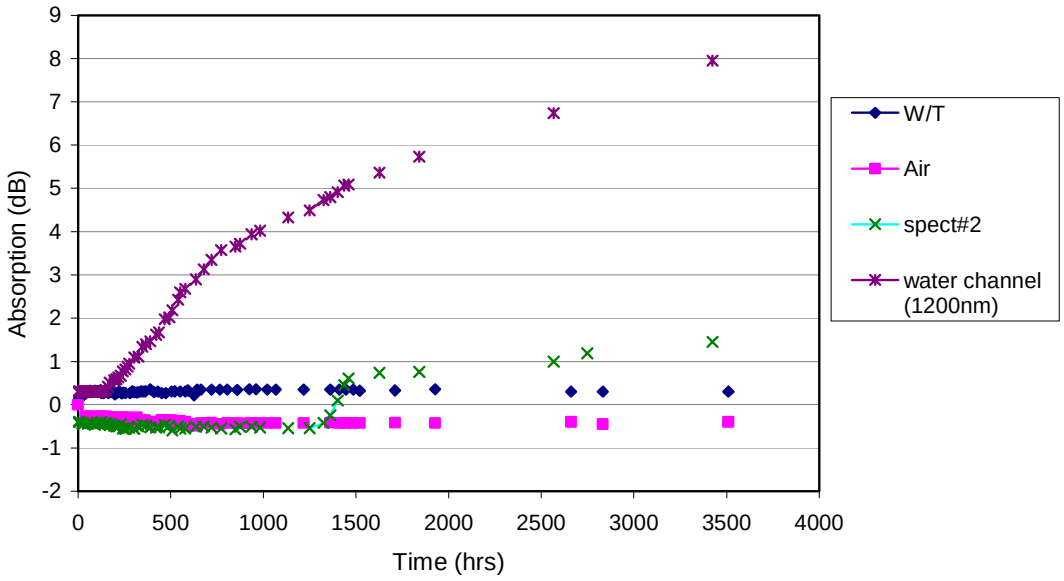

Figure 11.9. OH absorption versus time for fibers immersed in water at 200°C.

11.4 Carbon-Coated Fiber Development

Due to the outstanding results for protection against water penetration obtained for carbon coated and stainless steel needle tubing protected fibers, both metal coatings and carbon coatings were investigated to protect the sensor head. In this section, the results of the carbon coating development work will be presented. The coating method employed to deposit amorphous carbon onto the sensor head was laser ablation deposition. In this technique, a krypton-fluoride laser is directed through a series of mirrors and windows at a rotating carbon target in a vacuum chamber, which is pumped down to 10^{-6} torr. After stabilizing at this vacuum for a short period of time, oxygen is introduced into the chamber. The vacuum is stabilized at 10^{-4} torr. At this point the shutter to the laser beam is opened and the laser beam admitted to the target. A computer-controlled pulse firing sequence is initiated. The carbon is ablated from the surface with each pulse of the laser and deposits on the sample. The pulse count for samples coated to date has been 4000. After coating, the laser beam shutter is closed and the chamber is repressurized. The chamber cover is then opened and the samples removed.

Figure 11.10 shows an SEM micrograph of the fracture surface of a sensor coated using the laser ablation technique. As shown in this figure, the coating appears to be very uniformly distributed around the surface of the fused silica glass. It should be noted that the sample in this SEM micrograph is rotated about 10 degrees toward the viewer. The surface of the coating appears smooth and very uniform. The carbon coating thickness is approximately 1 micron. The fiber shown here is from the reflecting end of a sensor.

The entire sensor assembly was examined by optical microscopy as well. In transmitted light, the entire sensor system seemed uniformly coated. No pits, bubbles or obvious imperfections were observed. A Spectran carbon/polyimide coated fiber was used as the lead-in fiber in this sensor. The fiber was carbon-coated all over, except for the lead-in end, where the carbon coating was removed by soaking in hot sulfuric acid. After sensor bonding (fiber is bonded inside a fused silica tube), a short section of the fiber, which had been stripped, remained outside the tube. The laser ablation coating process not only coated the sensor head uniformly, but also coated the portion of the fiber that had been stripped during the sensor fabrication.

Experiments were also conducted to develop a method to overcoat the carbon-coated sensors with a polyimide coating. Several sensors were successfully coated with the polyimide material and cured.

11.5 Gold-Coated Fiber

This section describes the development of metallic coatings to protect the sensor head from penetration by water. Gold coatings were applied only to the sensor head and is believed to be approximately a few hundred nanometers thick based on previous experience with using the sputter coater to coat SEM samples. Figure 11.11 shows the results of the stability testing for a gold-coated sensor held at 205°C for two weeks in air. The standard deviation was calculated to be 0.0014.

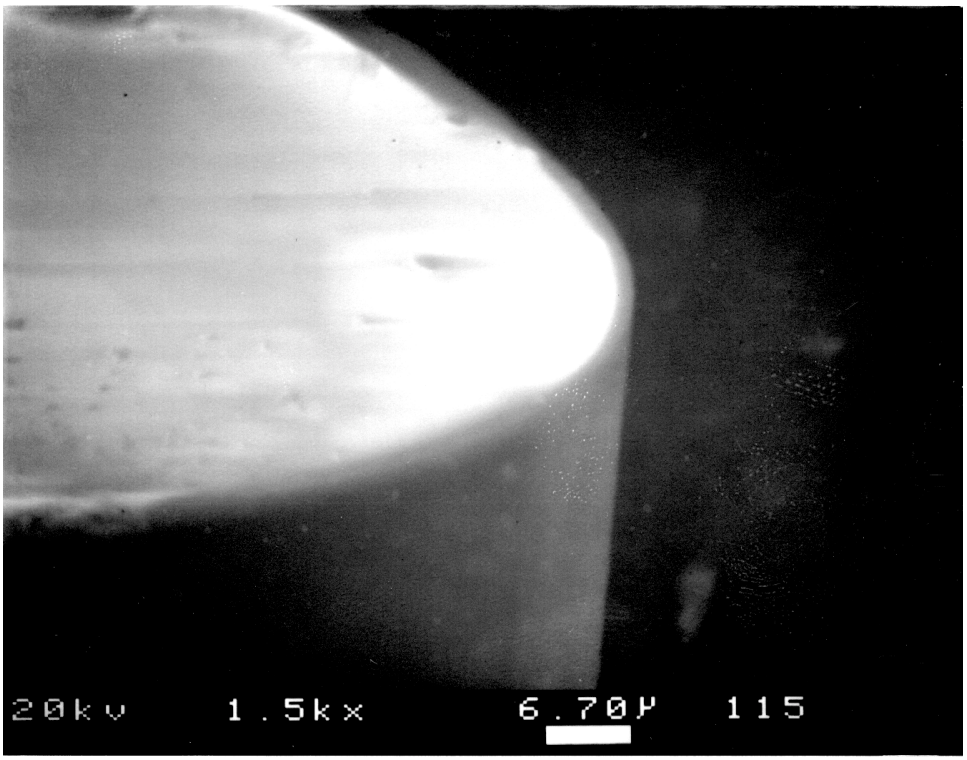

Figure 11.10. SEM micrograph of the fracture surface of an optical fiber coated with carbon by laser ablation

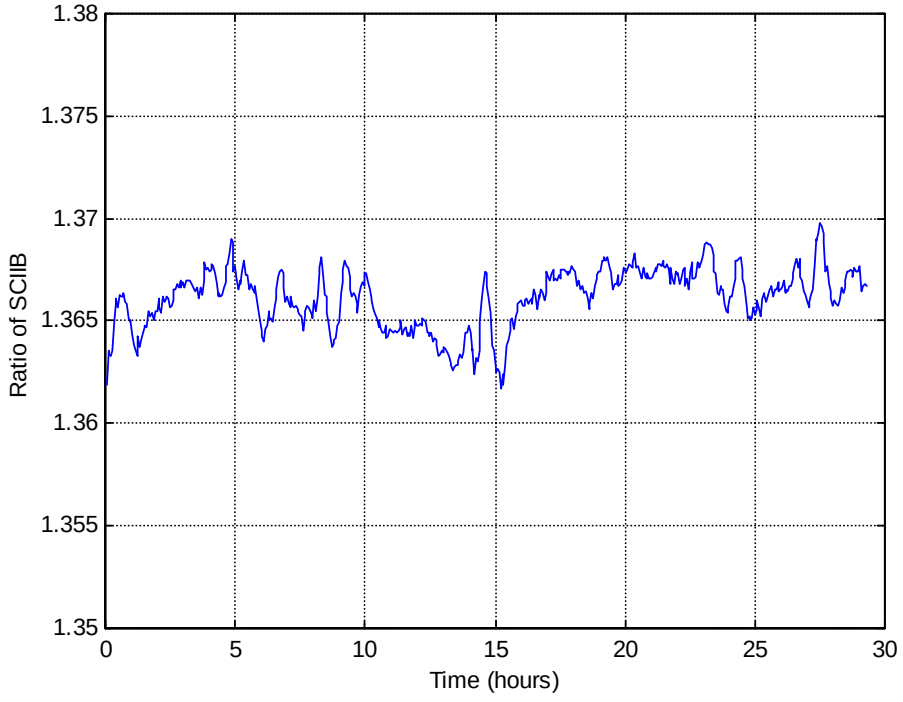

Figure 11.11. Results of stability testing of signal processing system – gold coated sensor held at 205°C.

In the downhole oil environment, the sensor will be subjected to simultaneous application of elevated temperature and pressure in an environment containing water. In order to evaluate the effects of such a combination of variables on the long-term stability of the sensor, a series of experiments was performed. In the first set of experiments an uncoated sensor was placed in the APP high-pressure calibration system. The system was heated to 200°C. The SCIIB output pressure as a function of the applied pressure was measured once per day. The results are shown in Figure 11.12 and Figure 11.13. As can be seen in this figure, the curve shifts as a function of exposure to the high temperature, high-pressure environment. The pressurizing fluid that was used in these experiments was water. It is believed that the shift in the curves represents the change in the physical dimensions of the sensor due to penetration of water molecules into the glass structure. The magnitude of the change from one day to the next day becomes smaller as time progresses. It is not certain whether the sensor is saturated with water, preventing further significant changes in sensor reading or whether the shift will progress.

The same experiment was repeated with a sensor coated with gold. The data obtained in this fashion is shown in Figure 11.14 and Figure 11.15. The gold-coated sensor exhibited a shift in the curve similar to the uncoated sensor, but larger in magnitude. The gold coating applied to the sensor did not adhere well. This is a common problem in the mirror industry. In order to allow the gold to stick to the substrate more strongly, a chromium layer was first applied to the glass before the gold is applied. In the sputtering system used in these experiments, the option to put down a layer of chromium before the gold was applied was not available. The new sputtering system acquired by CPT during this program does permit the deposition of chromium first followed by gold deposition.

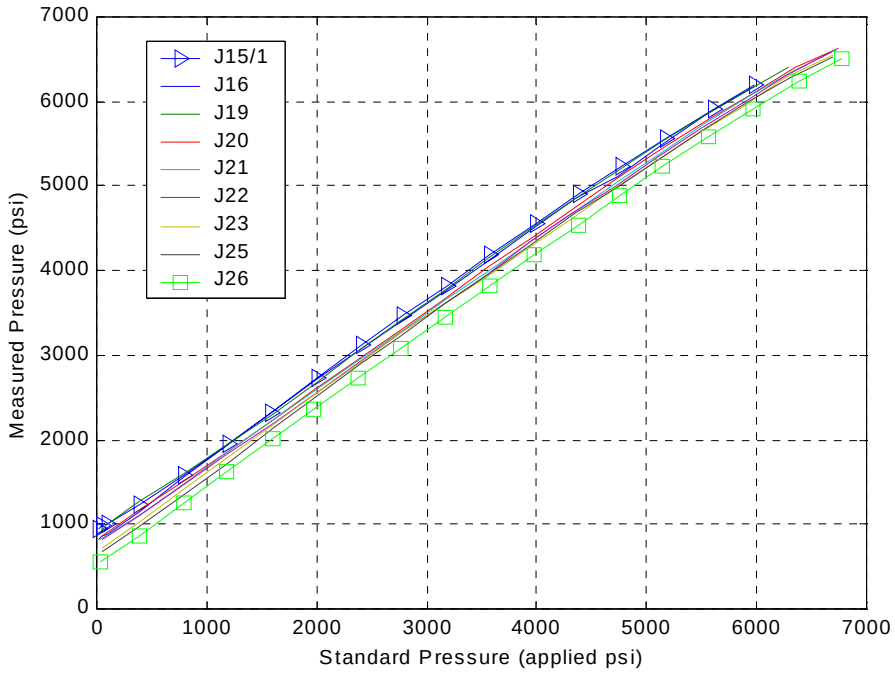

Figure 11.12. Measured pressure versus applied pressure as a function of exposure time for an uncoated sensor.

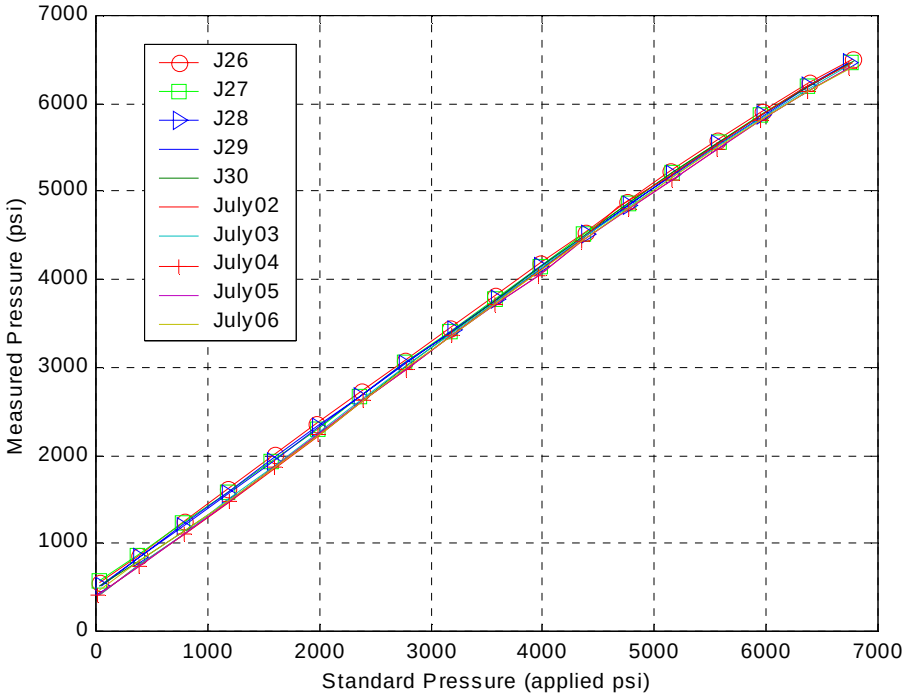

Figure 11.13. Measured pressure versus applied pressure as a function of exposure time for an uncoated sensor (continued).

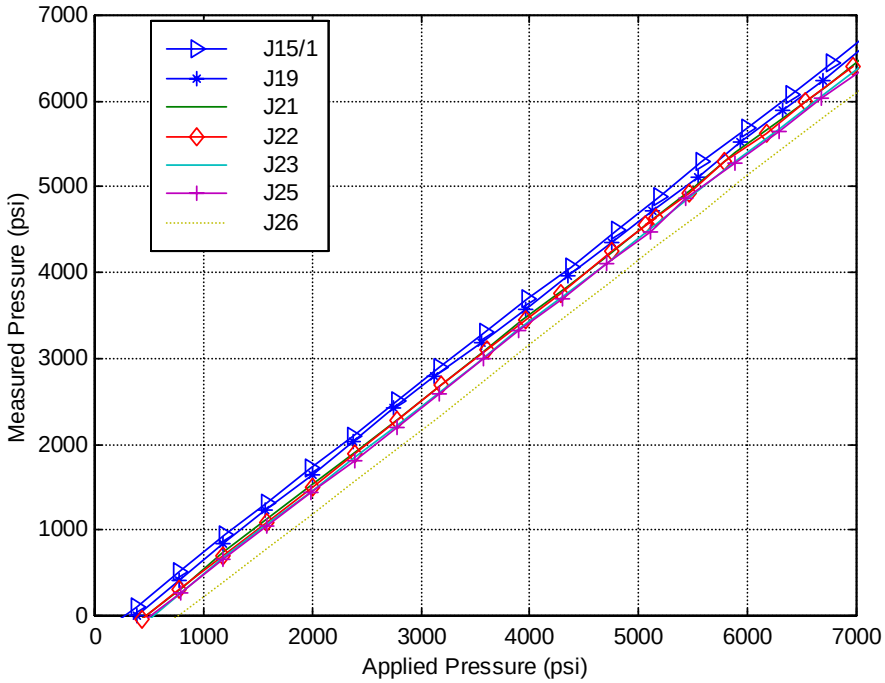

Figure 11.14. Measured pressure versus applied pressure as a function of exposure time for an gold coated sensor.

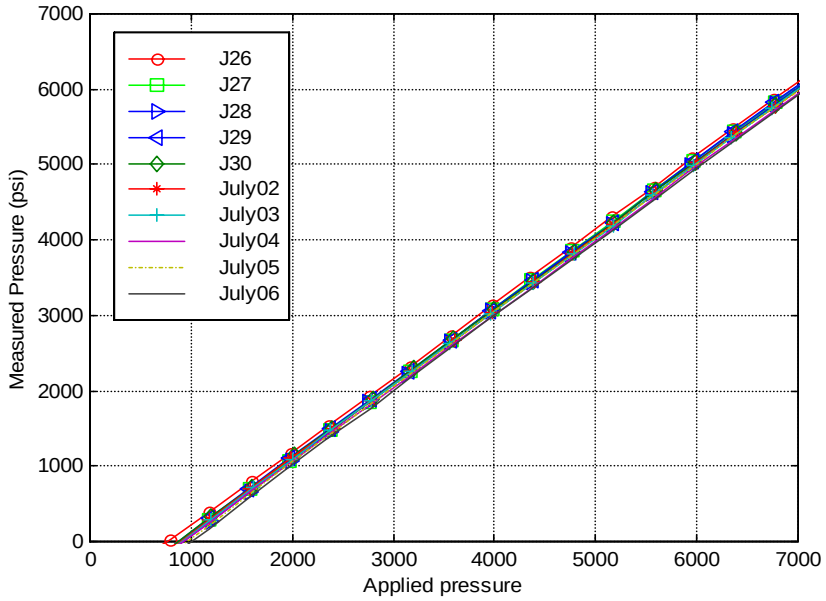

Figure 11.15. Measured pressure versus applied pressure as a function of exposure time for a gold-coated sensor.

Figure 11.16 shows the change in sensor output as a function of exposure time for both the gold-coated and uncoated sensor. The curves shown in this figure represent the variation between the pressure reading (in psi) as measured by the SCIIB system, at 3000 psi applied pressure, on the first day compared to the day being measured. For example, the pressure reading on day 5 from the SCIIB system at 3000 psi applied pressure minus the pressure reading from the SCIIB system on day 1 at 3000 psi applied pressure would become the value plotted for day 5. It can be seen from this figure that the readings for both the gold coated and the uncoated sensors show a positive trend. The magnitude of the slope for a gold-coated sensor is approximately twice the magnitude of the slope for the uncoated sensor. It is suspected that the increase in slope for both the gold-coated and uncoated sensor is due to penetration of water into the sensor.

Figure 11.17 through Figure 11.20 show a second set of data for the variation in calibration for a gold coated and an uncoated sensor. The data appear to be very consistent with the data shown in Figure 11.12 through Figure 11.15. The data for the pressure calibration variation versus number of days of exposure is shown in Figure 11.21 and shows a similar relation to that shown in Figure 11.16 for the previous set of data.

Figure 11.22 shows the variation in the SCIIB output ratio versus applied pressure for different states of polarization of the fiber pigtail. In this set of experiments, the fiber was rotated to various degrees while the readings were being acquired. The average system polarization error was calculated to be 1.12%. Figure 11.23 shows the variation in SCIIB output versus the applied pressure for different splicing losses. Initially, the system was spliced with a fusion splicer and the readings taken. The splice was then broken and respliced and the readings taken again. In each case the loss due to splicing as measured by the fusion splicer is noted on each curve on the graph.

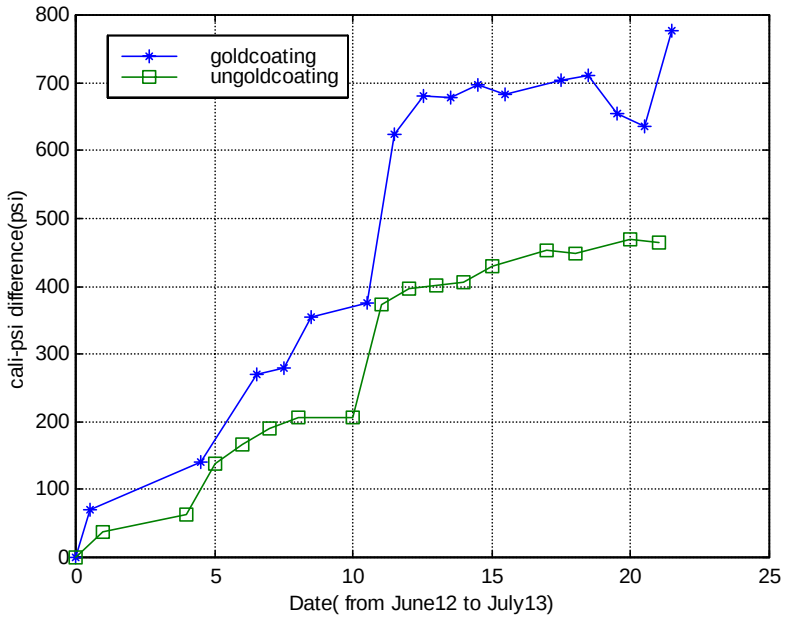

Figure 11.16. Pressure calibration difference between first and following days versus date for a gold coated and an uncoated sensor.

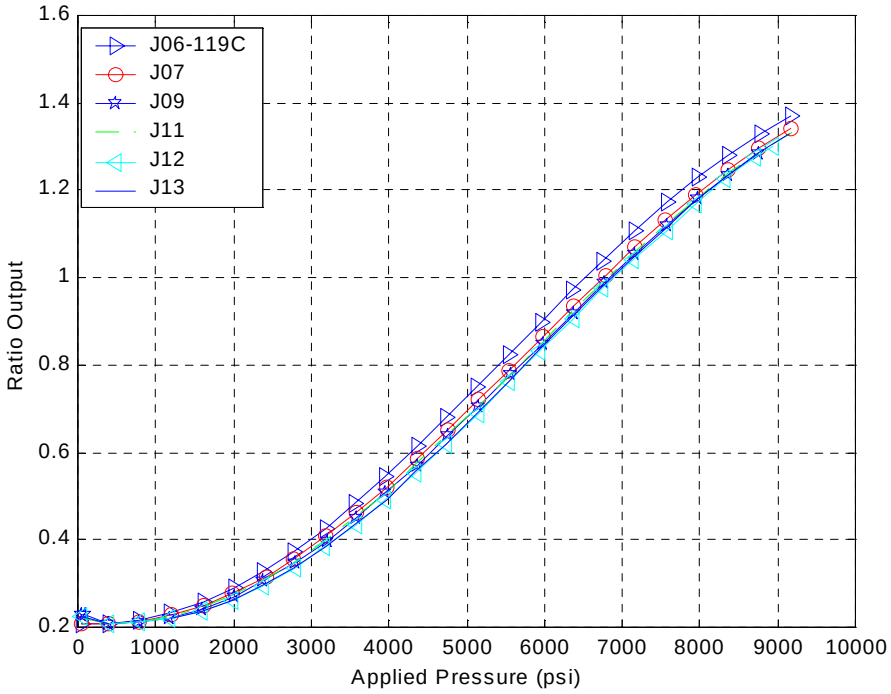

Figure 11.17. Measured pressure versus applied pressure as a function of exposure time for an uncoated sensor

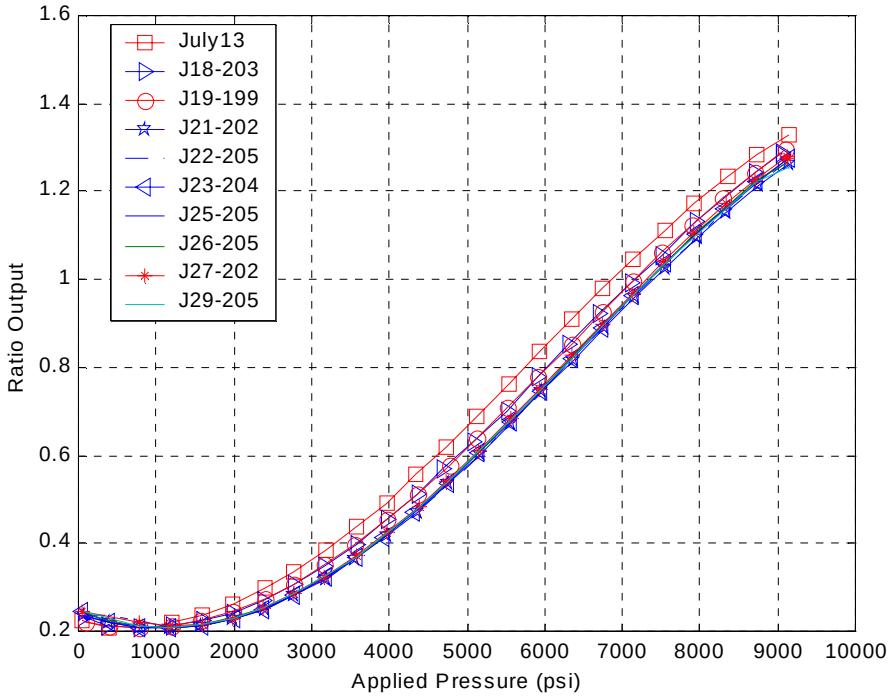

Figure 11.18. Measured pressure versus applied pressure as a function of exposure time for an uncoated sensor (continued).

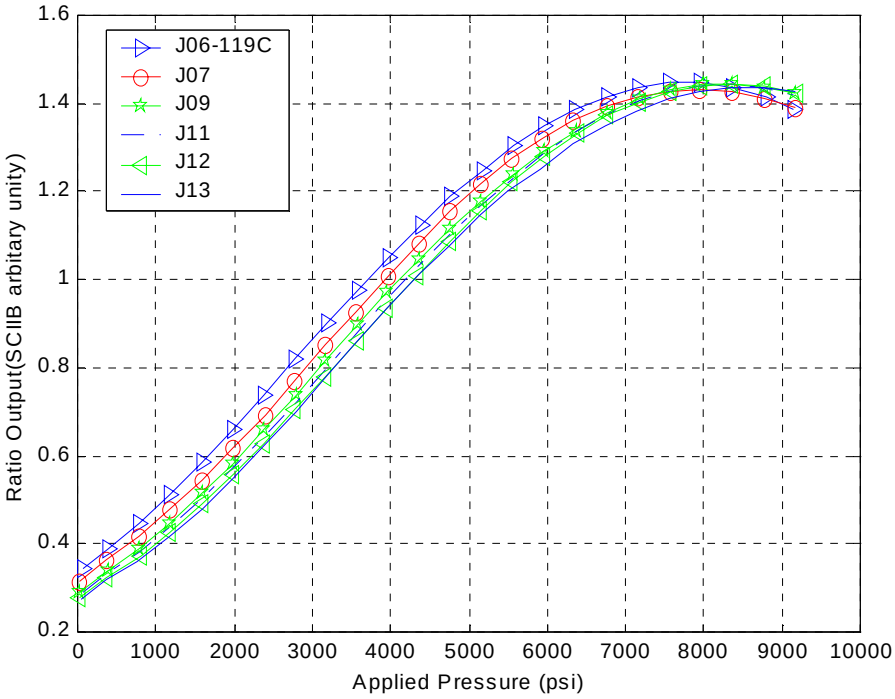

Figure 11.19. Measured pressure versus applied pressure as a function of exposure time for an uncoated sensor.

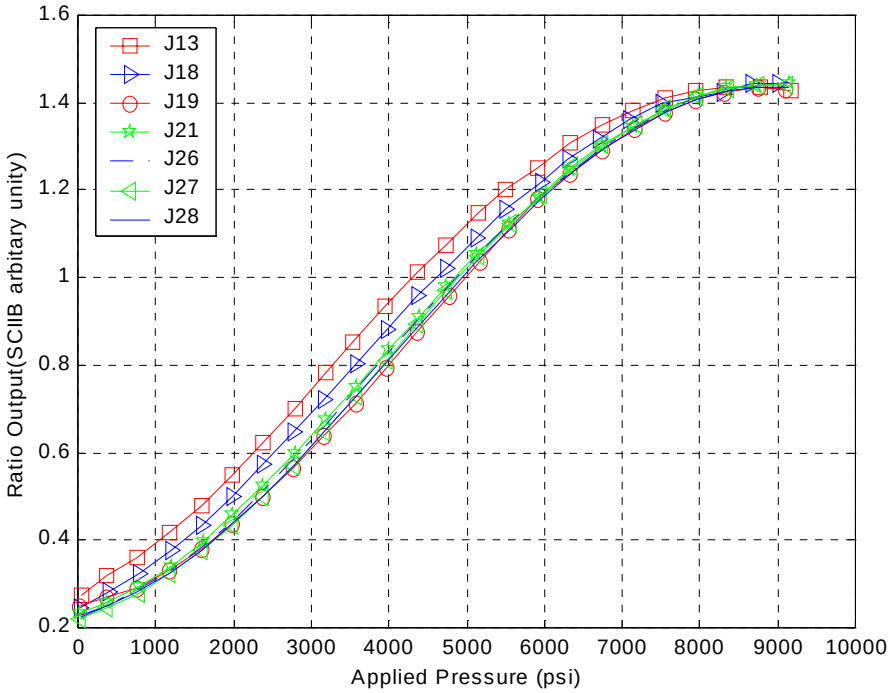

Figure 11.20. Measured pressure versus applied pressure as a function of exposure time for an uncoated sensor (continued).

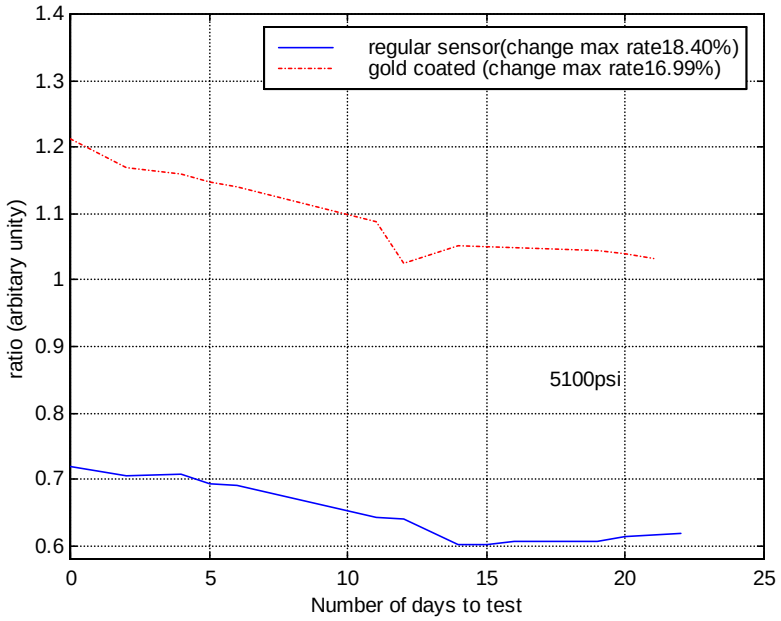

Figure 11.21. Pressure calibration difference between first and following days versus date for a gold coated and an uncoated sensor.

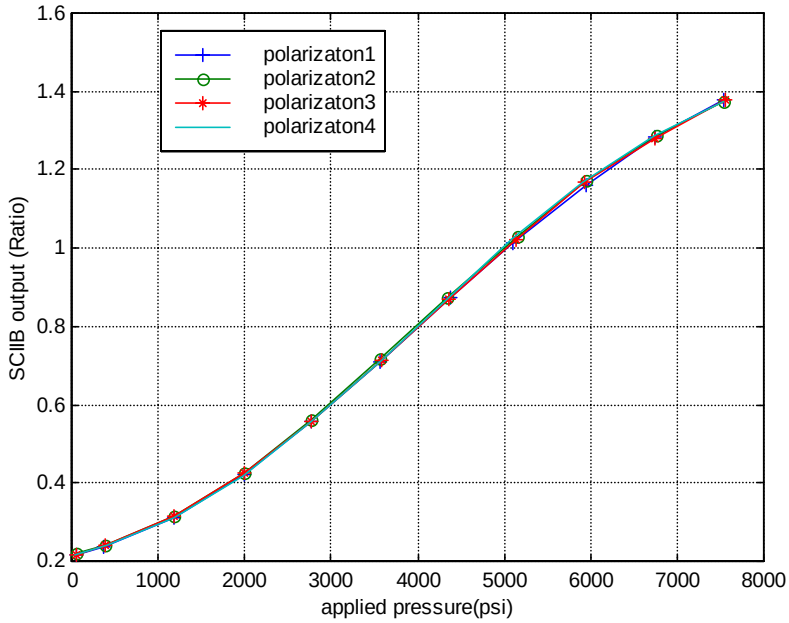

Figure 11.22. SCIIB output versus applied pressure and as a function of different fiber pigtail polarization states.

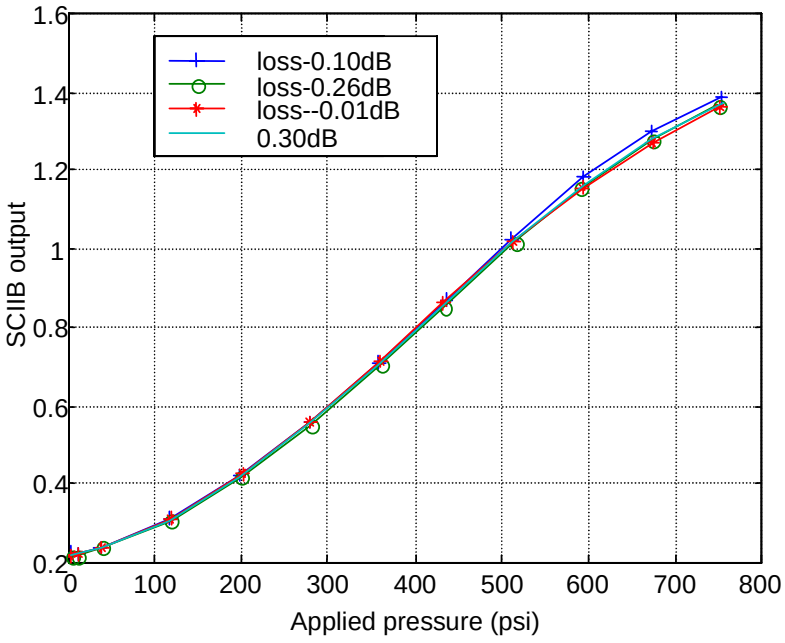

Figure 11.23. Effect of fusion splice loss on the SCIIB output.

In an attempt to improve the system stability, a second system was constructed. Calibration curve changes for this system for the fiber pigtail polarization state had an average polarization error of about 0.23%~0.787% as shown in Figure 11.24. Figure 11.25 shows the SCIIB output versus applied pressure for different splice losses for the improved system. The splice loss repeatability in the new system has dropped to approximately 0.5%

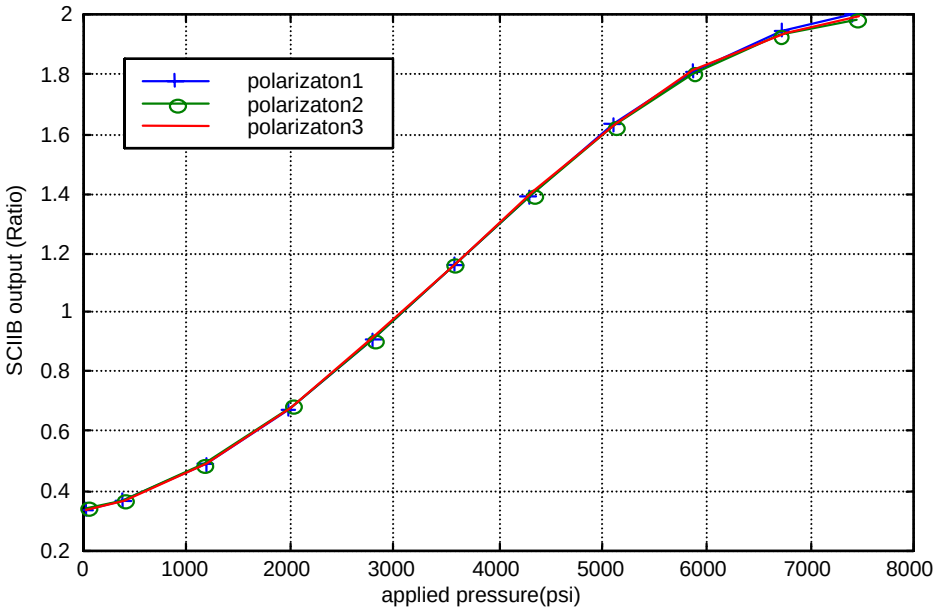

Figure 11.24. SCIIB output versus applied pressure and as a function of different fiber pigtail polarization states for improved system.

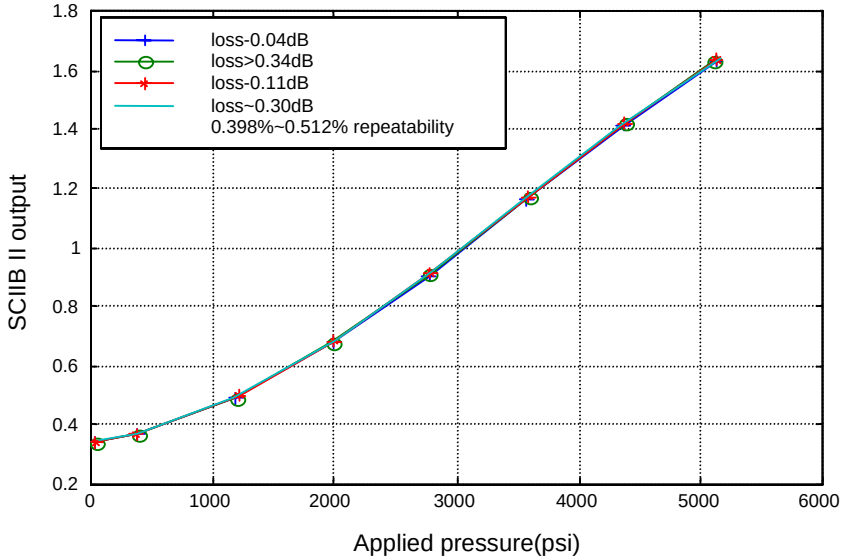

Figure 11.25. Effect of fusion splice loss on the SCIIB output for improved system.

11.6 Encapsulated Fiber

This method involves encapsulating the sensor head in a soft metallic material while simultaneously encapsulating the metal in an outer heat shrinkable tubing. The process required identification of suitable metallic and polymeric materials such that the melting temperature of the metallic material was in the same range as the consolidation temperature of the polymeric material.

11.6.1 Structure of the fiber sensor protection package:

The structure of the packaging system is shown schematically in Figure 11.26. The arrangement of the tubes can be performed quite easily be hand. In addition, no special microscopic equipment is necessary, so the process is very simple.

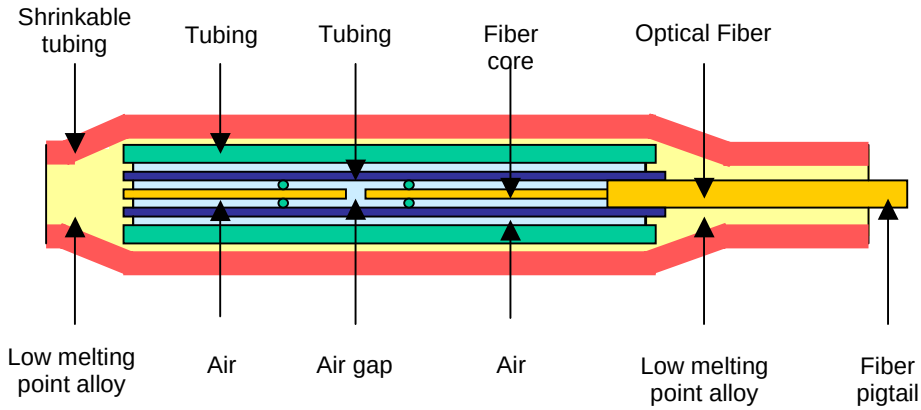

Figure 11.26. Schematic of the protection packaging assembly.

1. Materials:
   - Small tubing (silica glass tubing, stainless steel tubing, etc).
   - Heat shrinkable tubing
   - Low melting point metal or alloy

2. Structure: The sensor is positioned within the small outer tubing, of which, the diameter is only slightly larger than that of the sensor tubing. The small outer tubing is also a little bit longer than that of the sensor. The outermost part is the heat shrinkable tubing. Between the small outer tube which covers the sensor and the heat shrinkable tubing that covers the entire system, a low melting temperature metal is placed, which is used to isolate the sensor from moisture.

11.6.2 Packaging process

11.6.2.1 Material preparation:

1) Sensor preparation—It was important to ensure that the dimension of the sensor is small enough to allow proper packaging while still meeting the overall size requirements imposed on the sensor package by the deployment process.
2) Small tubing preparation—It was important to ensure that cutting of the tubing was performed evenly and control of the length was accomplished such that the outer glass tubing was slightly longer than that of the sensor head.
3) Shrinkable tubing preparation—It was important to control the length of this tubing such that it was a little longer than small outer tubing.
4) Low melting point metal preparation— Metal tubing was fabricated from metal sheets to aid in assembly of the components for bonding. As such, the metal tubing was cut slightly longer than the small outer tubing and shorter than the shrinkable tubing.

11.6.2.2 Fabrication Procedure:

1) Put the sensor into the small outer tubing.
2) Put the small outer tubing into low melting point metal tubing.
3) Put the metal tubing into the shrinkable tubing.
4) Carefully position the sensor and the tubing.
5) Heat them in a controlled way to make the shrinkable tubing shrink, while the metal is melted and flows out of the two ends of the shrinkable tubing.
6) The heating temperature, heating direction, and the amount of the metal is controlled.
7) For the pressure sensor, the metal contacts the two ends of the sensor. For the temperature sensor, at least one end of the sensor is free.
8) Final treatment: cut the excess part of the package and remove the excess metal on the ends of the packaged sensor.

This method proved to be extremely simple to employ in an oil field setting, was robust enough to be able to be applied reliably, and was found to be a very inexpensive solution. No special tools were required to perform the operation. The only tools used were a heat gun, small screwdriver, pliers and a ceramic plate to protect the surface below from heat. Extensive testing of the protected sensors was performed to ensure performance of the protection packing and to characterize the change in performance before protection versus after protection. Overall, the performance of the packaging method was found to be excellent.

12.0 Field Testing of Flow Sensor System

To demonstrate the feasibility of the developed flow sensor system, the prototype sensor system was field tested at the flow loops at the University of Tulsa from Aug 19, 2002~Aug 23, 2002. Two flow loops were involved in this field-tests; the detailed technical parameters and testing results are reported here.

12.1 Indoor Flow Testing

The indoor flow facility we used for flow testing is shown in Figure 12.1a. A variable frequency pump (0~1745RPM) from *Robins & Meyers, Inc* (Figure 12.1b) was used to pump the water into 1-1/2″ Schedule 40 flow loops, which combine many gauges including an adjustable pressure valve, pressure gauge from *Wika, Inc* and thermocouple from *Omega, Inc.* As shown in Figure 12.1(c), the flow sensor was deployed in the flow pipes using a 0.5~1.5inch NPT bushing through a 1.5inch NPT T-fitting. Figure 12.1(d) shows the flow sensor connected by a dual fiber cable to the rest of the fiber optic flow measurement system, which mainly includes a multimode fiber optic white light interferometric system. The output of white light system is shown as Figure 12.1(e), the flow rate measurement window is shown as Figure 12.1(f). The temperature of the flow loops during indoor testing was controlled by the air conditions and was stable at around 29ºC; the pressure in the flow pipes was controlled at around 5psi. The parameters of fiber optic flow sensor used in this indoor testing are listed in Table 12.1.

Table 12.1. Parameters of fiber optic flow sensor used for indoor flow testing in Tulsa.

Fiber type:	Multimode 50/125
Cantilever beam material:	Invar sheet
Cantilever beam size:	0.010"*1.5*0.13"
Original air gaps of two sensors:	10.46μm; 11.96μm
Original visibility of two sensors:	71%; 21%
Gauge length of two sensors:	2.2mm; 1.8mm
Relative temperature coefficients:	1; 0.85
Sensor protection:	Flexible Ni-bellows
Test conditions:	84~86ºF; 1~5psi

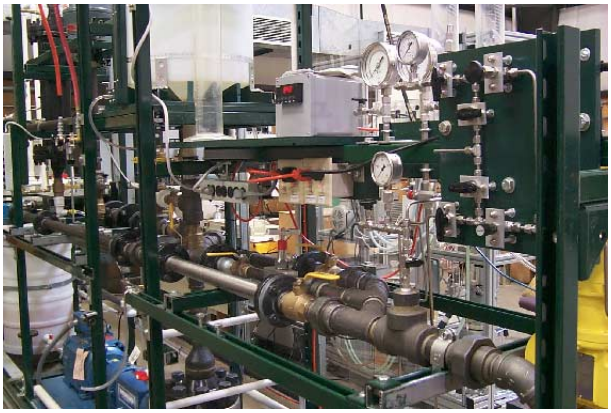

(a) Indoor flow test system in Tulsa University, OK

(b) Variable frequency pump

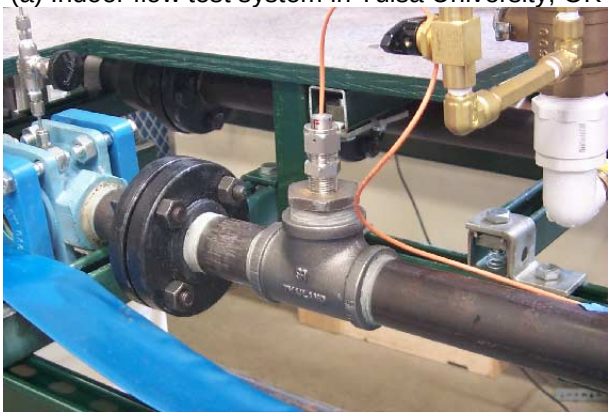

(c) Flow sensor in indoor flow loop

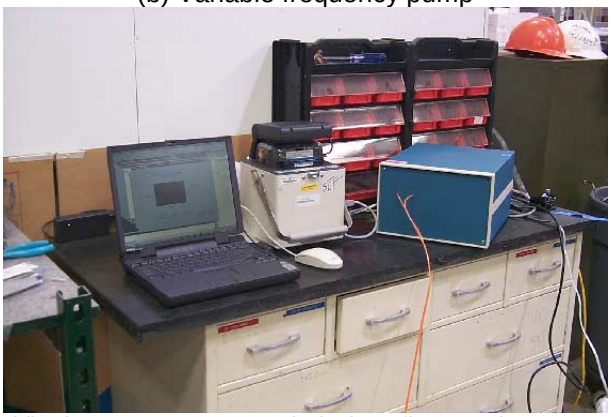

(d) Flow sensor system in indoor flow testing room

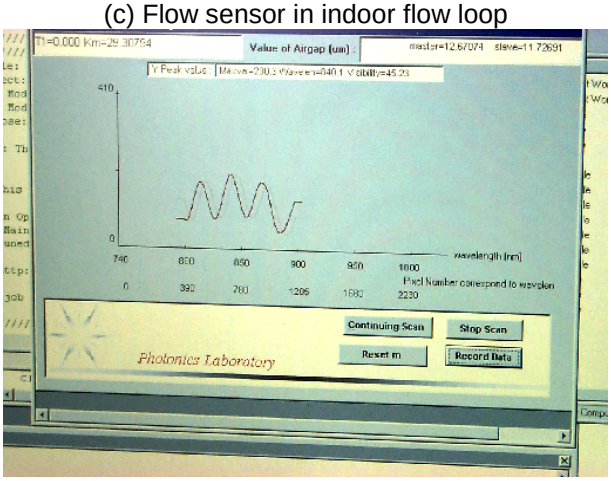

(e) Fiber optic white light system output window

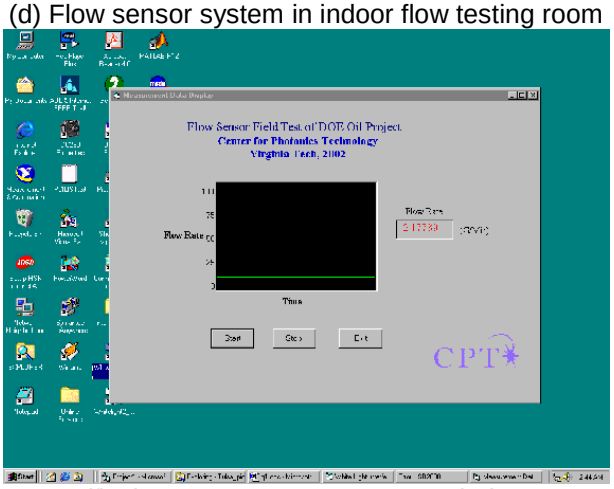

(f) Flow sensor system output window

Figure 12.1. Indoor flow testing system in University of Tulsa , OK.

Compared with the outdoor flow loops, the indoor flow testing facilities were at a very stable temperature and pressure. Due to some unexpected occurrences during shipping, when we arrived at the Tulsa testing field, only one channel of the white light system could be used for the indoor testing while we completed an urgent repair of the other channel. So for indoor testing, we used only one of the two sensors to measure the indoor loop flow rate.

12.1.1 Variable frequency pump calibration

The indoor flow testing system used a variable frequency pump from *Robins & Meyers, Inc* , which had an operating range from 0 to1745RPM, to drive water in the flow loop. Using the FT-NENW turbine flow meter, a calibration was performed first to convert the flow rate units from RPM to GPM; the calibration curve was shown in Figure 12.2.

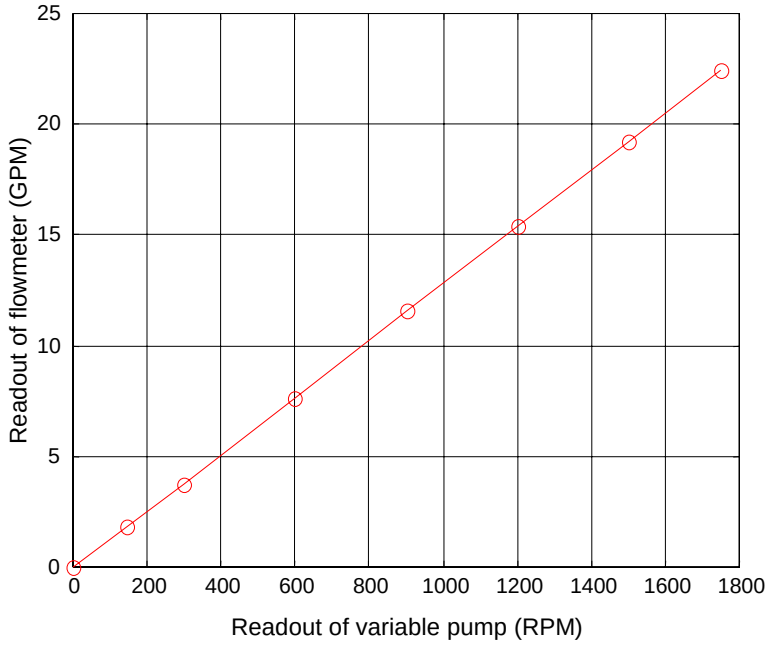

Figure 12.2. Variable frequency pump calibration curve using FT-24NENW flow meter.

12.1.2 Sensor calibration

Due to the difference in testing conditions between the indoor test loop and lab-scale testing, the sensor required recalibration prior to the testing in the outdoor system. The calibration curve of the fiber flow sensor using the output from a reference flow rate is shown in Figure 12.3.

12.1.3 Measurement results and repeatability

The real-time flow rate information was obtained through the calibrated relationship between the reference flow rate and the airgap change in the sensor head. Figure 12.5a shows the measurement results for repeatability testing. The flow sensor output is a linear function of the variable frequency pump rotational speed. A magnified view of the repeatability results is shown Figure 12.5b. For the full measurement range from 0 to 22.42 gallons per minute (GPM), the maximum deviation was ±0.26GPM, which is ±1.15% of full scale.

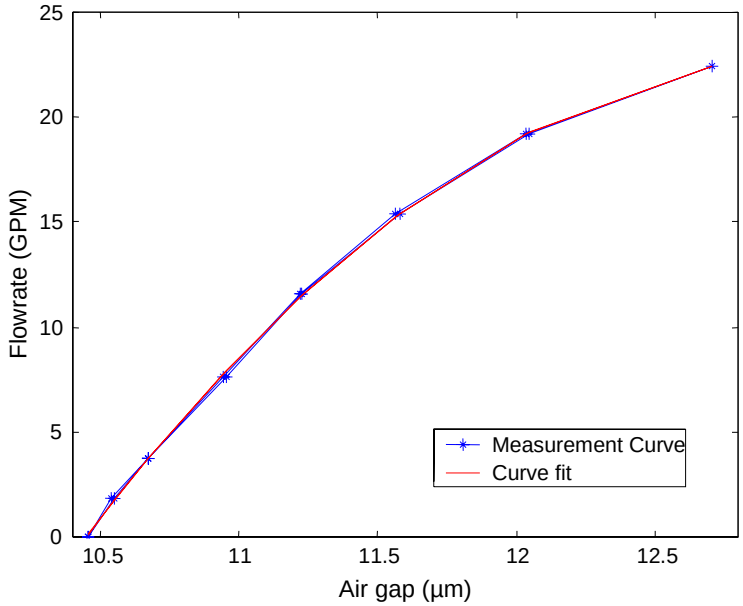

Figure 12.3. Flow sensor calibration curve for indoor flow testing in Tulsa, OK.

12.1.4 Resolution of indoor flow testing

For the indoor flow sensor system, 600 flow values were acquired in one minute with a sample frequency of 10 counts/second (Figure 12.4). The standard deviation of the flow data was σ=0.00123GPM; therefore, the resolution of the sensor system was estimated to be 2σ=0.0246GPM. The normalized resolution with respect to the dynamic range of the system was 0.11% of the full scale.

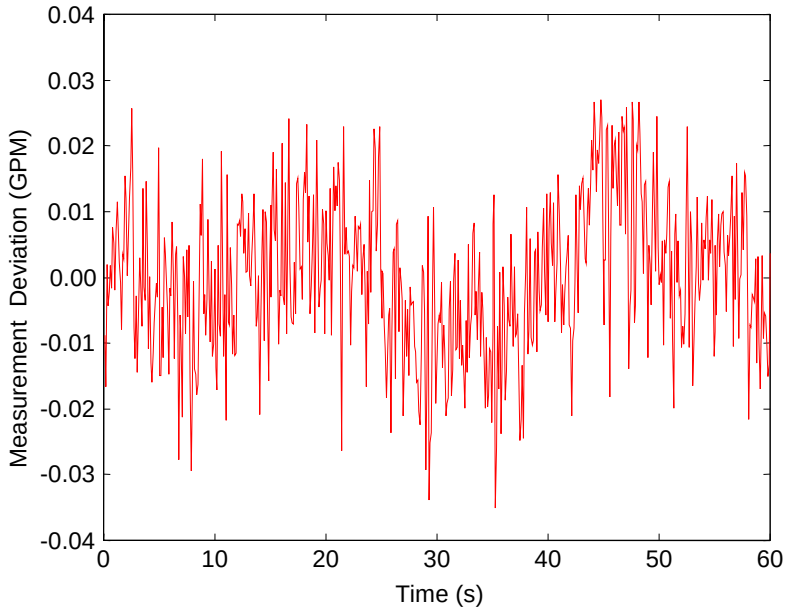

Figure 12.4. Resolution of flow sensor system, indoor flow testing.

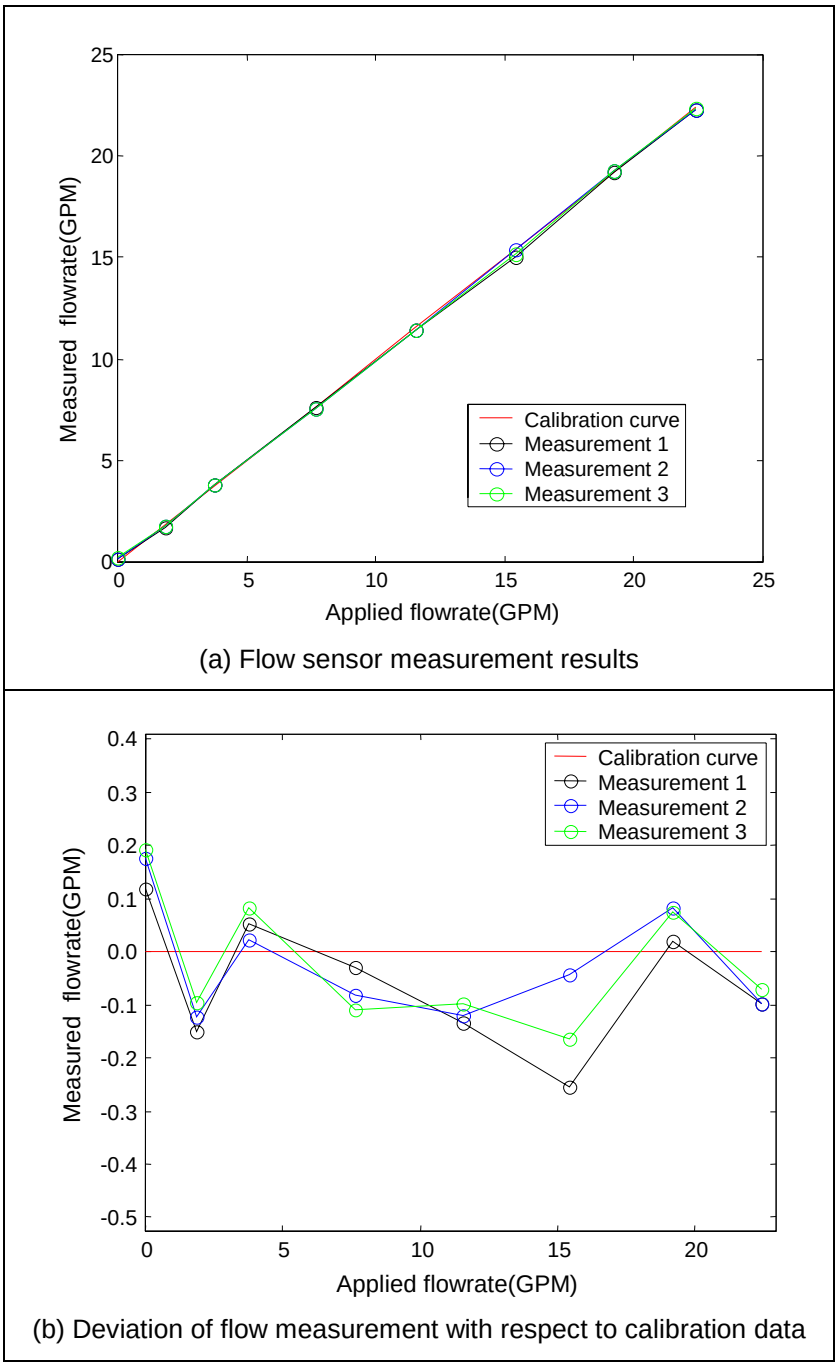

Figure 12.5. Measurement results from fiber flow sensor in indoor testing loop.

12.1.5 Hysteresis of flow sensor

The hysteresis characteristics of this sensor were also tested in the indoor flow loop (Figure 12.6a). No obvious hysteresis was observed for the measured range, as shown in the enlarged data in Figure 12.6b. The hysteresis of the full measurement range was measured to be 0.89% for the indoor flow tests.

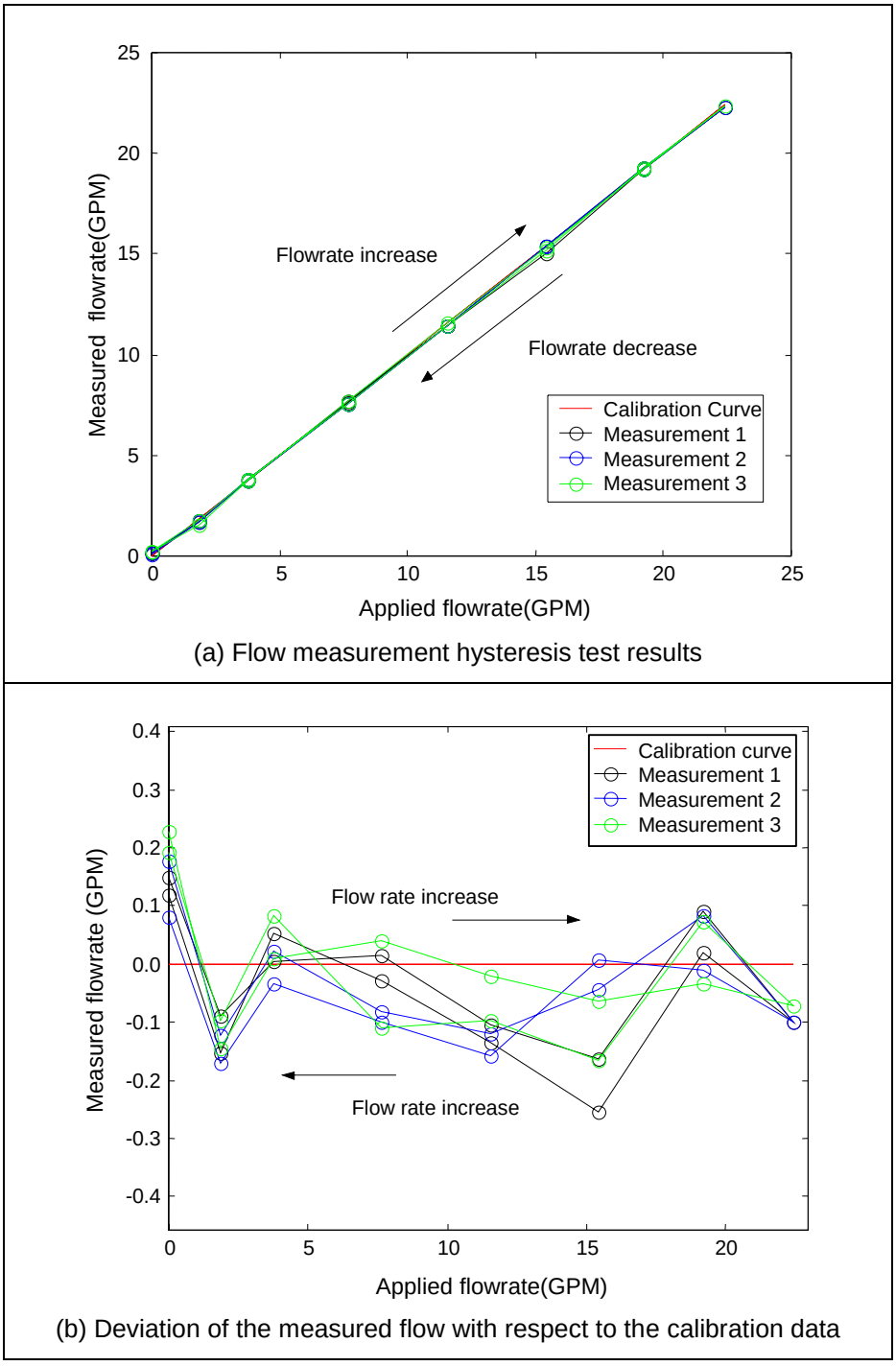

Figure 12.6. Flow sensor hysteresis measurement.

12.1.6 Stability testing

To further evaluate the sensor performance in the indoor flow loop, the stability of the designed sensor system was tested as shown in Figure 12.7. With the flow rate maintained at 4GPM for two hours, the output of the fiber optic flow sensing system was within 0.15GPM; the stability of the system was 0.67% of the full range.

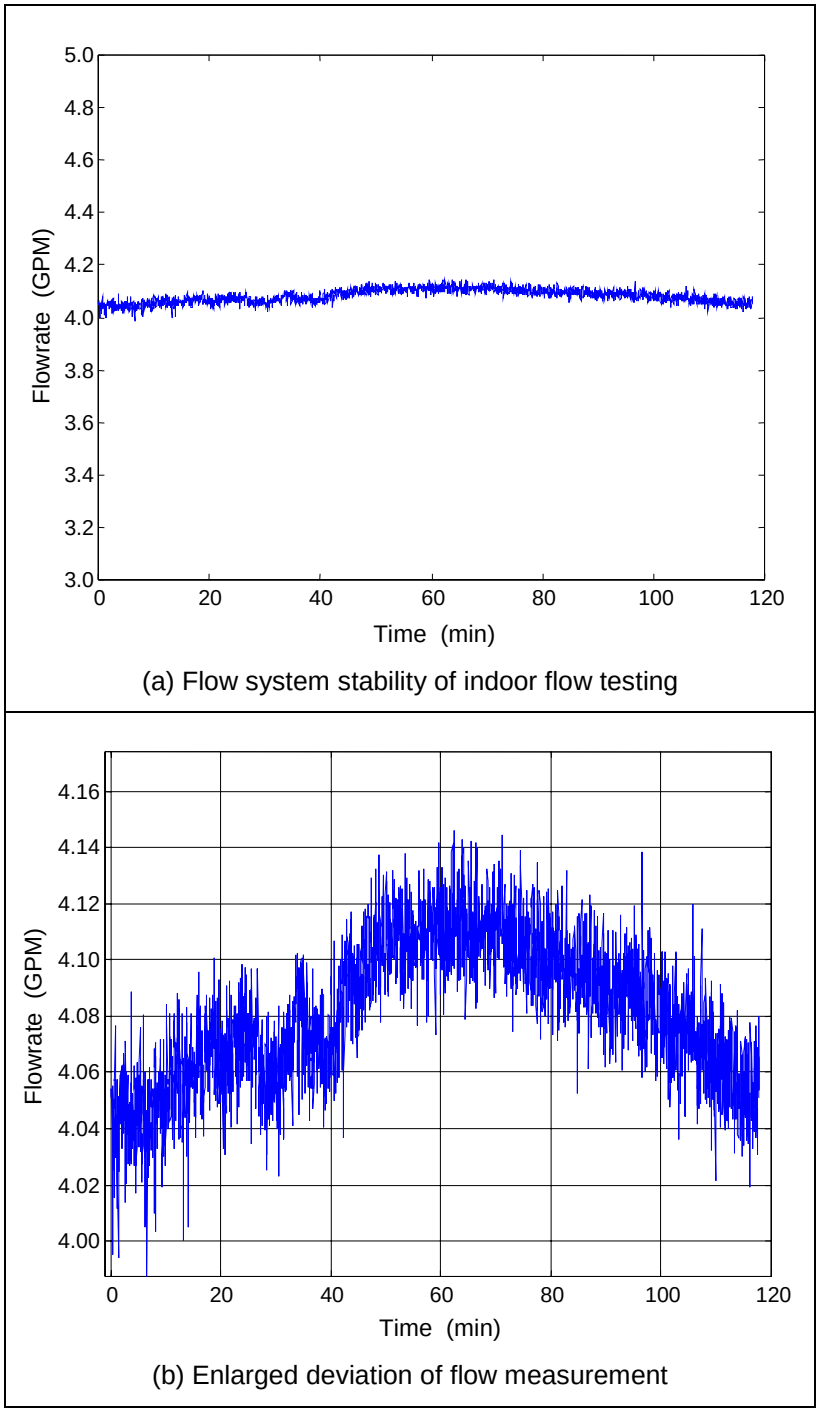

Figure 12.7. Flow system stability test over approximately 2 hours.

12.2 Outdoor Flow Loop Testing System and Results

The outdoor flow testing facility consisted of a simulated oil field flow environment combining pipes from 3 to 6 inches in diameter at various stages (Figure 12.8a). A variable frequency pump (Figure 12.8b)(0~2000GPM) from *Waukesha, Inc* was used for pumping water from the 3500-gallon tank shown in Figure 12.8c. The *Micro Motion* vibration flow meter shown in Figure 12.8d was used as the calibration. Many pressure and temperature gauges (Figure 12.8e) from *Rosemount Incare* were also distributed along the flow pipes to monitor the environmental conditions. The entire facility and gauges were controlled by the central computer in the control room. As shown in Figure 12.9, the fiber optic flow sensor was deployed in the outdoor 3-inch flow pipes using a 1.5 to 0.75inch NPT bushing through into a 0.75 inch welding port. The sensor probe was connected to the sensor system optoelectronic unit in the control room through a dual-core multimode fiber cable. The white light interferometer-based flow sensor control system is shown in Figure 12.10a and the flow rate measurement output window in Figure 12.10b. Using the *Micro Motion* flow meter as a reference, the sensor system was calibrated and tested with the water circulating in the flow loop at different flow rates. After spectrum detection and signal processing, the output flow rate data were digitized, displayed, and recorded.

Due to the complex structure of the outdoor flow testing system, for each testing step a minimum of 20 minutes was required to obtain a relatively stable flow rate. The flow meter and pump were designed for the flow rate range of 0~2000GPM, with ±0.2% accuracy of full range, around ±4GPM. So in the relatively low flow rate range of 0~64GPM, the accuracy of the reference flow meter was diminished. When the pump was set to a certain value, the flow rate fluctuated significantly, affecting the evaluation of the fiber optic sensor system's performance. The flow sensor was calibrated and tested based on the average outputs of the *Micro Motion* flow meter. The outdoor flow loop testing system experienced pressure fluctuations of around 9~66Psi, and temperature changes of approximately 26 to 37ºC. The flow sensor parameters for outdoor flow testing are listed in Table 12.2.

Table 12.2. Fiber optic flow sensor parameters for outdoor flow testing in Tulsa, OK.

Fiber type:	Multimode 50/125
Cantilever beam material:	Invar sheet
Cantilever beam size:	0.012" × 1.5" × 0.13"
Original air gaps of two sensors:	9.27μm; 9.61μm
Original visibility of two sensors:	52%; 29%
Gauge length of two sensors:	1.7mm; 178mm
Relative temperature coefficients:	1; 1
Sensor protection:	Flexible Ni-bellows
Test conditions:	84~86ºF; 1~5psi

(a) Outdoor flow testing loop

(b) Variable frequency pump (0~2000GPM)

(c) Water tank for outdoor flow testing loop

(d) Flow meter in outdoor flow loop

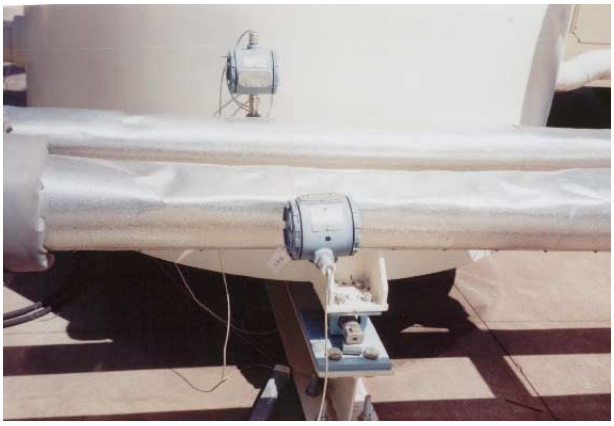

(e) Pressure and temperature gauge in outdoor flow loop

Figure 12.8. Outdoor flow testing facility in Tulsa University, OK.

Figure 12.9. Fiber optic flow sensor deployment in outdoor flow loops of Tulsa University, OK.

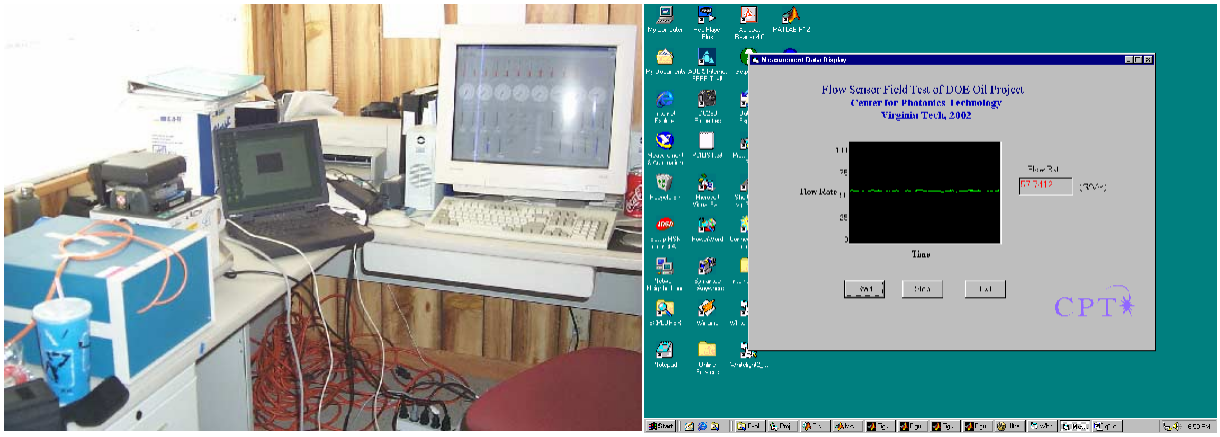

(a) Flow sensor measurement system in the control room of outdoor flow facility

(b) Output window of flow sensor

Figure 12.10. Fiber optic flow sensor control system for outdoor flow testing.

12.2.1 Calibration

Due to the difference in testing conditions (including pipe size, sensor deployment position and fluid characteristics) between the outdoor flow loop and lab-scale testing setup, the sensor required recalibration prior to testing in the outdoor system. Figure 12.11a shows the air-gaps of the two sensors and the output of the system with changes in the flow rate during the calibration. The calibration curve was generated as shown in Figure 12.11b, which provided the compensation coefficients used for the following measurement and evaluation.

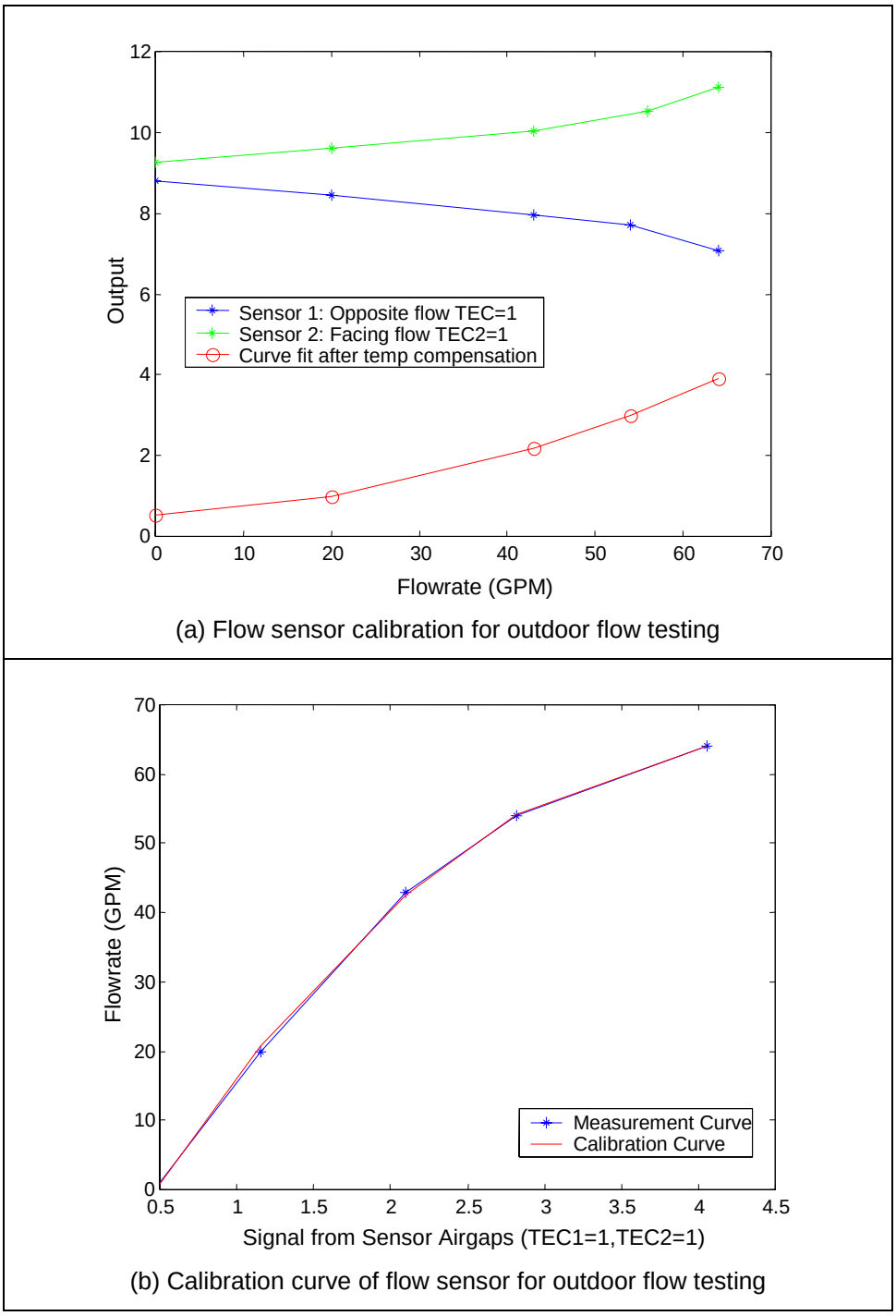

Figure 12.11. Flow sensor calibration for outdoor flow testing.

12.2.2 Stability

The stability of both *Micro Motion* flow meter and the fiber flow sensor are shown in Figure 12.12. Maintaining the variable frequency pump at 57GPM for 70 minutes, the maximum peak-to-peak fluctuation of the reference flow meter was 3.32GPM, which larger than that of the fiber optic flow sensor whose maximum fluctuation is 3.15GPM. Also the standard deviation of the reference flow meter was 0.61GPM, while of the fiber optic flow sensor was 0.42GPM. Relative to the *Micro Motion* flow meter, the mean deviation of fiber optic flow sensor was 0.9327GPM. Based on this data, we believed that the standard deviation of fiber flow sensor was less than 1GPM, and the stability of this sensor system was better than 1.56% for 0~64GPM full scale.

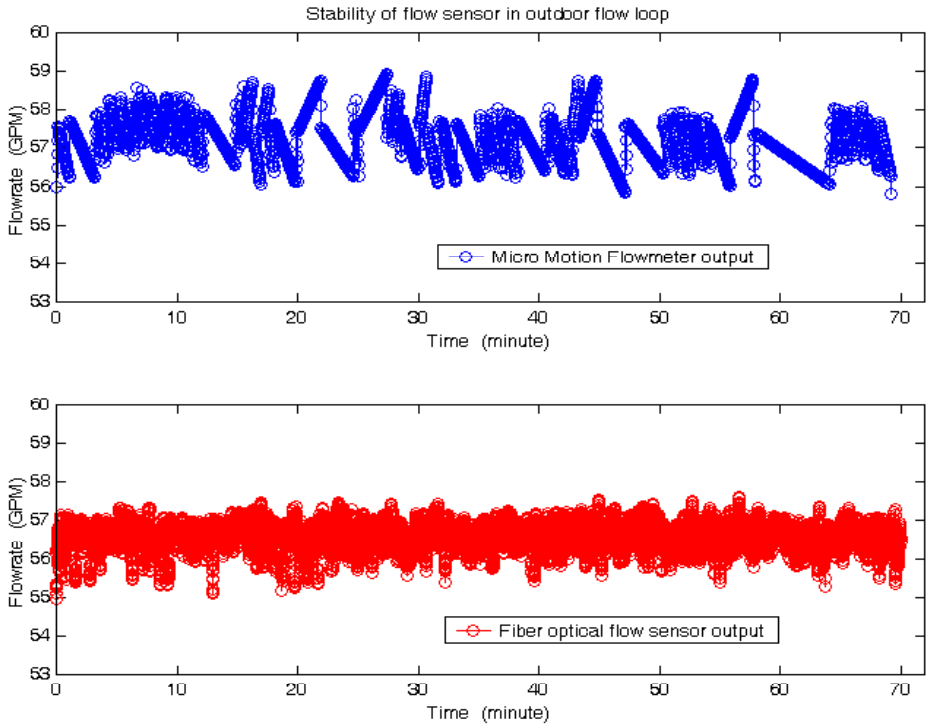

Figure 12.12. Flow sensor stability during outdoor flow testing.

12.2.3 Resolution

Using the same definition of resolution as described previously, the resolution of the fiber sensor system in the outdoor testing system is shown in Figure 12.13, and the calculated standard deviation from this data was σ=0.0083GPM. The resolution of the fiber optic sensor system was estimated to be 2σ=0.1664GPM. The normalized resolution for this sensor system was 0.26% of the full scale.

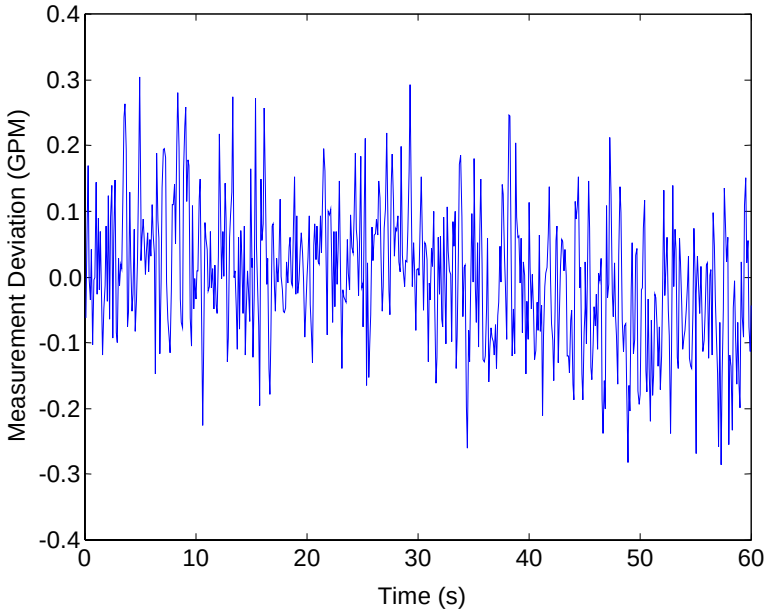

Figure 12.13. Resolution of fiber flow sensor during outdoor flow testing.

12.2.4 Repeatability

The flow rate in outdoor flow loop was measured based on above calibration curve and coefficients. Fig 28 shows the measurement results of flow rate measurements repeated three times. With respect to flow meter output, the deviation of these repeatability measurements were enlarged and shown in Fig 28(b). The maximum deviation was ±0.8GPM, which translates to ±1.25% of full scale.

12.2.5 Hysteresis

As shown in Figure 12.15, the hysteresis of the flow measurement was evaluated as 2.1% of full range during outdoor flow loop testing. Further improvement in sensor performance may be achieved by improving the sensor materials and fabrication techniques, the accuracy of the reference flow rate as well as the test system stability with respect to laminar flow generation.

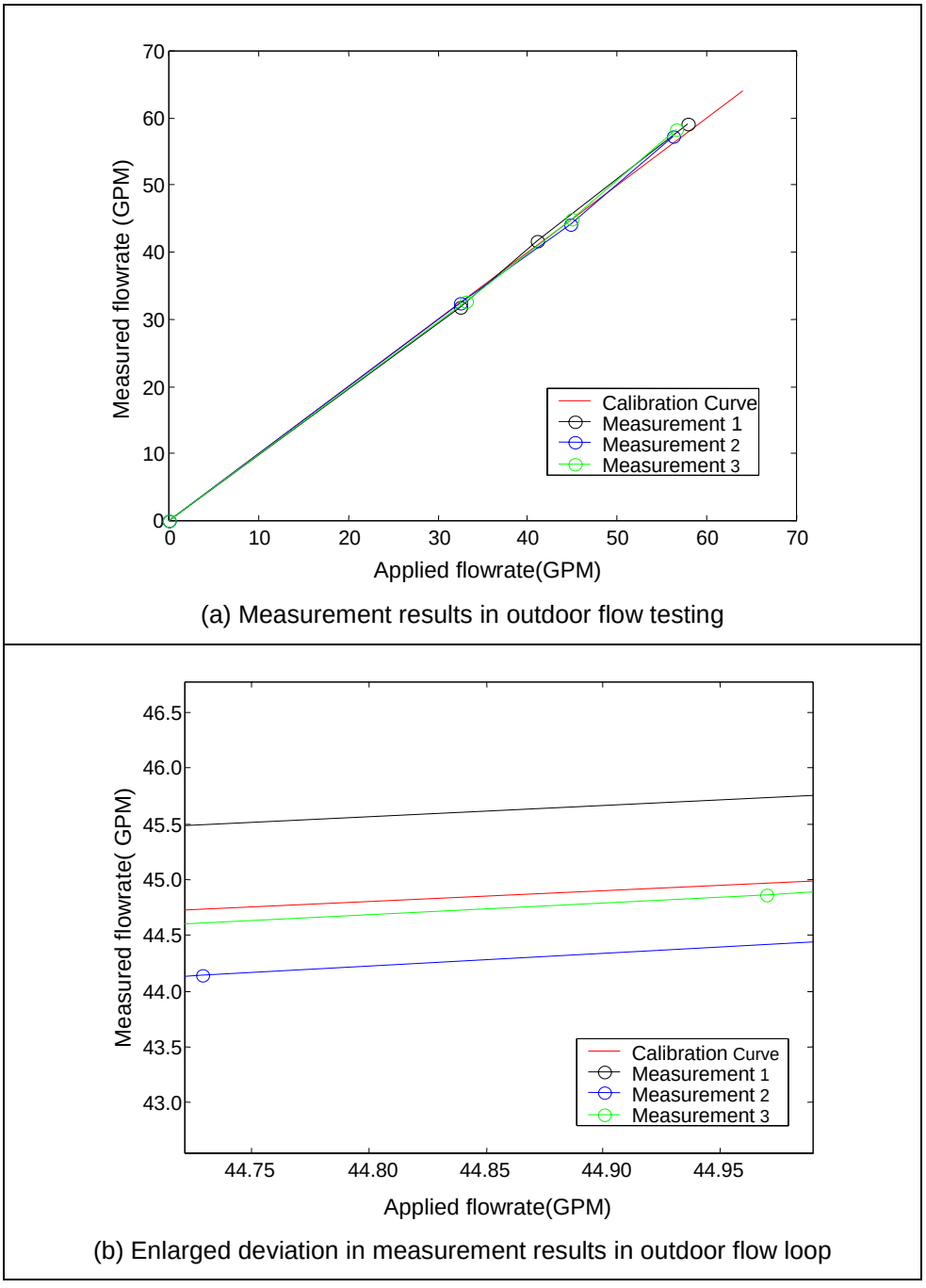

Figure 12.14. Measurement results and repeatability testing in outdoor flow testing.

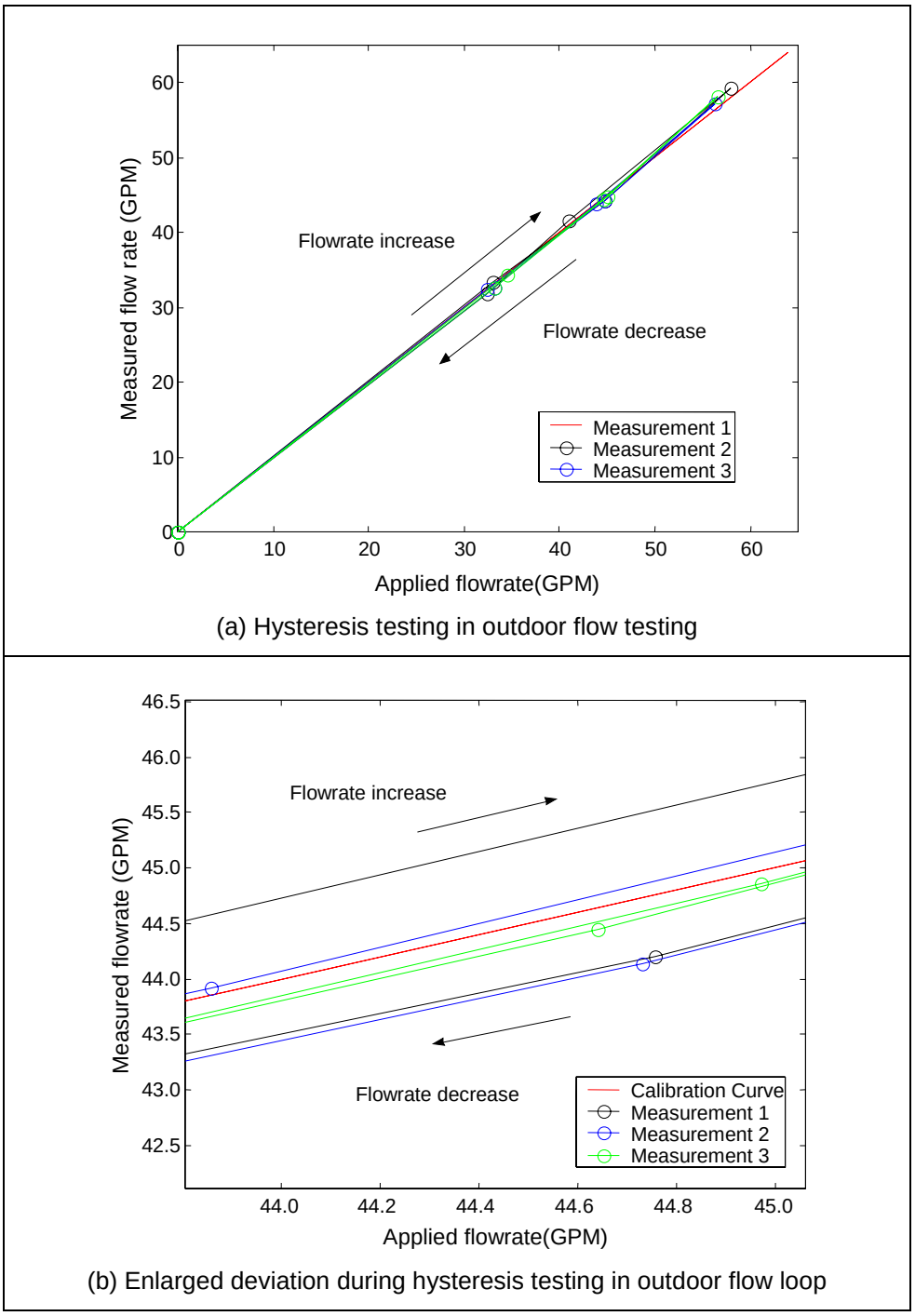

Figure 12.15. Hysteresis testing in outdoor flow testing.

Table 12.3 Summary of the performance evaluation results for fiber optic sensor systems.

	Repeatability	Hysteresis	Resolution	Stability
Lab-scale flow testing	±1.62%	1.35%	0.11%	<1.89% (~12hrs)
Indoor flow loop testing	±1.15%	0.89%	<0.11%	0.67% (~2hrs)
Outdoor flow loop testing	±1.25%	2.1%	0.26%	<1.56% (~70min)

Table 12.3 shows the overall summary performance of the fiber optic flow sensor testing for the both the laboratory testing and field testing.

13.0 Temperature and Pressure Sensor Field Testing

To evaluate the performance of the fiber optic sensor system in the oil site, a multimode white light sensor system was tested at the oil site of Chevron/Texaco Company (Coalinga CA).

13.1 First Coalinga Field Test

The main purpose of the first field test included verifying the deployability of the sensor head, testing the remote data access through the Internet, and evaluating the long term stability of the sensor head in the downhole environment.

13.1.1 Sensor deployment

A hydraulic optic fiber deployment system developed by the Chevron Company was used to deploy the pressure senor. The sensor head with connecting optical fiber was pumped down by utilizing hydraulic oil as the suspension media and force-imparting member. The sensor head moved down about 250m along the stainless steel pipe. The inner diameter of the metal pipe is smaller than 4mm, and there are several connectors along the pipe. Several times during the deployment of the sensor, the sensor apparently got stuck on something, and the sensor had to be drawn back a little by reversing the fluid flow direction and pushed forward again. The ability of the sensor to survive the rigors of the harsh deployment process is attributed to the improvements in mechanical durability of the sensor head. The position of the sensor head in the oil well was monitored by OTDR. After deployment, a pump was used to increase the pressure inside the testing pipe to about 3000psi, and then all valves were shut off to keep a constant pressure inside the pipe.

13.1.2 Remote access and control

13.1.2.1 Hardware configuration

The host computer that controlled the fiber sensor measurement was a Dell Latitude, P2-350 notebook with 128MB memory and 4.5GB hard disk. The Ethernet card was a SMC8040Tx 10/100 PC Card. The client computer was a PC desktop, P2-350 with 128MB memory, 6GB hard disk and a NE2000 compatible Ethernet card. This computer remotely controlled the host computer and obtained the measurement data through the internet.

13.1.2.2 Software configuration

The operating system was Windows 98 Second Edition. The remote control software was Symantec pcAnywhere 10.0, and the VPN service software was Nortel extranet access client V2.50.

13.1.2.3 Connection establishment

Host Computer:

In order for the notebook computer to log onto Chevron's intranet and obtain a static IP, the authorized user name and correct password was input when the computer enters Windows 98. The host computer must maintain the logon status.\

Client Computer:

On the client side, the computer is on the internet all the time through the Virginia Tech LAN. Each time the host computer was remotely controlled, the following steps were required:

(1) Run the extranet access client software; the window shown in Figure 13.1 will pop up. Then input the authorized user name and the pin plus passcode. The passcode is generated every 60 seconds by a security card.

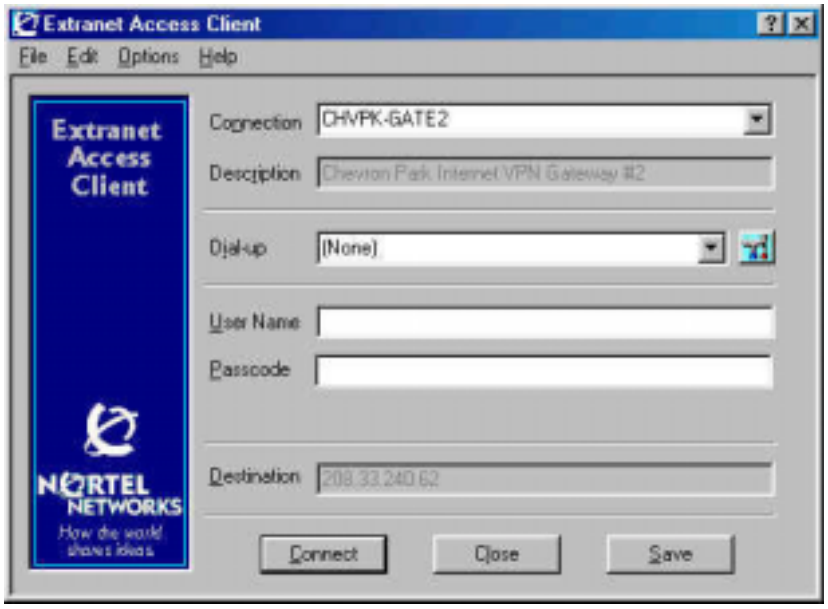

Figure 13.1. Nortel Extranet Access Client Software.

(2) Run 'pcAnywhere'and start the 'doe' task, which will try to connect to the host computer, when the host computer responds the window shown in Figure 13.2 will pop requesting the user name and password for secure connection.

When the above steps are performed successfully, the entire screen of the host computer will be displayed on the client computer. Then the host computer can be controlled using the client computer's mouse or keyboard.

Figure 13.2. pcAnywhere Manager Window.

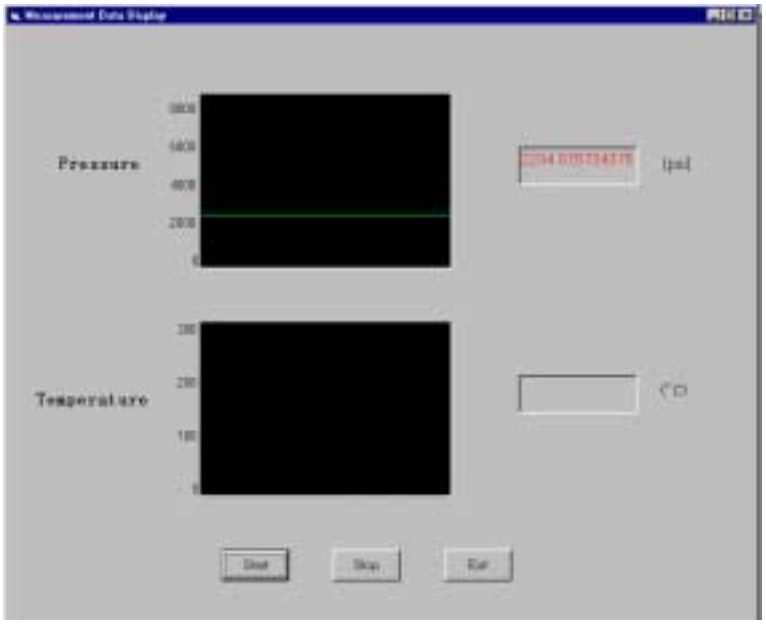

Figure 13.3. Pressure Measurement Window.

13.1.2.4 Data saving and remote access

The fiber sensor based measurement system measures the pressure in the oil well every minute and saves the data to the hard disk of the host computer. The software generates a new filename at time 00:00:00 every day so that one file will contain a single day's measurement data. The filename is the date, for example, '10-03-2001'. The data format is text, as follows:

Time		Pressure
10-03-2001	10:23:00	2290.3298
10-03-2001	10:24:00	2290.3021
……		

It is convenient to find a specific day's data by searching the filenames. Using one file for each day will not cause a huge size data file so that the download will be easy. For remote data access, we can use pcAnywhere's 'File Transfer' function: Run the file transfer function; a window will pop up showing the directory list of the host and the client computer separately in two subwindows. We can use a mouse to drag the file from the host window to the client window to finish the download.

13.1.2.5 Network security

The network security of the remote access is very important. The host computer cannot be accessed without running extranet access software first. The host computer is on Chevron's Intranet. Correct username and passcode are needed. The passcode consists of a PIN and Security Card Number, and the Security Card Number will change every 60 seconds and will be examined by the server of the Chevron's gateway. Also, pcAnywhere has its own network security: a username and password are needed to establish remote control. Therefore, the network security is very good.

13.1.3 Long-term stability

This system ran for more than three months in the downhole environment, and the computer was accessed remotely from Virginia Tech. The whole system functioned well during this period. Figure 13.4 shows the testing results for first 90 days.

The slow decrease in pressure was expected due to the leakage of the pressure system. A surface-mounted pressure sensor in-line with the fiber optic pressure sensor also shows the downward trend of the pressure with time. The magnitude of the drift downward for the surface mounted pressure sensor is much larger than for the subsurface fiber optic sensor.

13.2 Second Coalinga Field Test

After the successful achievement of the goals outlined for the first field test, the sensors were again deployed using a hydraulic optic fiber deployment system developed by the Chevron/Texaco Company and the position of the sensor head in the oil well monitored by OTDR. After deployment, a pump was used to increase the pressure inside the testing pipe to about 3000psi, and then all valves were shut off to maintain a constant pressure inside the pipe. As discussed previously, the sensor system was accessed remotely to control the host computer and obtain the measurement data. Data was saved to the hard disk of the host computer once per minute. The software generated a new filename at time 00:00:00 each day so that one file contained one day's measurement data. Figure 13.5 and Figure 13.6 show the testing results through the end of the fourth program year.

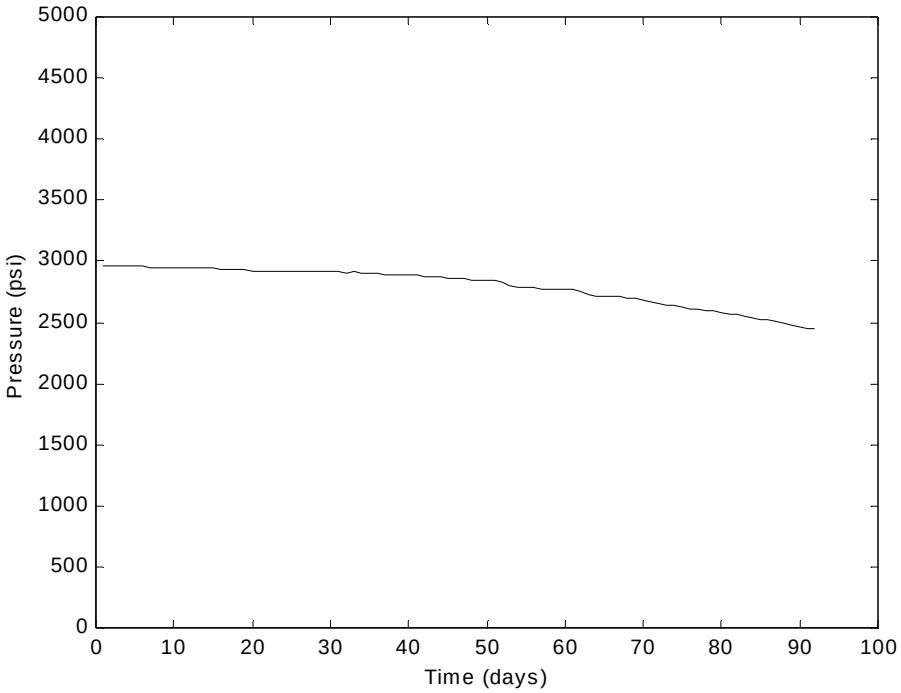

Figure 13.4. Ninety day testing result in oil site.

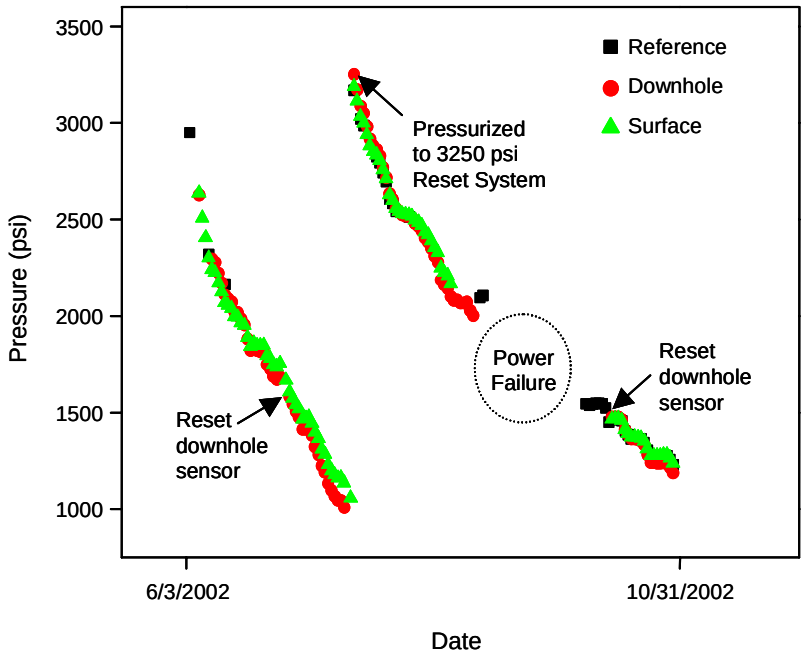

Figure 13.5. Pressure sensor output from 6/3/2002 - 10/31/2002.

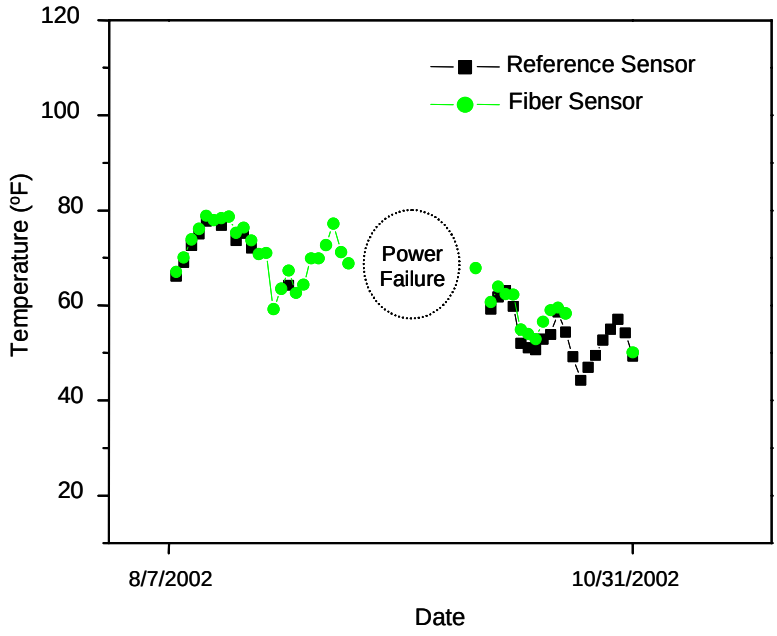

Figure 13.6. Temperature sensor output from 8/7/2002 – 10/31/2002.

14.0 Summary and Conclusions

This four and one half year program successfully developed optical fiber sensors for measurement of pressure, temperature, flow and acoustic waves, including three successful field tests in the oil fields of Chevron/Texaco in Coalinga, California and at the world class oil flow loop facilities at the University of Tulsa, in Tulsa, Oklahoma.

Successes demonstrated in this program include:

- Proven deployability of fiber optic sensors – no sensors have failed in any of the three field tests during deployment
- Pressure sensor resolution of 0.03psi, repeatability of 0.15% full scale and stability of 0.01%
- Flow sensor resolution of 0.26% and stability better than 1.56%
- Successfully completed two sets of field tests in the Chevron/Texaco's Coalinga, Ca oil fields
- Developed sensor and hermetic packaging that can be deployed through 0.25inch O.D., 0.125 inch I.D. high pressure steel tubing – packaged sensor is less than 1mm in diameter
- Developed remote monitoring and control systems so that all the computers in the field site at Coalinga, Ca could be monitored and controlled from virtually anywhere in the world through remote internet access
- Successfully developed and field tested flow sensors at the University of Tulsa's indoor and outdoor flow testing loops. The flow sensors preformed very well in both systems
- Successfully developed and tested acoustic sensors

In more detail, major research areas included design and fabrication of sensor probes, development of DSP-based signal processing techniques, construction of test systems, development and testing of strategies for the protection of optical fibers and sensors in the downhole environment, remote internet data access system to allow monitoring of the real time data from virtually anywhere in the world, evaluation of sensor performance in laboratory testing and improvement of the performance of the SCIIB optoelectronic signal conditioning system. A breakthrough in the signal demodulation method led to the development of the white light interferometer instrumentation system, which was ultimately shown to be the optimal system for high resolution, low speed applications, and was used in this project for pressure, temperature and flow measurements. Comprehensive testing was performed to systematically evaluate the performance of the fiber optic sensor systems in both laboratory and field environments.

Pressure and temperature sensors were successfully deployed using Chevron's hydraulic deployment method into a test well in Coalinga, California and the long-term stability of the

sensor head in the downhole environment verified. Hydraulic deployment added the additional constraint that the packaged sensors had to be less than 1mm in diameter to fit throught the hydraulic tubing. To ensure the durability of the sensor head such that it would be able to survive the rigorous deployment process, the sensor head was encapsulated in a soft metallic material while simultaneously encapsulating the metal in outer heat shrinkable tubing. This method proved to be extremely simple to employ in an oil field setting, was robust enough to be able to be applied reliably, and was found to be a very inexpensive solution. Extensive testing of the protected sensors verified the packaging performance.

A self-compensating fiber optic flow sensor based on a cantilever beam and fiber optic interferometer was designed and successfully tested in both laboratory and field tests. The extensive laboratory development work for the optical fiber sensors culminated in successful long term field demonstrations.

Every portion of the sensor systems from the sensor head to the protective packaging to the optoelectronic signal detection to the signal demodulation algorithm had to perform flawlessly in order for the field testing to be successful. The overall verification and culmination of the extensive development work in this project was manifested in the successful field testing results.

References

1. "Doing Business with DoE: Office of Fossil Energy - Gas and Oil Programs," DoE's Office of Gas and Petroleum Technology, Wsahington, DC (1994).
2. A. Wang, H. Xiao, J. Wang, Z. Wang, W. Zhao and R. G. May, Self-Calibrated Interferometric/Intensity-Based Optical Fiber Sensors,J. Lightwave Tech. 19 (10), 1495-1501 (2001).
3. G. P. Agrawal, Fiber-Optic Communication Systems, 2nd ed, John Wiley & Sons, New York (1997).
4. G. S. Brady, H. R. Clanser and J. A. Vaccari, in Materials Handbook, pp. 518, (1997).
5. N. P. Cheremisinoff, Applied fluid flow measurement - fundamentals and technology, M. Dekker, New York (1979).
6. N. P. Cheremisinoff and P. N. Cheremisinoff, Flow measurement for engineers and scientists., M. Dekker, New York (1988).
7. J. Dakin and B. Culshaw, Optical Fiber Sensors: Principles and Components, Artech House, Boston (1988).
8. M. di Giovanni, Flat and corrugated diaphragm design handbook,11, M. Dekker, New York (1982).

List of Acronyms and Abbreviations

A/D, analog to digital
APP, Advanced Pressure Products, Inc.
CCD, charge couple device
CPT, Center for Photonics Technology
CTE, coefficient of thermal expansion
EMI, electromagnetic interference
FWHM, full width half maximum
GRIN, graded index
LAN, local area network
LED, light emitting diode
MMF, multimode fiber
PC, personal computer
PZT, lead zirconium titanate
SCIIB, self-calibrated interferometric/intensity-based
SLED, superluminescent light emitting diode
SMF, singlemode fiber
SNR, signal to noise ratio
VTPL, Virginia Tech Photonics Laboratory (now Center for Photonics Technology)